

Structural and chemical variations in pyroxenes

MARYELLEN CAMERON

Board of Earth Sciences, University of California
Santa Cruz, California 95064

AND J. J. PAPIKE

Department of Earth and Space Sciences
State University of New York
Stony Brook, New York 11794

Abstract

Within the last 15 years, approximately 80 high-quality, three-dimensional structure refinements of terrestrial, lunar, and meteoritic pyroxenes were published. The majority of the refinements involve $C2/c$ clinopyroxenes and $Pbca$ orthopyroxenes, but $P2_1/c$ structures are also well represented. Few data are available on the $Pbcn$ pyroxenes that constitute the fourth major structure type. The topology of the four space groups can be described with idealized models composed of tetrahedral-octahedral-tetrahedral "I-beam" units that lie parallel to [001]. The different symmetries are a result of different stacking sequences of the octahedral layers and/or of symmetrically-distinct tetrahedral chains in adjacent layers. In all of the pyroxenes refined, the M1 cation site is coordinated by six oxygens arranged in a regular pseudo-octahedral configuration. The M2 site is irregularly coordinated by six, seven, or eight oxygens. The M2 coordination depends upon the size of the cation occupying the site: higher coordination numbers are usually associated with larger cations. The maximum deviation of the tetrahedral chains from an extended configuration ($O3-O3-O3 = 180^\circ$) occurs in the B chains of several $Pbca$ structures where $O3-O3-O3 \cong 136^\circ$. The A tetrahedral chains in most $P2_1/c$ structures are S-rotated, but all other chains are O-rotated. Studies of pyroxene structures at elevated temperatures and pressures revealed that the cation polyhedra expand and compress differentially. The high temperature studies documented a $P2_1/c \rightleftharpoons C2/c$ transition in the Fe-Mg pyroxenes, and showed that the temperature of the transition decreases with increasing ferrosilite content. In addition, these studies provided further insight into the miscibility between the high-calcium and low-calcium pyroxenes and produced cell parameter data that are basic to geothermometry studies involving exsolution lamellae. Site occupancy refinements confirmed the preference of the Fe^{2+} for the larger, more distorted M2 site in the Fe-Mg pyroxenes. Cations in synthetic pyroxenes show a preference of $Mn > Zn > Fe^{2+} > Co > Mg$ for the M2 site. T-O distances in the $Pbca$ orthopyroxenes indicate that Al concentrates in the TB tetrahedron.

Examination of the chemistry of 175 naturally-occurring pyroxenes from a variety of lithologies confirms complete solid solution between diopside and hedenbergite and extensive solid solution between enstatite and ferrosilite under crustal P - T conditions. In this limited set of samples the number of Ca atoms per formula unit does not exceed 1.0, which is consistent with its occurrence only in the M2 site. The range in total Al between 0 and 1.0 is smaller than expected, and the maximum amount of ^{IV}Al substitution is 55% of the T site occupancy. Na, when present as a jadeite or acmite component, is responsible for the highest non-quadrilateral contents of the pyroxenes examined. The most important substitutional couples in terrestrial Fe-Mg pyroxenes and augites are $^{VI}Fe^{3+}-^{IV}Al$ and $^{IV}Al-^{VI}Al$. Detailed statistical analysis of 1200 high-quality pyroxene analyses from 11 planetary basalt suites revealed that the $^{VI}Ti-^{IV}Al$ couple is one of the two most important couples for essentially all suites considered. Fe^{3+} is important in all of the terrestrial suites, but is virtually absent in the lunar and

meteoritic suites, reflecting the lower oxygen fugacities that obtained on the moon and meteorite parent bodies.

Transmission electron microscopy (TEM) studies documented the presence of anti-phase domains in pigeonite and omphacite and also elucidated the growth and development of exsolution lamellae as wedge-shaped precipitates. In addition, TEM studies of the textures of exsolution lamellae contributed significantly to the understanding of the mechanisms (spinodal decomposition vs. nucleation and growth) by which exsolution proceeds.

Features within individual pyroxene crystals potentially useful as geothermometers include the Fe²⁺-Mg intracrystalline distribution, the orientation of exsolution lamellae relative to (001) and (100) of the host phase, and differential changes in the unit-cell parameters of the host and lamellar phases during cooling. Attempts to use the size of anti-phase domains as an indicator of cooling rate are of limited use at present.

Introduction

Since the late 1960's, pyroxenes have received increasing attention from both mineralogists and petrologists. The initial upswing in research coincided with the introduction of sophisticated automated equipment into many laboratories, and it was given impetus by studies of lunar rocks, basalts sampled by the Deep Sea Drilling Project, and the newly discovered meteorites in Antarctica. Although previous workers recognized the importance of pyroxenes as petrogenetic indicators, it is only in some of the recent research that their usefulness in providing information on f_{O_2} conditions, temperature and pressure of crystallization, and cooling rates was more fully documented. Chemical studies using the electron microprobe revealed complex zoning trends (e.g., Bence and Papike, 1972) and elucidated the substitutional couples characteristic of various geologic associations (e.g., Schweitzer *et al.*, 1979; Papike and White, 1979). In addition, scores of X-ray refinements of both end-member and disordered pyroxenes provided excellent detailed data on structural variations as a function of composition, temperature, and pressure.

Despite the voluminous amount of data published on pyroxenes in the last 15 years, there are few comprehensive reviews of their chemical or structural variations (e.g., Appleman *et al.*, 1966; Smith, 1969; Zussman, 1968; G. M. Brown, 1972; Morimoto, 1974). The main objectives of this paper are: (1) to provide a concise summary of recent trends in pyroxene research, (2) to discuss the limits of structural and chemical variations in pyroxenes, and (3) to interpret the observed chemical variations in terms of crystal chemical considerations. In preparing this review, we systematically examined, compiled, and plotted much of the data (exclusive of abstracts) published in recent papers; however, for a more detailed discussion of topics not covered (e.g., phase relations)

or those covered in a cursory manner (e.g., microstructures), the interested reader is referred to Deer *et al.* (1978) or to the 1980 *MSA Reviews in Mineralogy, Volume 7: Pyroxenes* (Prewitt, 1980) prepared by the Mineralogical Society of America.

Chemical classification and nomenclature

The general formula for pyroxene can be expressed as XYZ₂O₆, where X represents Na, Ca, Mn²⁺, Fe²⁺, Mg, and Li in the distorted 6- to 8-coordinated M2 site; Y represents Mn²⁺, Fe²⁺, Mg, Fe³⁺, Al, Cr, and Ti in the octahedral M1 site; and Z represents Si and Al in the tetrahedral site. Chromium usually occurs as Cr³⁺ and titanium as Ti⁴⁺, but under the reducing conditions that obtained on the moon and meteorites Cr²⁺ and Ti³⁺ may occur. The cations mentioned above are the most common ones in the rock-forming pyroxenes; however, others do occur in trace amounts or as major constituents in synthetic pyroxenes.

Although pyroxene nomenclature has been discussed for many years and no general consensus exists, we believe that the scheme proposed by Deer *et al.* (1978) (hereafter referred to as DHZ) is satisfactory for most purposes. We use a slight variation of their classification combined with the method of Papike *et al.* (1974). The major chemical subdivisions, which are based on occupancy of the M2 site, are indicated in Table 1. For a discussion of frequently-used pyroxene names (e.g., the varieties of orthopyroxene—bronzite, hypersthene, *etc.*, or varieties of calcium pyroxenes—fassaite, titanaugite, *etc.*) the reader is referred to DHZ. In addition, certain pyroxenes such as enstatite and ferrosilite have several polymorphs. Multiple space groups listed after each entry in Table 1 indicate the different polymorphs; for example, enstatite has three polymorphs with symmetries *Pbca*, *P2₁/c*, and *Pbcn*. Structural details are given below, but for the *P-T* synthesis conditions

and relationships among the various polymorphs the reader is referred to Papike and Cameron (1976), Iijima and Buseck (1975), Buseck and Iijima (1975), Smith (1969), and Burnham (1965).

The system proposed by Papike *et al.* (1974) divides pyroxenes into two chemical groups designated "Quad" and "Others." The Quad pyroxenes (Fig. 1) belong to the well-known pyroxene quadrilateral with the end-members diopside, $\text{CaMgSi}_2\text{O}_6$, hedenbergite, $\text{CaFe}^{2+}\text{Si}_2\text{O}_6$, enstatite, $\text{Mg}_2\text{Si}_2\text{O}_6$, and ferrosilite, $\text{Fe}^{2+}\text{Si}_2\text{O}_6$. The Others chemical group includes pyroxenes with significant amounts of cations other than Mg, Fe^{2+} , and Ca. Figure 1 designates one-phase fields for augite, orthopyroxene, and pigeonite. When only chemical data are available, we will refer to orthopyroxenes and pigeonites jointly as the Mg-Fe pyroxene group. This group generally has $\text{CaSiO}_3(\text{Wo}) < 15\%$ compared to augites with $\text{Wo} \approx 25\text{--}50\%$. We feel it is adequate to designate quadrilateral pyroxenes as augite, pigeonite, or orthopyroxene with the appropriate (Wo, En, Fs) mole percentages, but in order to avoid confusion when referring to specific pyroxenes described in the literature, we use the more detailed nomenclature for quadrilateral pyroxenes proposed by Poldervaart and Hess (1951) and adopted by DHZ. En represents the end-member composition MgSiO_3 ; Fs, the composition FeSiO_3 ; Wo, the composition CaSiO_3 .

In the following paragraphs we give a rather detailed description of our classification procedure because we applied it to 406 pyroxene analyses presented in DHZ and because this system is basic to a further characterization of the relative importance of the various substitutional couples in the pyroxene structure. We used the DHZ analyses because our discussion can be keyed to their book with little repetition of lengthy data tables. In addition, their basic set of analyses includes pyroxenes from a variety of

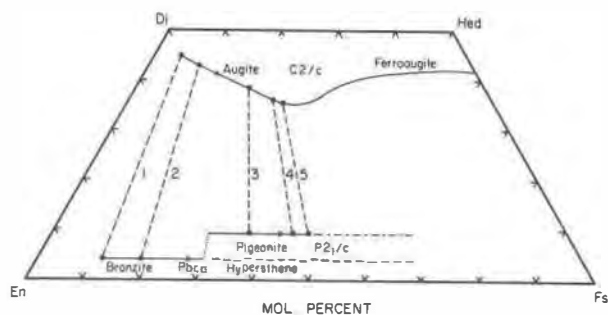


Fig. 1. The pyroxene quadrilateral (after Brown, 1967). Dashed lines 1-5 represent tie-lines joining equilibrium pairs of high-calcium and low-calcium pyroxenes.

Table 1. Major chemical subdivisions of pyroxenes (after Deer *et al.*, 1978)

1. Magnesium - Iron Pyroxenes		
Enstatite	$\text{Mg}_2\text{Si}_2\text{O}_6$	Pbca, P2 ₁ /c, Pbcn**
Ferrosilite	$\text{Fe}_2^{2+}\text{Si}_2\text{O}_6$	Pbca, P2 ₁ /c
Orthopyroxene	$(\text{Mg}, \text{Fe}^{2+})_2\text{Si}_2\text{O}_6$	Pbca
Pigeonite	$(\text{Mg}, \text{Fe}^{2+}, \text{Ca})_2\text{Si}_2\text{O}_6$	P2 ₁ /c, C2/c
2. Calcium Pyroxenes		
Augite	$(\text{Ca}, \text{R}^{2+})(\text{R}^{2+}, \text{R}^{3+}, \text{Ti}^{4+})(\text{Si}, \text{Al})_2\text{O}_6$	C2/c
Diopside	$\text{CaMgSi}_2\text{O}_6$	C2/c
Hedenbergite	$\text{CaFe}^{2+}\text{Si}_2\text{O}_6$	C2/c
Johannsenite	$\text{CaMnSi}_2\text{O}_6$	C2/c
3. Calcium - Sodium Pyroxenes		
Omphacite	$(\text{Ca}, \text{Na})(\text{R}^{2+}, \text{Al})\text{Si}_2\text{O}_6$	C2/c, P2 ₁ /c, P2
Aegirine-Augite	$(\text{Ca}, \text{Na})(\text{R}^{2+}, \text{Fe}^{3+})\text{Si}_2\text{O}_6$	C2/c
4. Sodium Pyroxenes		
Jadeite	$\text{NaAlSi}_2\text{O}_6$	C2/c
Acmite	$\text{NaFe}^{3+}\text{Si}_2\text{O}_6$	C2/c
Ureyite	$\text{NaCr}^{3+}\text{Si}_2\text{O}_6$	C2/c
5. Lithium Pyroxenes		
Spodumene	$\text{LiAlSi}_2\text{O}_6$	C2 (= C2/c)

* $\text{R}^{2+} = \text{Mn}^{2+}, \text{Fe}^{2+}, \text{Mg}$; $\text{R}^{3+} = \text{Fe}^{3+}, \text{Cr}^{3+}, \text{Al}$

** Multiple entries indicate polymorphs having identical composition.

lithologies and, with few exceptions, the analyses include both Fe^{2+} and Fe^{3+} . The latter point is critical to some of our discussions concerning the relative importance of the Others substitutional couples.

As part of our system to assess the quality of an individual pyroxene analysis (other than an oxide wt % sum $\approx 100\%$), we subject each analysis to four additional crystal-chemical consistency tests. After calculating a formula based on six oxygen atoms, a pyroxene analysis is judged "superior" if: (1) the sum of $\text{Si} + {}^{IV}\text{Al} = 2.00 \pm 0.02$ atoms per six oxygens, (2) the octahedral cations ($\text{Mn}, \text{Fe}^{2+}, \text{Fe}^{3+}, \text{Mg}, \text{Ti}, \text{Cr}, {}^{VI}\text{Al}$) sum to > 0.98 atoms per six oxygens, (3) the M2 site occupancy = 1.00 ± 0.02 , and (4) the charge balance equation is balanced (see below) to ± 0.03 of a charge. The purpose of these four tests together with the requirement of a weight percent oxide sum of approximately 100% is to identify those pyroxene analyses that we have no reason to question. This procedure does not imply that any analysis which does not pass all tests is inferior because, for example, ferric iron can enter the tetrahedral site under certain bulk composition, temperature, pressure, and oxygen fugacity conditions (*e.g.*, Huckenholz *et al.*, 1969). In addition, there is good evidence for vacancies in the M2 site, indicating in certain environments the pres-

ence of the component $\text{Ca}_{0.5}\text{AlSi}_2\text{O}_6$ (e.g., Wood and Henderson, 1978; Gasparik and Lindsley, 1980). These additional substitutions are discussed further by Robinson (1980). Our procedure simply identifies those analyses that are either of low quality or that represent a relatively unusual and important substitutional couple.

Papike *et al.* (1974) considered the pyroxene quadrilateral as the reference chemical state, deviations from which constitute the Others pyroxene group. The Others pyroxenes obey the following charge balance equation:

$$\begin{array}{l} \text{Charge Excess} = \text{Charge Deficiency} \\ \text{Relative to Quad} \quad \text{Relative to Quad} \\ {}^{\text{VI}}\text{Al} + {}^{\text{VI}}\text{Fe}^{3+} + {}^{\text{VI}}\text{Cr}^{3+} + 2{}^{\text{VI}}\text{Ti}^{4+} = {}^{\text{IV}}\text{Al} + {}^{\text{M2}}\text{Na} \end{array}$$

As an example of the use of this equation, consider substitution of ${}^{\text{VI}}\text{Al}$, ${}^{\text{VI}}\text{Fe}^{3+}$, or ${}^{\text{VI}}\text{Cr}^{3+}$ into the pyroxene M1 site. This produces a charge excess of +1 relative to the (Mg, Fe^{2+}) occupancy of this site in Quad pyroxenes. By similar reasoning a Ti^{4+} substitution in M1 causes a charge excess of +2 relative to Quad. Obviously, to maintain charge balance in the pyroxene structure, these site charge excesses must be compensated by site charge deficiencies. The substitution of Al for Si in the tetrahedral site causes a deficiency of -1. Similarly, the substitution of Na in the M2 site for (Ca, Fe^{2+} , Mg) also results in a site charge deficiency of -1 relative to Quad. The charge balance equation thus defines the eight most important Others substitutional couples for Li-free pyroxenes; these are ${}^{\text{VI}}\text{Al}-{}^{\text{IV}}\text{Al}$, ${}^{\text{VI}}\text{Fe}^{3+}-{}^{\text{IV}}\text{Al}$, ${}^{\text{VI}}\text{Cr}^{3+}-{}^{\text{IV}}\text{Al}$, ${}^{\text{VI}}\text{Ti}^{4+}-2{}^{\text{IV}}\text{Al}$, $\text{Na}-{}^{\text{VI}}\text{Al}$, $\text{Na}-{}^{\text{VI}}\text{Fe}^{3+}$, $\text{Na}-{}^{\text{VI}}\text{Cr}^{3+}$, and $2\text{Na}-{}^{\text{VI}}\text{Ti}^{4+}$.

Our method for dividing each pyroxene chemically into Quad and Others components is based upon certain crystal-chemical limits in the Others pyroxenes. For example, the M2 site can contain a maximum of one sodium atom per formula unit. Thus, a pyroxene whose M2 site is filled with Na is considered 100% Others and 0% Quad. For each pyroxene analysis examined, we calculate three parameters and use the largest of the three as the percent Others. The parameters are: (1) (Na per six oxygens) \times 100, (2) (${}^{\text{IV}}\text{Al}$ per six oxygens) \times 100, and (3) (${}^{\text{VI}}\text{Al} + {}^{\text{VI}}\text{Fe}^{3+} + {}^{\text{VI}}\text{Cr}^{3+} + {}^{\text{VI}}\text{Ti}$ per six oxygens) \times 100. Quad is simply 100% - % Others.

The charge balance equation discussed above is also used to select a best name for the Others component. A simplified version of the equation is: ${}^{\text{VI}}\text{R}^{3+} + 2{}^{\text{VI}}\text{Ti}^{4+} = \text{Na} + {}^{\text{IV}}\text{Al}$, where R^{3+} is ${}^{\text{VI}}\text{Al} + {}^{\text{VI}}\text{Fe}^{3+} + {}^{\text{VI}}\text{Cr}^{3+}$. Any three of the four variables in this equation can be used as end-members for a ternary Oth-

ers diagram. The result is an Others quadrilateral that separates the Others pyroxenes into five major groups. Papike *et al.* (1974) picked $\text{Ti}-{}^{\text{IV}}\text{Al}-\text{Na}$ as the variables that are used to classify Others (Fig. 2). The five major Others groups can be subdivided into 19 individual end-member names by reference to Table A1.¹ Thus, for example, consider a pyroxene analysis that is characterized as 70% Quad component and 30% Others component with Quad being an augite ($\text{Wo}_{40}\text{En}_{30}\text{Fs}_{30}$) and Others being acmite. If one chooses to use a single "general" name for the pyroxene our procedure for assigning a name and our recommended nomenclature are given in Tables A2 and A3.

Pyroxene topology

The structure of pyroxenes can be described in terms of alternating tetrahedral and octahedral layers that lie parallel to the (100) plane. Within the tetrahedral layer each T tetrahedron shares two corners with adjacent tetrahedra to form infinite chains parallel to the *c* axis (Fig. 3). The base of each tetrahedron lies approximately in the (100) plane and the repeat unit in each chain consists of two tetrahedra with the formula $(\text{TO}_3)^{2-}$. The octahedral layer contains the 6-8-coordinated M cations. Their coordination polyhedra share edges to form either laterally continuous sheets or wide bands of polyhedra that are also parallel to the *c* axis within the (100) plane. The four structure types reported for most silicate pyroxenes (*C2/c*, *P2₁/c*, *Pbca*, *Pbcn*) differ principally in the manner in which the octahedral and tetrahedral layers are linked. Pyroxenes with other space groups such as *C2*, *P2*, *P2/n*, and *P2₁ca* have also been reported, but in general such occurrences are limited. These space groups are all symmetrical subgroups of either *C2/c* or *Pbca* (e.g., Ohashi and Finger, 1974a; Matsumoto, 1974; W. Brown, 1972).

Pyroxenes with the monoclinic space group *C2/c* are probably most important volumetrically. This group includes Ca-rich pyroxenes near the $\text{CaMgSi}_2\text{O}_6$ (diopside)- $\text{CaFe}^{2+}\text{Si}_2\text{O}_6$ (hedenbergite) join in the pyroxene quadrilateral, sodium-rich pyroxenes such as $\text{NaAlSi}_2\text{O}_6$ (jadeite) and $\text{NaFe}^{3+}\text{Si}_2\text{O}_6$ (acmite), and chemically variable calcic pyroxenes referred to as augites/salites/fassaites. The *Pbca* and *P2₁/c* space groups are characteristic of the low-Ca or Fe-Mg quadrilateral pyroxenes. The former includes orthorhombic varieties such as bronzite or hy-

¹ The prefix "A" indicates that the table is located in the Appendix.

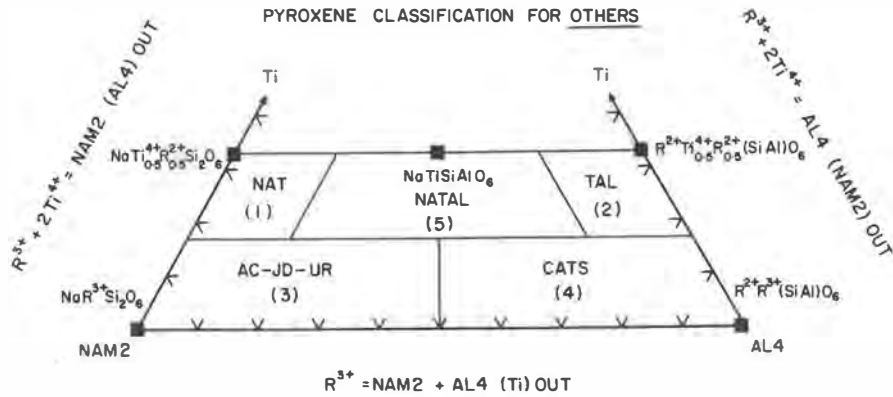


Fig. 2. The pyroxene Others quadrilateral (after Papike *et al.*, 1974). See text of paper for discussion.

persthene whereas the latter includes monoclinic pyroxenes such as pigeonite or clinohypersthene. The orthorhombic *Pbcn* space group is restricted to compositions near MgSiO_3 , and includes a non-querchable polymorph of enstatite that exists only at elevated temperatures ($\sim 1000^\circ\text{C}$). The space groups *P2/n* and *P2* were reported for the chemically complex omphacites (Clark and Papike, 1968; Matsumoto *et al.*, 1975; Curtis *et al.*, 1975), *C2* for Li-rich pyroxenes such as spodumene (Clark *et al.*, 1969),

and *P2₁ca* for two lunar orthopyroxenes (Smyth, 1974a; Steele, 1975).

The schematic I-beam diagrams (Fig. 4) of Papike *et al.* (1973) summarize the topologic differences among the four principal structure types of pyroxenes. These diagrams, which are based on the "ideal" models presented by Thompson (1970), depict the pyroxene structure as tetrahedral-octahedral-tetrahedral "I-beam" units whose infinite dimension lies parallel to *c*. In each I-beam, two tetrahedral

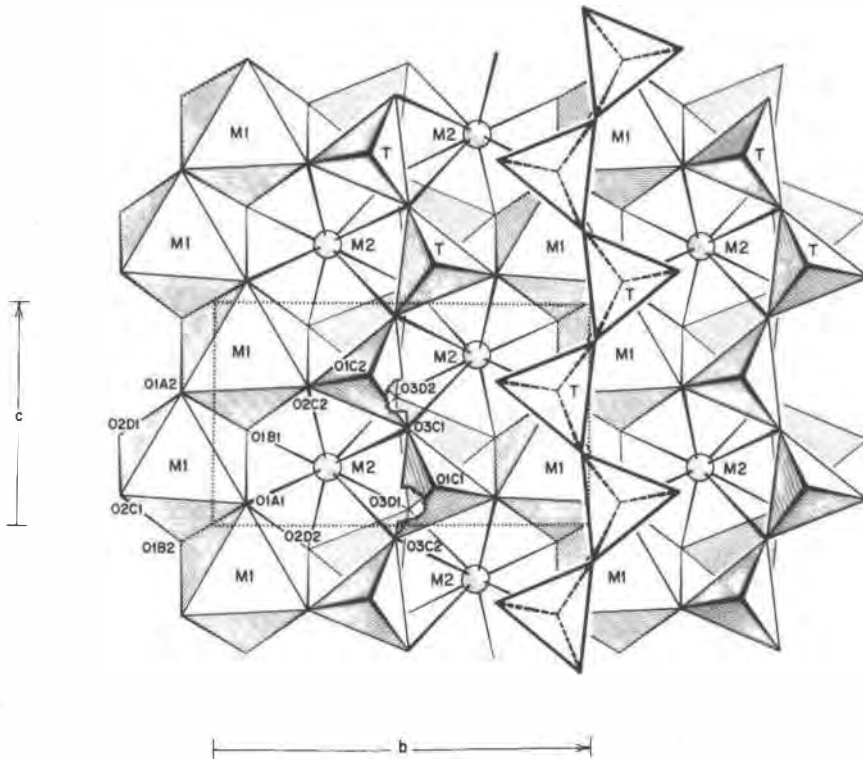


Fig. 3. The crystal structure of *C2/c* pyroxene (diopside) projected onto the (100) plane. Atom nomenclature is after Burnham *et al.* (1967).

units point inward and are cross-linked by octahedrally-coordinated cations. These tetrahedral–octahedral–tetrahedral units are highly stylized, and the correspondence between them and a real pyroxene structure is shown in Figure 5.

The symbols within the I-beam units provide information on the symmetry and orientation of individual coordination polyhedra. The A's and B's of the tetrahedral layers refer to two symmetrically-distinct chains: that is, chains that are kinked by different amounts and/or those whose tetrahedra are distorted differently. The absence of this notation indicates that the chains in adjacent layers within one I-beam unit are symmetrically equivalent and

are related to 2-fold axes of rotation parallel to b . The O or S notation within the tetrahedral layers refers to the rotational aspect of the chains, as originally defined by Thompson (1970) for regular polyhedra. The completely rotated (*i.e.*, $O_3-O_3-O_3 = 120^\circ$) O and S configurations shown in Figure 6 are based on a close-packed arrangement of oxygen atoms with a tetrahedral to octahedral edge ratio of 1:1. Cubic close-packing of oxygen atoms (ABCABC...) produces a tetrahedral–octahedral configuration referred to by Thompson (1970) as an O rotation, whereas hexagonal close-packing produces a S rotation. In an O rotation, the basal triangular faces of the tetrahedra (those approximately parallel to bc)

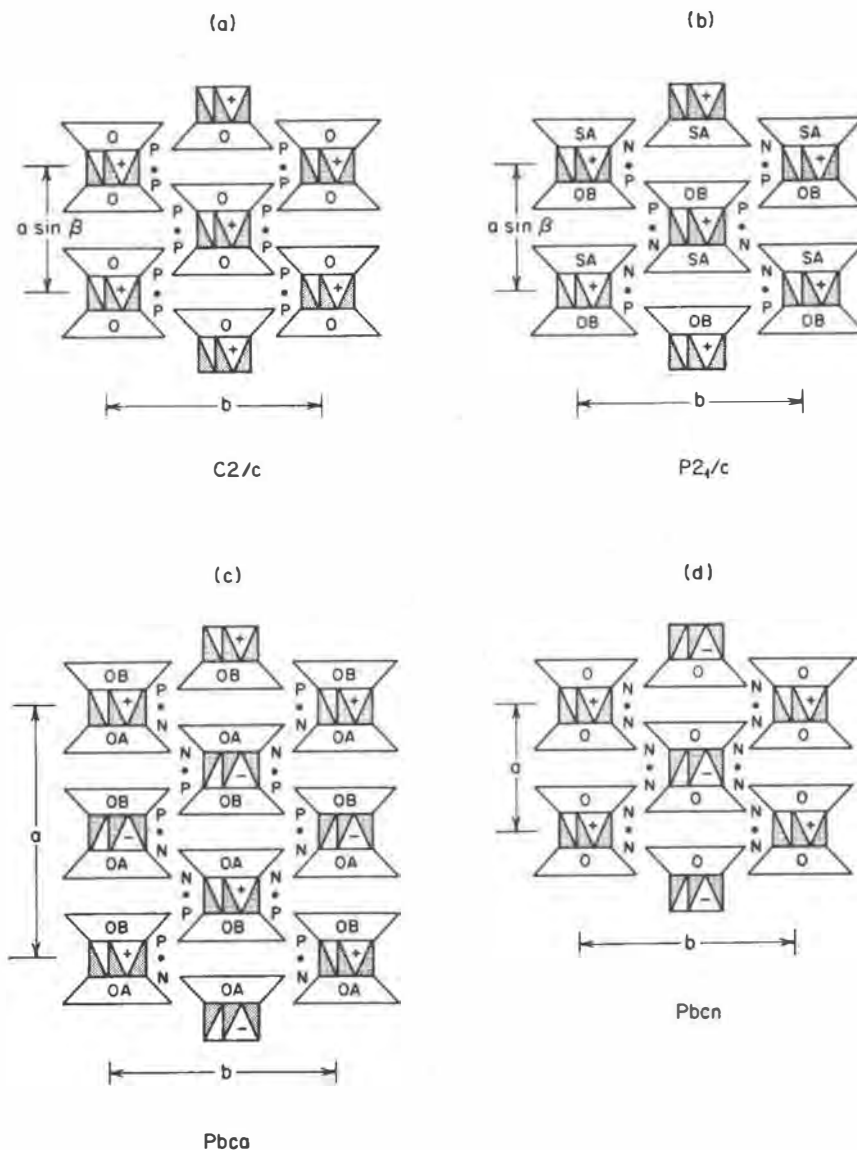


Fig. 4. I-beam diagrams of the four pyroxene structure types. See text of paper for explanation of symbols.

have an orientation opposite to the triangular faces of the octahedral strip to which they are linked through apical O1 oxygen atoms. In a S-rotation, the triangular faces of the octahedra and tetrahedra that are joined through O1 have the same orientation. The completely rotated O and S configurations represent the geometric extremes produced by rotating tetrahedra in the chains in opposite directions about imaginary lines passing through oxygen O1 and perpendicular to the (100) layer. Fully extended chains ($O3-O3-O3 = 180^\circ$; Fig. 6c) are possible only in an ideal structure with a tetrahedral to octahedral edge ratio of $\sqrt{3}:2$. In the structures of real silicate pyroxenes, the tetrahedral chains approach and achieve

full extension ($O3-O3-O3 = 180^\circ$), but they are never kinked by an amount as extreme as 120° (Table A4).

The positive (+) and negative (-) symbols in the octahedral layers refer to the "skew," "tilt," or direction of stagger of the layer with respect to a right-handed set of crystallographic axes. Within a single layer each octahedron has a pair of triangular faces that lie approximately parallel to (100). The apices of the upper and lower face of each pair are oriented in an opposite sense, but all triangular faces on one side of an octahedral layer point in the same direction (Fig. 3, 6). In a positive (+) octahedral strip, the apices of the upper triangular faces point in a +c di-

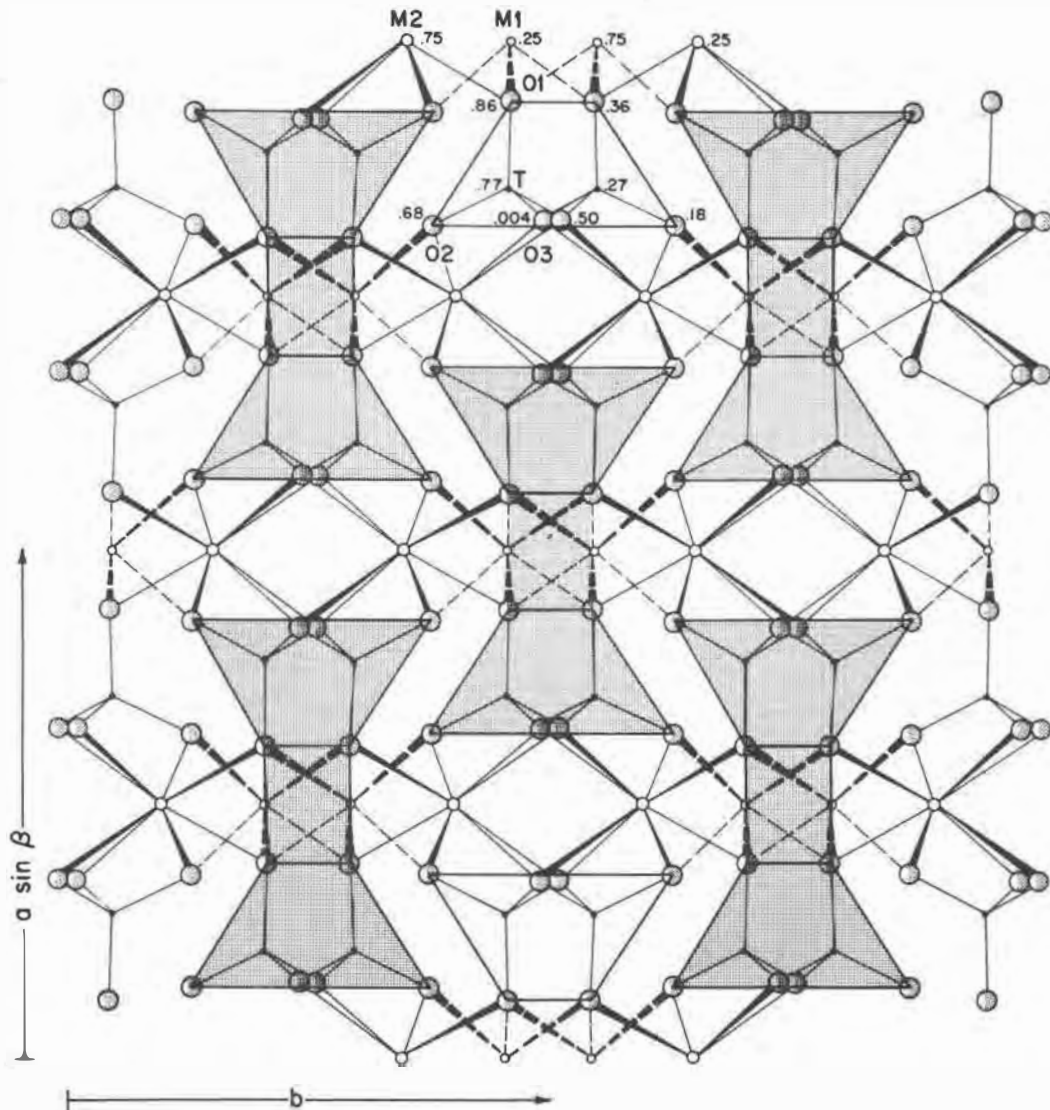


Fig. 5. The crystal structure of $C2/c$ pyroxene projected down $[001]$. Shaded areas outline I-beam units depicted in Fig. 4.

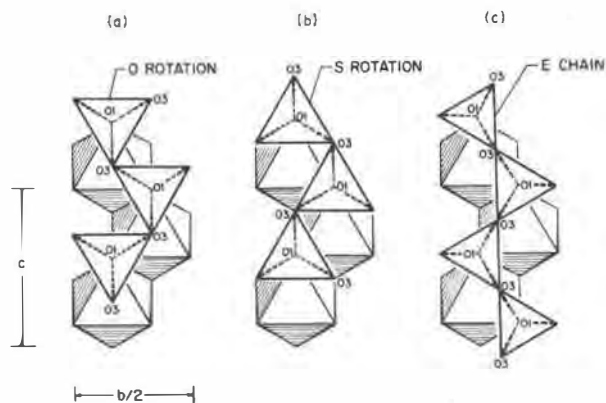


Fig. 6. Complete O and S rotations and extended (E) chain configuration for an ideal pyroxene structure. Note difference in size of tetrahedra in (a) and (b) vs. (c).

rection, *i.e.* away from the eye of the reader in Figure 4; in a negative (–) strip, the apices point in a $-c$ direction, *i.e.* toward the eye of the reader in Figure 4.

Thompson (1970) pointed out in his parity rule that because of geometrical considerations, there are only certain ways that tetrahedral layers can be combined in a structure. His statement follows: "This rule derives from the regularity of the polyhedra and affects the nature of the rotations of adjacent tetrahedral strips in a given tetrahedral layer. If two such strips are both rotated in the same sense then the two octahedral strips (one above and one below the tetrahedral layer) to which they are joined across (100) must both have a 'tilt' or skew of the same sense. If the rotations are in opposite senses then the tilts must be in opposite senses." Geometrical models for ideal, completely-rotated pyroxene structure (Fig. 7) show that violation of the parity rule results in a mismatch between tetrahedral and octahedral layers. All of the tetrahedral layers in the *Pbcn* pyroxene structure and the A layers in the *Pbca* pyroxene structure contain parity violations. Examination of the tetrahedra within an A layer of the *Pbca* structure shows that all have the same sense of rotation (O), even though the octahedral layers on either side of it have skews of the opposite sense. Despite the parity violation in real *Pbcn* and *Pbca* pyroxene structures, linkage between adjacent octahedral and tetrahedral layers is achieved largely by extension or straightening of the A tetrahedral chains relative to the B chains and by distortion of the cation polyhedra. Papike and Ross (1970) suggested a similar mechanism for the amphibole gedrite. Veblen and Burnham (1978) also discussed in considerable detail the tetrahedral misfit in various pyroboles (including pyroxenes).

The P and N symbols (after Sueno *et al.*, 1976) be-

tween the I-beams describe the structural configuration around the M2 site (Fig. 8). They refer to the relative orientations of triangular faces parallel to (100) of octahedra and tetrahedra that are joined laterally through O2 oxygen atoms. (Recall that for O and S rotations, the relative orientations of triangular faces of tetrahedra and octahedra joined through O1 oxygen atoms were important.) In an N configuration, the basal triangles of the lateral tetrahedral chain point in a direction opposite that of the octahedral faces to which they are joined through O2 atoms. In a P configuration, the triangular faces of the tetrahedra and octahedra joined through O2 are similarly oriented. This notation is identical to the U · D notation presented by Papike *et al.* (1973). For example, a D · U or U · D combination in a horizontal row is equivalent to an N symbol, whereas a U · U or D · D combination in a horizontal row produces a P symbol. The N–P symbol thus describes the relative orientations between an octahedral layer and the tetrahedral chains above and below it. It also provides information on the number of shared edges and size of the M2 polyhedron. The complete symbol for each M2 site includes two letters and a dot, which represents the position of the M2 cation. Each N indicates an edge shared between the M2 octahedron and a tetrahedron. The M2 octahedron in those structures with a $\frac{N}{N}$ configuration is relatively small because it shares two edges with tetrahedra. The $\frac{P}{P}$ configuration produces the largest (most open) M2 coordination polyhedron and appears to be the most stable arrangement because no polyhedral edges are shared. In ideal close-packed structures that exhibit no parity violations, only combinations of O with P and S with N are possible.

Referring again to Figure 4, we can now examine systematically the differences among the four structure types. The monoclinic *C2/c* pyroxene structure has octahedral stacking sequence $(+c/3)(+c/3)(+c/3)\cdots$ and all O (or all S) rotations of the tetrahedral chains. There is only one type of chain, and those in adjacent tetrahedral layers are related by a 2-fold axis of rotation parallel to *b*. In this ideal model, the tetrahedra and M2 octahedra share no edges. The orthorhombic *Pbca* structure has octahedral stacking sequence $(+c/3)(+c/3)(-c/3)(-c/3)(+c/3)\cdots$, which produces zero displacement parallel to *c* for each four octahedral layers. There are two symmetrically distinct tetrahedral chains, and those in the A layer, which is located between octahedral layers with different skews, exhibit parity violations. The M2 octahedron shares one edge with

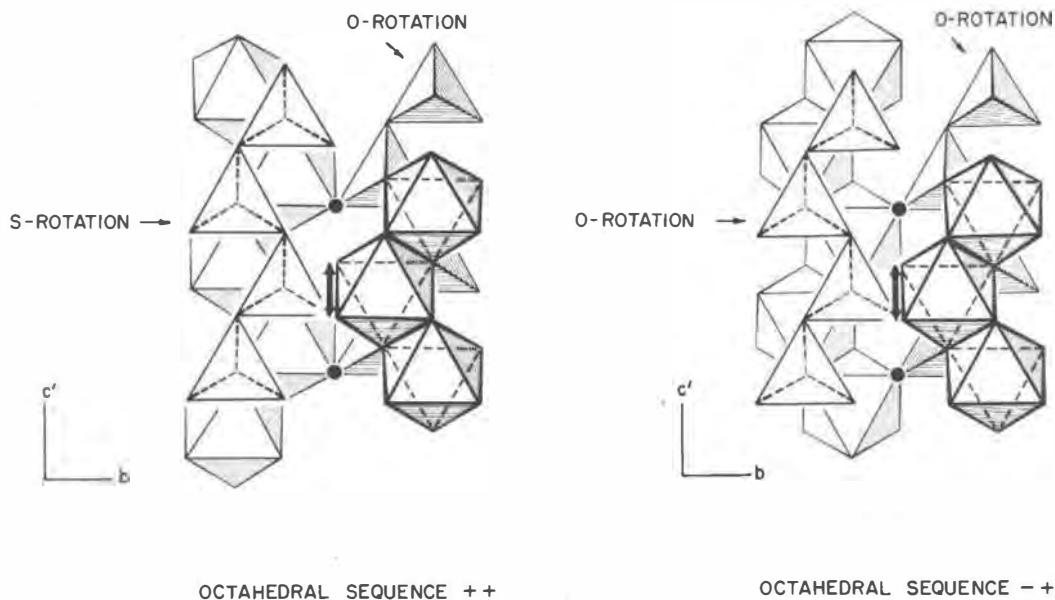


Fig. 7. Stacking sequences for ideal, completely-rotated pyroxene structures. Arrows in both figures show the degree of mismatch between tetrahedra and octahedra in hypothetical structures with parity violations (after Papike *et al.*, 1973).

adjoining tetrahedra. The monoclinic $P2_1/c$ structure has octahedral stacking sequence $(+c/3)(+c/3)(+c/3)\dots$. It contains symmetrically distinct chains in adjacent tetrahedral layers: the A chain is S-rotated and the B chain is O-rotated. No parity violations are present, and the M2 octahedron shares one edge with a tetrahedron as in the $Pbca$ structure. The orthorhombic $Pbcn$ space group has the stacking sequence $(+c/3)(-c/3)(+c/3)(+c/3)(-c/3)\dots$ and one type of tetrahedral chain, which is O-rotated. Because the octahedral skew changes in adjacent layers, all of the

tetrahedral layers exhibit parity violations. The M2 octahedron shares two edges with adjacent tetrahedra.

The stacking arrangements and possible space groups for pyroxenes were also examined by Pannhorst (1979) and Law and Whittaker (1980). Pannhorst (1979) presented a new classification in which pyroxene structures are described in terms of various stacking sequences of layer-like subunits, the smallest of which are termed O layers (oxygen layers). Law and Whittaker (1980) examined further Thomp-

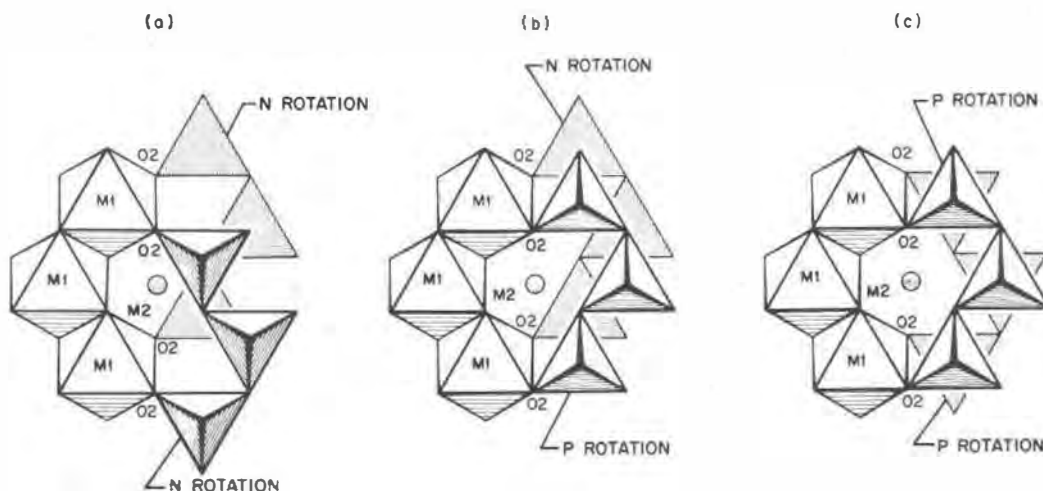


Fig. 8. Configuration of tetrahedral chains around the M2 site in an ideal pyroxene structure (after Sueno *et al.*, 1976). See text of paper for discussion of N and P rotations.

son's (1970) models for both pyroxenes and amphiboles.

Structural details

The coordination polyhedra in all pyroxene structures include 4-coordinated tetrahedra that contain the T cations and 6–8-coordinated polyhedra that contain the M cations. In the four principal structure types there are two types of M sites, labelled M1 and M2 (Table A5). In *C2/c* and *Pbcn* space groups, these sites occur in special positions on 2-fold axes of rotation parallel to *b*, whereas in the *Pbca* and *P2₁/c* structures they occupy general positions. In the *P2/n* space group reported for omphacite, there are four symmetrically distinct M sites, each of which occupies a special position on a 2-fold axis of rotation parallel to *b*. The T cations occupy general positions in all five space groups. There is only one symmetrically distinct T site in the *C2/c* and *Pbcn* structures, whereas there are two in the other three space groups. In the *Pbca* and *P2₁/c* pyroxene structures, the more extended chain with the smaller tetrahedra is referred to as the A chain, whereas the more kinked chain with the larger tetrahedra is referred to as the B chain. Except for the *P2/n* pyroxenes, there is only one type of tetrahedron within a given tetrahedral layer and adjacent tetrahedra along the chain are related by a *c* glide. The *P2/n* pyroxene structure has only one type of chain, but adjacent tetrahedra within each chain are not equivalent.

The basic coordination of both anions and cations in the four principal space groups varies only slightly. Each symmetrically distinct T cation is coordinated by one O1, one O2, and two O3 oxygen atoms (Fig. 3). The O1 anions are referred to as apical oxygen atoms, and the O3 anions as bridging oxygen atoms because they are shared between adjacent tetrahedra in the chains. The M1 cation is coordinated by four O1 and two O2 anions that have a fairly regular octahedral configuration. The coordination of M2 varies from 6 to 8 and depends on the size of the cation occupying the site. It ranges from eight when M2 is occupied by the large Ca and Na atoms (*C2/c* structures) to seven (some *P2₁/c* pigeonites) and six (orthorhombic *Pbca* pyroxenes or Li-rich *C2/c* or *C2* pyroxenes) when it is occupied by smaller Fe and Mg (or Li) atoms. Although there are minor variations among the different space groups, in the *C2/c* pyroxenes the O1 oxygen atom is coordinated by two M1, one M2, and one T cation; O2 by one M1, one M2, and one T cation; and O3 by two M2 and two T cations in the Ca and Na series and by

one M2 and two T cations in the Li series. In terms of classical Pauling bond strengths, O1 is approximately charge-balanced, O2 is highly underbonded, and O3 is highly overbonded. The apparent charge imbalances are largely eliminated by variations in cation–oxygen bond distances: for example, bonds to the underbonded O2 oxygen atoms are typically shortened (strengthened) whereas those to the overbonded O3 atoms are lengthened (weakened). The bond strengths and valency sums reported for pyroxenes by Clark *et al.* (1968, 1969), Ferguson (1974), and Hawthorne and Ito (1977) are in accord with these observations. The calculations in each of these three studies included a modification of Pauling's original electroneutrality principle in which variations in cation–anion distances were also taken into account.

The tetrahedral layer

In the end-member pyroxene structures, the mean T–O bond length of Si-bearing tetrahedra ranges from 1.618 to 1.644 Å (Table 2). The shortest of the four tetrahedral distances (1.585–1.612 Å) is usually Si–O2 whereas the longest involves the bridging O3 anions, with the exception of CaTs and the *C2/c* Li pyroxenes. The mean of the bridging bond distances is larger than that of the non-bridging distances, and in general the difference between the two means (Δ) is smallest for the *C2/c* Li pyroxenes with monovalent M2 cations and largest for the *C2/c* Ca pyroxenes with divalent M2 cations. The Δ 's for the *Pbca* and *P2₁/c* structures are intermediate between these two groups. Among the various pyroxene structures, the shorter bridging distances are associated with larger Si–O3–Si (Fig. 9) and O3–O3–O3 angles. The Si–Si distances within the chains vary between 3.01 and 3.13 Å, with the nearest approaches occurring in the highly kinked B chains of clino- and ortho-enstatite (Fig. 9). The 3.01 Å distances are close to the lower limit of the Si–Si non-bonded contacts discussed by Hill and Gibbs (1979). In the paragraphs that follow, we discuss some of the factors that are believed to contribute to the distortion and bond length variations in silicate tetrahedra. Specifically, we consider the effects of shared polyhedral edges, of the size and electronegativity of nontetrahedral cations, and of the coordination and local electrostatic environment of the oxygen atoms. In general, the relative importance of the various factors cannot be specified, and in many instances the variations are suitably explained either on the basis of a modified version of Pauling's electrostatic valence rule (*e.g.*, Baur, 1971) or on the basis of generally more realistic

Table 2. Average interatomic distances in ordered silicate pyroxenes. Crystal data given in Table A4

No.	Pyroxene Name	Space Group	Mean T-O ^a			Mean M1-O			Mean M2-O			Reference
			T cation	Distance (Å)	Q.E. ^b	M cation & Coordination	Distance (Å)	Q.E.	M cation & Coordination	Distance (Å)	Q.E.	
1.	CaNiSi ₂ O ₆	C2/c	Si	1.634	--	Ni(6 oxy)	2.072	--	Ca(8 oxy)	2.494	--	Schlenker et al. (1977) ^c
2.	diopside	C2/c	Si	1.634	1.0067	Mg(6 oxy)	2.077	1.0052	Ca(8 oxy)	2.498	--	Clark et al. (1969)
3.	CaCoSi ₂ O ₆	C2/c	Si	1.634	--	Co(6 oxy)	2.102	--	Ca(8 oxy)	2.506	--	Schlenker et al. (1977) ^c
4.	hedenbergite	C2/c	Si	1.635	1.0059	Fe ²⁺ (6 oxy)	2.130	1.0045	Ca(8 oxy)	2.511	--	Cameron et al. (1973)
5.	johannsenite	C2/c	Si	1.644	1.0055	Mn ²⁺ (6 oxy)	2.173	1.0052	Ca(8 oxy)	2.530	--	Freed and Peacor (1967)
6.	jaeite	C2/c	Si	1.623	1.0055	Al(6 oxy)	1.928	1.0151	Na(8 oxy)	2.469	--	Prewitt and Burnham (1966)
7.	ureyite	C2/c	Si	1.624	1.0037	Cr(6 oxy)	1.998	1.0088	Na(8 oxy)	2.489	--	Clark et al. (1969)
8.	acmite	C2/c	Si	1.628	1.0033	Fe ³⁺ (6 oxy)	2.025	1.0135	Na(8 oxy)	2.518	--	Clark et al. (1969)
9.	NaScSi ₂ O ₆	C2/c	Si	1.632	1.0036	Sc(6 oxy)	2.102	1.0110	Na(8 oxy)	2.564	--	Hawthorne and Grundy (1973)
10.	NaNSi ₂ O ₆	C2/c	Si	1.632	1.0026	In(6 oxy)	2.141	1.0106	Na(8 oxy)	2.568	--	Hawthorne and Grundy (1974)
11.	spodumene ^{d,e}	C2/c	Si	1.618	1.0047	Al(6 oxy)	1.919	1.0149	Li(6 oxy)	2.211	1.2177	Clark et al. (1969)
12.	LiFe ³⁺ Si ₂ O ₆	C2/c	Si	1.620	1.0030	Fe ³⁺ (6 oxy)	2.031	1.0135	Li(6 oxy)	2.249	1.231	Clark et al. (1969)
13.	LiScSi ₂ O ₆	C2/c	Si	1.624	1.0030	Sc(6 oxy)	2.107	1.0132	Li(6 oxy)	2.289	1.2399	Hawthorne and Grundy (1977)
14.	Zn ₂ Si ₂ O ₆	C2/c	Si	1.618	1.0029	Zn(6 oxy)	2.145	1.0204	Zn(4 oxy)	1.982	--	Morimoto et al. (1975)
15.	Ca tschermakite ^d	C2/c	½Si, ½Al	1.686	1.0089	Al (6 oxy)	1.947	1.0144	Ca(8 oxy)	2.461	--	Okamura et al. (1974)
30.	orthoenstatite	Pbca	SiA	1.628	1.0099	Mg(6 oxy)	2.076	1.0089	Mg(6 oxy)	2.149	1.0488	Hawthorne and Ito (1977)
			SiB	1.640	1.0052							
31.	Zn ₂ Si ₂ O ₆	Pbca	SiA	1.621	1.0037	Zn(6 oxy)	2.128	1.0181	Zn(6 oxy)	2.265	--	Morimoto et al. (1975)
			SiB	1.629	1.0040							
32.	orthoferrosilite	Pbca	SiA	1.626	1.0071	Fe ²⁺ (6 oxy)	2.135	1.0087	Fe ²⁺ (6 oxy)	2.228	1.0706	Sueno et al. (1976)
			SiB	1.637	1.0046							
57.	clinoenstatite	P2 ₁ /c	SiA	1.628	1.0080	Mg(6 oxy)	2.078	1.0086	Mg(6 oxy)	2.142	1.0430	Ohashi and Finger (1976)
			SiB	1.638	1.0050							
55.	clinoferrosilite	P2 ₁ /c	SiA	1.623	1.0058	Fe ²⁺ (6 oxy)	2.137	1.0083	Fe ²⁺ (6 oxy)	2.224	1.0641	Burnham (1966)
			SiB	1.635	1.0051							
68b.	Mn ₂ Si ₂ O ₆	P2 ₁ /c	SiA	1.632	1.0057	Mn(6 oxy)	2.177	1.0088	Mn(6 oxy)	2.281	1.0746	Tokonami et al. (1979)
			SiB	1.637	1.0039							
70.	protopyroxene	Pbcn ^f	Si	1.622	1.0073	Mg(6 oxy) ^g	2.096	1.0106	Mg(6 oxy) ^h	2.186	1.142	Smyth and Ito (1977)

^aInteratomic distances refer to room temperature structures except for protoenstatite.

^bQuadratic elongation parameter of K. Robinson et al. (1971).

^cFrom Ribbe and Prunier (1977)

^dSpace group may be C2.

^eTrue formula for crystal studied is (Li_{0.952}Fe_{0.048})²⁺(Fe_{0.952}Fe_{0.048})³⁺Si₂O₆²⁺

^fM1 contains Sc and M2 contains Li. See Table A7 for site occupancies.

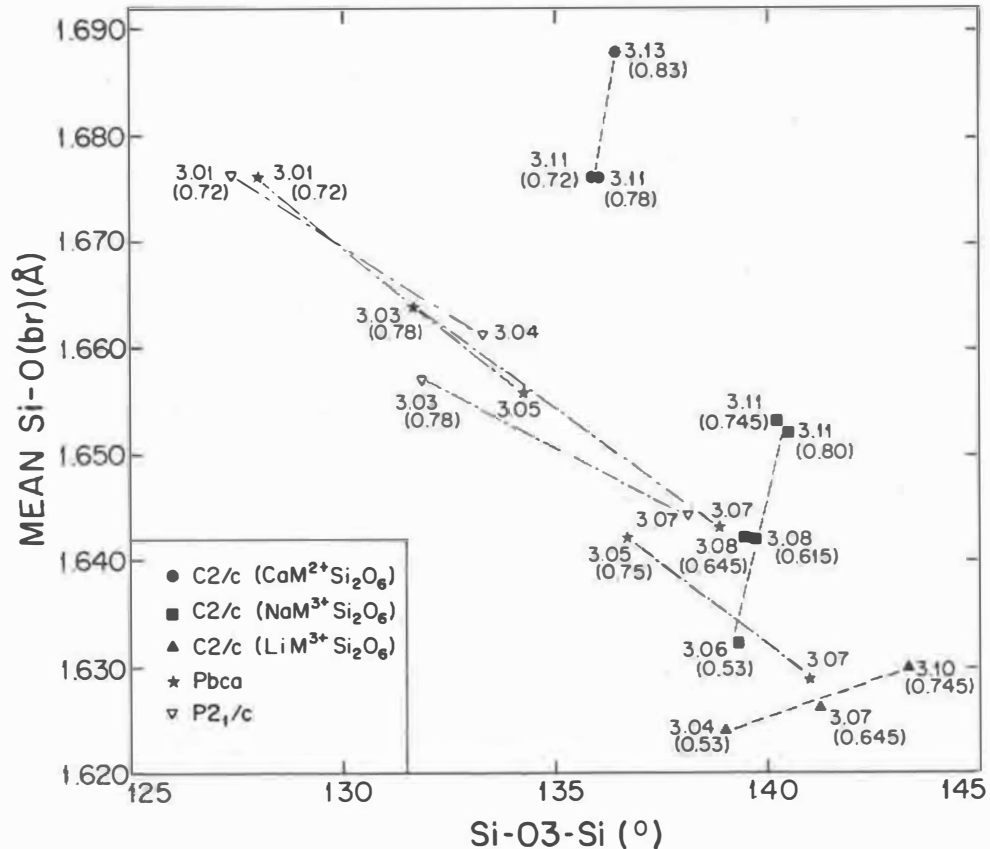


Fig. 9. Variation of mean Si-O(br) bonds with Si-O3-Si angles. Samples plotted include 1-14, 30-32, 55, and 57 (Table A4). Dashed lines are regression curves for $C2/c$ pyroxenes with $M2 = \text{Li}$ (triangles), $M2 = \text{Na}$ (squares), and $M2 = \text{Ca}$ (solid circles). Dot-dashed lines connect data points for A and B chains in $PbcA$ pyroxenes (stars) and $P2_1/c$ pyroxenes (inverted triangles). Numbers associated with each symbol are distances between adjacent Si cations within the same tetrahedral chain. Numbers in parentheses are ionic radii for $M1$ cations in $C2/c$ pyroxenes and $M1 + M2$ in $PbcA$ and $P2_1/c$ pyroxenes.

covalent bonding models (e.g., Gibbs *et al.*, 1972; Hill and Gibbs, 1979).

We used the quadratic elongation parameter of K. Robinson *et al.* (1971) to characterize systematically the tetrahedral distortion in the various pyroxenes (Table 2). In the $C2/c$ structures, the tetrahedra of the Ca pyroxenes exhibit the largest distortion whereas those of the Li pyroxenes have the smallest. Within each of the three groups, the quadratic elongation parameter decreases with increasing radius of the $M1$ cation. In the $PbcA$ and $P2_1/c$ structures, tetrahedra in the iron end-members are slightly less distorted than those in the magnesium end-members (Table 2), and in addition, the A tetrahedra are more distorted than the B. The greater distortion of the A tetrahedron is largely a result of the cation-cation repulsion across the O-O edge shared with the $M2$ coordination polyhedra. The approach of $M2$ and SiA is much closer (2.78-2.85 Å) than that of either $M2$ and SiB or $M2$ and Si (~3.10 to ~3.30 Å). In the

$PbcA$ pyroxenes, the increased distortion also reflects the response of the structure to the parity violation in the A tetrahedral layer. This distortion of individual tetrahedra within the chains is one of the mechanisms that promotes linkage between the tetrahedral and octahedral layers (Papike *et al.*, 1973) and is discussed in more detail in a later section.

The variation in Si-O(br) bond lengths can be explained on the basis of local charge balance considerations. Clark *et al.* (1969) related the increase in bridging distances in the three groups of $C2/c$ pyroxenes directly to the strength of the $M2$ -O bonds. They stated that "Each O3 bridging oxygen coordinates two $M2$ cations (except when $M2$ is Li), and assuming the electrostatic attraction between O3 and Ca^{2+} to be greater than that between O3 and Na^+ , then the Si-O3 bridging bonds would be expected to lengthen in the Ca clinopyroxenes." Ribbe and Prunier (1977), in addition, noted the positive correlation in $C2/c$ pyroxenes between the length of the Si-

O(br) bonds and the sum of classical Pauling bond strengths (s) at the O3 anion. For example, in the Ca group the bond strength at the O3 oxygen = 2.50 valence units because each O3 is bonded to two Si and two Ca atoms. For the Na pyroxenes, s at O3 = 2.25 v.u., and for the Li pyroxenes, s at O3 = 2.17 v.u. From these values we would expect the $C2/c$ Li group to exhibit the shortest Si–O3 bonds and the smallest differences between the average bridging and non-bridging distances, as is observed. In the CaTs pyroxene, the relatively short bridging O3 bonds can be explained as a result of their being bonded to two (Si+Al) rather than to two Si cations.

The variation in Si–O bond lengths can also be rationalized by covalent bonding models such as extended Hückel molecular orbital (EHMO) theory (e.g., Brown *et al.*, 1969; Gibbs *et al.*, 1972; Tossell and Gibbs, 1977). Analysis of the TO_3^- oxyanions by EHMO theory involves computation of Mulliken bond overlap populations, $n(\text{Si–O})$, for individual bond distances. These $n(\text{Si–O})$ terms are related to the electron density between two bonded atoms, and larger overlap populations imply higher electron densities, greater binding forces, and hence are associated with shorter Si–O bond lengths. Because shorter bond lengths necessarily induce larger overlap populations during the calculations, each Si–O distance is usually set to a fixed value close to 1.63 Å. With this induced correlation eliminated, variations in $n(\text{Si–O})$ and therefore bond length are attributed to the effects of geometrical factors such as O–Si–O and Si–O–Si angles. In general, computations showed that larger $n(\text{Si–O})$ and shorter Si–O bonds are associated with larger Si–O–Si angles (e.g., Gibbs *et al.*, 1972), with larger O–Si–O angles (e.g., Louisnathan and Gibbs, 1972a), and with larger $(\text{O–Si–O})_3$, which is the mean of the three O–Si–O angles common to a bond (e.g., Louisnathan and Gibbs, 1972b). The change in bond overlap populations is apparently related to concomitant changes in both the σ - and π -bonding potentials of the atoms involved (Gibbs *et al.*, 1972). In Figure 9, we show the variation of mean Si–O(br) bond distance with Si–O–Si angle for selected end-member pyroxenes. The overall trend is as expected, even though the tetrahedral angles are undoubtedly affected by bonding of the O3 anions to non-tetrahedral cations. Shorter Si–O(br) bonds are associated with wider Si–O–Si angles.

Several researchers discussed the relationship between electronegativity and variations both in the Si–O bond length and in the difference between the Si–

O(br) and Si–O(nbr) distances (McDonald and Cruickshank, 1967; Brown and Gibbs, 1969, 1970; Baur, 1971). In 1967 McDonald and Cruickshank suggested that the formation of covalent bonds to non-tetrahedral cations would diminish the pi-bonding potential of the silicate ion, and as a consequence the difference between the bridging and non-bridging bonds should decrease as electronegativity of these cations increases. Brown and Gibbs (1969) noted that in $C2/m$ amphiboles longer Si–O(nbr) bonds are associated with the more electronegative cations, but Baur (1971) concluded that their arguments were not convincing since the comparisons did not involve strictly isostructural compounds. In the same study Baur compared four pairs of isostructural pyroxenes, each with different M1 cations, and concluded that no unambiguous trend attributable to electronegativities is present. We examined, in addition, variations in the Si–O(nbr) distances and Δ 's for $C2/c$ pyroxenes along the hedenbergite–ferrosilite join (Ohashi *et al.*, 1975) and for the Fe–Mg series of the $Pbca$ and $P2_1/c$ pyroxenes. In each of these groups the difference between the bridging and non-bridging Si–O bonds decreases with increasing electronegativity of the nontetrahedral cations. However, the decrease in Δ is affected as much, if not more, by significant decreases associated with the bridging distances as by increases in the non-bridging Si–O distances (e.g., Figs. 10b,c; 11b,c).

The mean Si–O distances in the $C2/c$, $Pbca$, and $P2_1/c$ space groups are also influenced by the size of the nontetrahedral cations. The variation is controlled largely by the behavior of the Si–O(br) bond lengths because the Si–O(nbr) distances either remain constant or increase slightly with increasing radius of the M1 and M2 cations (Figs. 10, 11). With increasing size of the octahedral layer, the mean Si–O distance in the $C2/c$ pyroxenes increases whereas that in the $Pbca$ and $P2_1/c$ pyroxenes decreases slightly (Fig. 12). In 1969 Morimoto and Koto suggested that the relationship between Si–O distances and the Fe/(Fe+Mg) content of orthopyroxenes was linear. However, Burnham *et al.* (1971) noted that the mean bridging distances of an orthopyroxene of intermediate composition fell on Morimoto and Koto's curves, but the mean of the non-bridging and hence that of all Si–O bonds did not. Figure 12 shows that there is a definite trend of decreasing mean Si–O distances with increasing Fe content of the octahedral layer, but the relationship in the $Pbca$ pyroxenes may not be linear as originally proposed. A similar but less well defined decrease occurs in

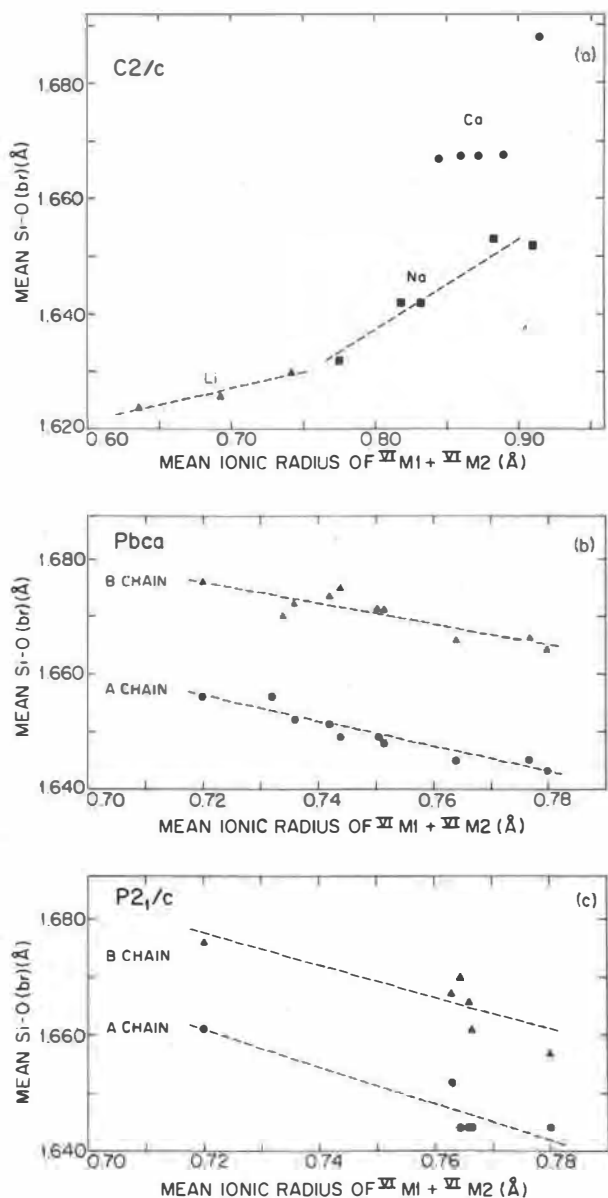


Fig. 10. Variation of mean Si-O(br) interatomic distance with mean ionic radius of ($^{VI}M1 + ^{VI}M2$). Note difference in scale of the abscissa in (a) vs. (b) and (c). Dashed lines are regression curves. (a) $C2/c$ pyroxenes. Triangles represent Li varieties; squares, Na varieties; circles, Ca varieties. Samples plotted include pyroxenes 1-13 (Table A4). (b) $Pbca$ pyroxenes. Triangles represent the B chain and circles, the A chain. Samples plotted include pyroxenes 30, 32, 35-38, 41, 42, 44, 46. (c) $P2_1/c$ pyroxenes. Triangles represent the B chain and circles the A chain. Samples plotted include pyroxenes 55, 57, 61, 64, 66, 67.

both chains of the $P2_1/c$ structure. In the $C2/c$ pyroxenes, the increase in Si-O bond lengths is much more pronounced than the variation in either the $Pbca$ or $P2_1/c$ structures. The systematic increase in size of the tetrahedra probably reflects both per-

turbations caused by the increasing size of the octahedral layer and differences in distortion of the tetrahedra. Brown and Shannon (1973) noted that mean bond lengths are approximately a linear function of bond length distortion. The general variations in the $C2/c$ pyroxenes are in accord with this observation; that is, the Ca pyroxenes have the largest and most distorted tetrahedra whereas the Li pyroxenes have the smallest and least distorted tetrahedra.

The variation of T-O distances vs. $Al/(Al+Si)$ is linear for $C2/c$ pyroxenes whose M2 sites are filled almost entirely by Ca. In Figure 13, we show only the variation for mean T-O, mean T-O(br), and mean T-O(nbr) distances, even though a linear relationship also exists for T-O2 distances (Clark *et al.*, 1968). The three open symbols associated with each regression curve in Figure 13 show how the relationship changes when there is less than one Ca (≈ 0.75 Ca+Na) per formula unit. The synthetic CaTs ($CaAlSiAlO_6$) studied by Okamura *et al.* (1974) does not lie on two of the three regression lines when it is plotted at $Al/(Al+Si) = 0.5$, and Hazen and Finger (1977a) suggested that the short range Al-Si ordering

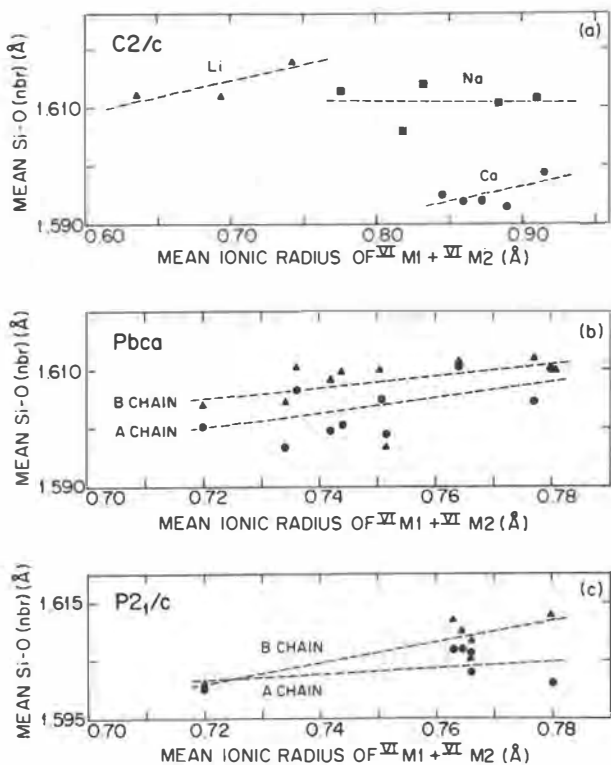


Fig. 11. Variation of mean Si-O(nbr) interatomic distance with mean ionic radius of ($^{VI}M1 + ^{VI}M2$). Diagram and symbols are analogous to Fig. 10 in all aspects.

reported by Grove and Burnham (1974) might explain its deviation.

In the *Pbca* pyroxenes, Al concentrates in the TB tetrahedron (Takeda, 1972b; Kosoi *et al.*, 1974; Brovkin *et al.*, 1975) because TB is inherently larger than TA and because it shares no edges with M2. This explanation was first used by Papike and Ross (1970) for the amphibole gedrite. The distribution of tetrahedral Al is inferred largely from the T-O distances. In those orthopyroxenes that contain tetrahedral Al, the mean TA-O bond lengths are relatively constant at approximately 1.627 Å, whereas the mean TB-O bond lengths increase significantly as the amount of tetrahedral Al in the formula increases. The relationship between T-O bond length and Al content is not as well defined as that for the *C2/c* clinopyroxenes, possibly because of the presence of submicroscopic exsolution lamellae and complex microstructures as suggested by Hawthorne and Ito (1977). They concluded that some of the Al represented in chemical analyses of orthopyroxenes occurs in incoherently diffracting microstructures, and thus

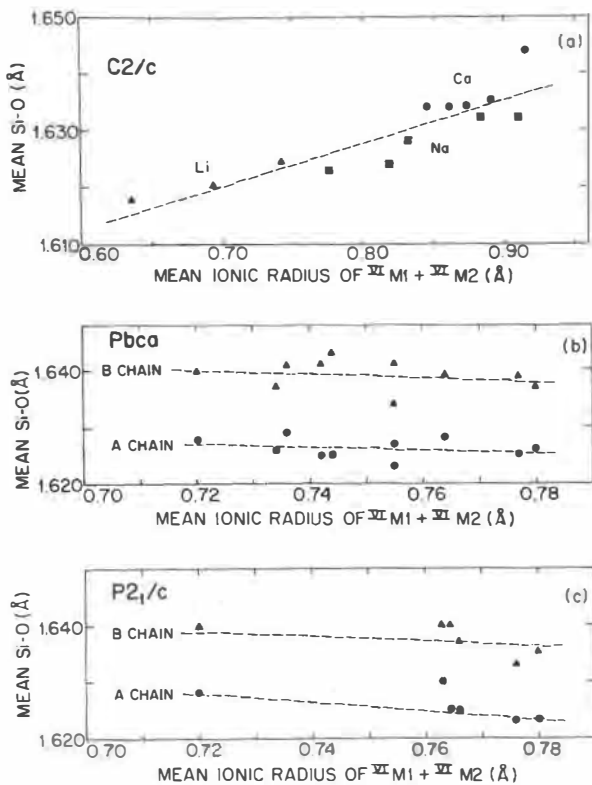


Fig. 12. Variation of mean Si-O interatomic distance with mean ionic radius of $(VI M1 + VI M2)$. Diagram and symbols are analogous to Fig. 10 in all aspects. Dashed lines are regression curves.

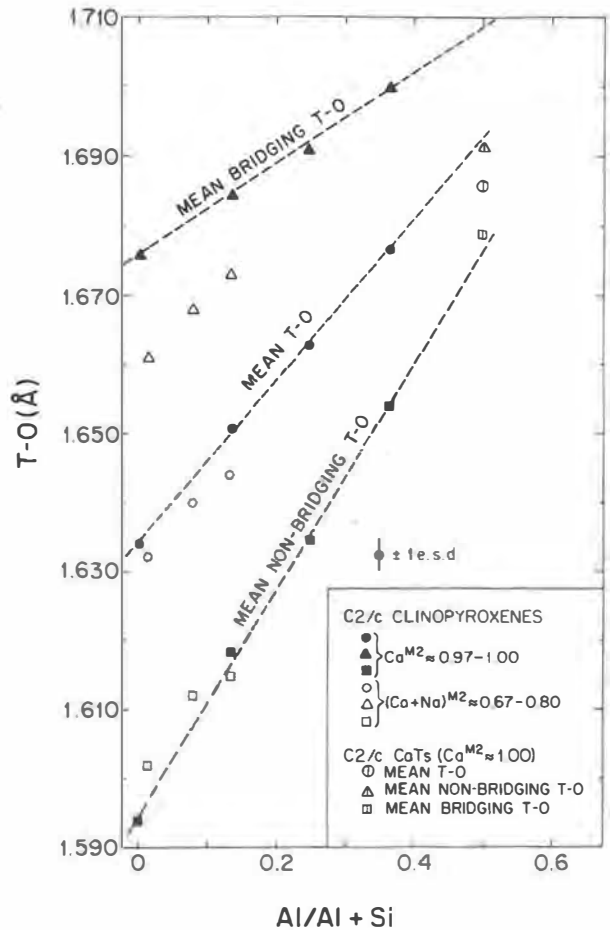


Fig. 13. Variation of T-O distances with $Al/(Al+Si)$. Dashed lines are regression curves for the four samples shown in solid symbols. Samples plotted include pyroxenes 2, 25-27 (solid symbols), 19, 20, 24 (open symbols) and 15 (open symbols with vertical lines). See Table A4.

does not contribute to the overall diffraction pattern of the host orthopyroxene.

The octahedral layer

The M1 octahedron and M2 polyhedron share edges to form either laterally continuous sheets or wide bands of polyhedra that lie parallel to the *c* axis within the (100) plane (Fig. 3). Each M1 octahedron shares two edges with other M1 octahedra to form zig-zag "chains" whose infinite dimension is parallel to *c*. The M2 polyhedra lie diagonally off to each side of these edge-sharing M1 octahedra.

The 6-coordinated M1 site accommodates divalent, trivalent, and tetravalent cations with ionic radii ranging from $\sim 0.53 \text{ \AA}$ (Al) to $\sim 0.83 \text{ \AA}$ (Mn). The variation in mean M1-O with the radii of constituent M1 cations is shown in Figure 14. The plot includes data

for the 15 ordered $C2/c$ pyroxenes, 10 disordered $C2/c$ pyroxenes (mostly augites), the Fe and Mg end-members for the $Pbca$ and $P2_1/c$ pyroxenes, and one $Pbcn$ protopyroxene. This diagram illustrates that the size of the M1 octahedron is dependent upon the radius of the M1 cation [as shown by Ribbe and Prunier (1977) for the $C2/c$ pyroxenes], and that it does not vary drastically among the four different structure types. The M1 octahedron appears to be the most important building-block in the pyroxene structure and it has a major effect on the detailed configuration of the M2 polyhedron and on the relative displacement and kinking of the tetrahedral chains linked to it. The trend in Figure 14 can also be used to determine if cation site assignments are grossly in error and if cation valences are properly assigned. For example, the two points connected by the horizontal line represent site occupancies calculated for Ti in two different valence states in a fassaite believed to contain considerable trivalent Ti (Dowty and Clark, 1973). The point on the left represents the mean ionic radius for a M1 occupancy of 0.48 Ti + 0.39 Mg + 0.13 Al, assuming that all of the Ti is tetravalent. The point on the right, which was calcu-

lated with all trivalent Ti, lies closer to the overall trend of the data and appears to be more reasonable. Dowty and Clarke concluded that this fassaite from the Allende meteorite contains 0.14 atoms of Ti^{4+} and 0.34 atoms of Ti^{3+} . The aberrant point (symbolized by an X), which plots above the curve at a radius = 0.75, represents a synthetic $C2/c$ zinc polymorph ($ZnSiO_3$) that has a rather distorted M1 octahedron and a tetrahedrally coordinated M2 cation (Morimoto *et al.*, 1975).

The variation of mean M1-O with mean radius of the M1 cations for the disordered $Pbca$ and $P2_1/c$ pyroxenes containing principally Fe and Mg is shown in Figure 15. The scale of the abscissa is expanded relative to Figure 14 in order to show the variation in detail. The regression curves for both structure types are almost parallel and that for the $Pbca$ pyroxenes is displaced only very slightly toward lower mean M1-O values at identical cation radii. When more than two cation species are present, the trend for the $Pbca$ pyroxenes shows more scatter, but is still well defined. In general, the synthetic Mg, Mn, Co, Zn orthopyroxenes (Hawthorne and Ito, 1977; Hawthorne and Ito, 1978; Morimoto *et al.*, 1975) plot near the

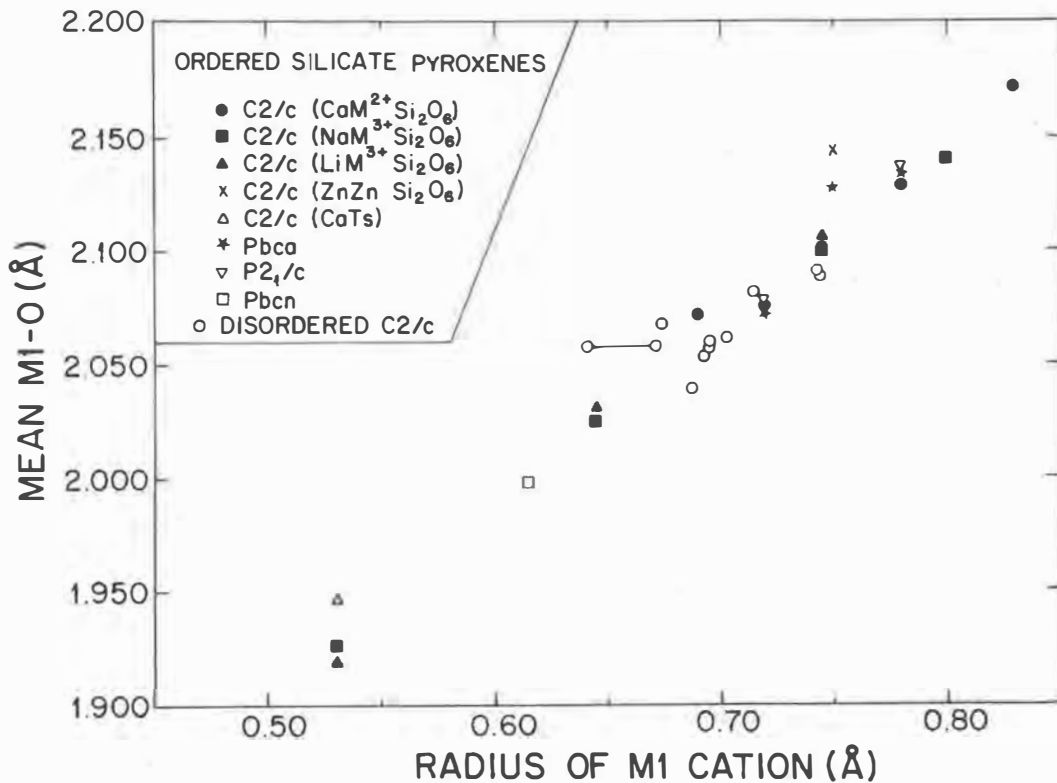


Fig. 14. Variation of mean M1-O with radius of the M1 cation. Samples plotted include ordered pyroxenes 1-15, 30-32, 54, 55, 69 and disordered pyroxenes 19-27, 29 (Table A4).

curve for the natural Fe-Mg *Pbca* orthopyroxenes.

Figure 16 is a plot of mean observed M1-O vs. predicted M1-O distances for the *C2/c* pyroxenes. The predicted M1-O is the sum of Shannon and Prewitt's (1969, 1970) ionic radii for the constituent cations and four-coordinated oxygen. Note that the trends for the calcic, sodic, and lithium pyroxenes each cut diagonally across the 45° line representing ideal predicted interatomic distances. The location of the lithium and sodic pyroxenes above the curve at short M1-O distances (= small M1 cations) indicates that observed values are larger than predicted—thus implying that the oxygen framework around the M1 site may be held open for small cations. Similarly, at longer M1-O distances, observed values are smaller than predicted—suggesting that the octahedra are somehow constrained.

The M2 site is 6-, 7-, or 8-coordinated, depending on the size of the cation occupying the site. It is coordinated by four non-bridging (two O2 and two O1) oxygen atoms in all of the structures; however, the number of O3 atoms varies between two and four depending on the relative displacement and kinking of the tetrahedral chains above and below the M2 site. For example, the *C2/c* structures that contain large M2 cations such as Ca or Na have four O3 oxygen atoms coordinating M2 because tetrahedral chains in adjacent layers are superimposed closely above each other. On the other hand, those *C2/c* pyroxenes with a small cation such as Li in M2 have only two O3 atoms within the first coordination sphere because the tetrahedral chains in adjacent lay-

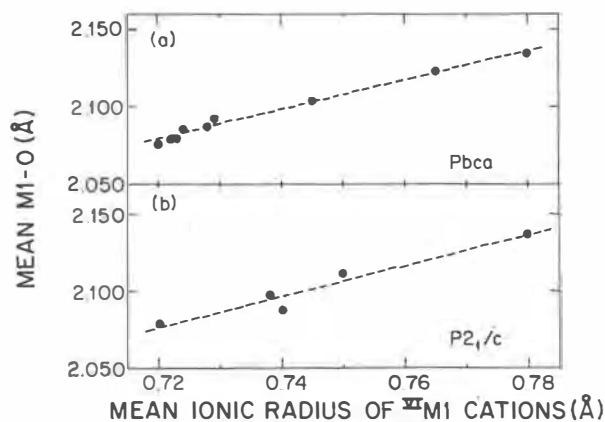


Fig. 15. Variation of mean M1-O interatomic distance with mean ionic radius of VI M1 cations. Pyroxenes shown contain principally (Fe+Mg) in M1 and (Fe+Mg+Ca) in M2. Dashed lines are regression curves. Samples plotted include 30, 32, 36-38, 41, 44, 46 (*Pbca* pyroxenes) and 55, 57, 61, 66, 67 (*P2₁/c* pyroxenes). See Table A4.

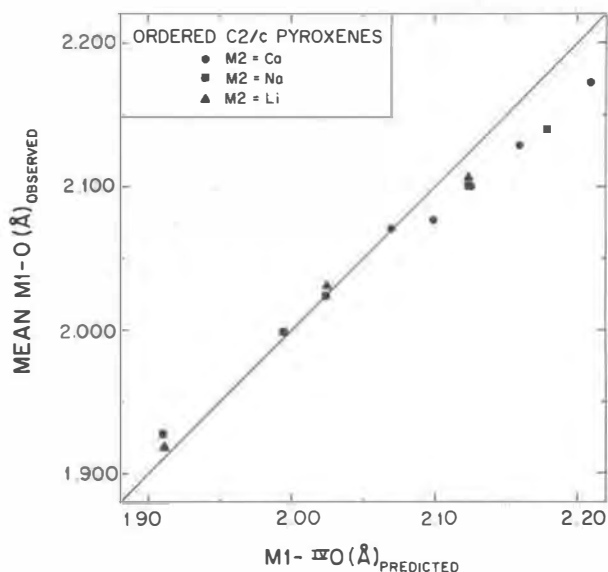


Fig. 16. Variation of observed mean M1-O with M1-O predicted from the sum of the ionic radius of the M1 cation and four-coordinated oxygen. The line drawn at 45° represents the hypothetical situation in which observed M1-O equals M1-O predicted from the sum of the radii.

ers are displaced by relatively large amounts in the *c* direction. The M2 site in the *Pbca* structure is 6-coordinated whereas that in the *P2₁/c* structures has been described as either 6- or 7-coordinated. Morimoto and Güven (1970) considered the M2 site in pigeonite to be 7-coordinated whereas other authors (e.g., Clark *et al.*, 1971; Güven, 1969) have considered it 6-coordinated. In many *P2₁/c* structures (e.g., clinoenstatite, Ohashi and Finger, 1976; pigeonite, Clark *et al.*, 1971, pigeonite, Ohashi and Finger, 1974b) the effective coordination is probably better described as six rather than seven because SiA approaches M2 more closely than does the seventh coordinating oxygen.

The radius of cations that occupy the M2 site in silicate pyroxenes ranges from ~ 0.72 (Mg^{VI}) to ~ 1.16 Å (Na^{VIII}). In *C2/c* pyroxenes, the mean M2-O distance increases with increasing radius of both the M2 and M1 cations. For identical M2 occupancy, the mean M2-O distance increases as size of the M1 cation increases (Fig. 17). For example, in the *C2/c* sodic pyroxenes where M2 = Na, the mean M2-O varies from 2.469 (M1 = Al; $r_{Al} = 0.53$ Å) to 2.568 Å (M1 = In; $r_{In} = 0.80$ Å). These variations in mean M2-O were also noted by Clark *et al.* (1969) and Ribbe and Prunier (1977), and the latter correlated them to the size of the M1 cation and to the size and charge of the M2 cation. Figure 18 shows the variation of mean M2-O distances with mean radius of

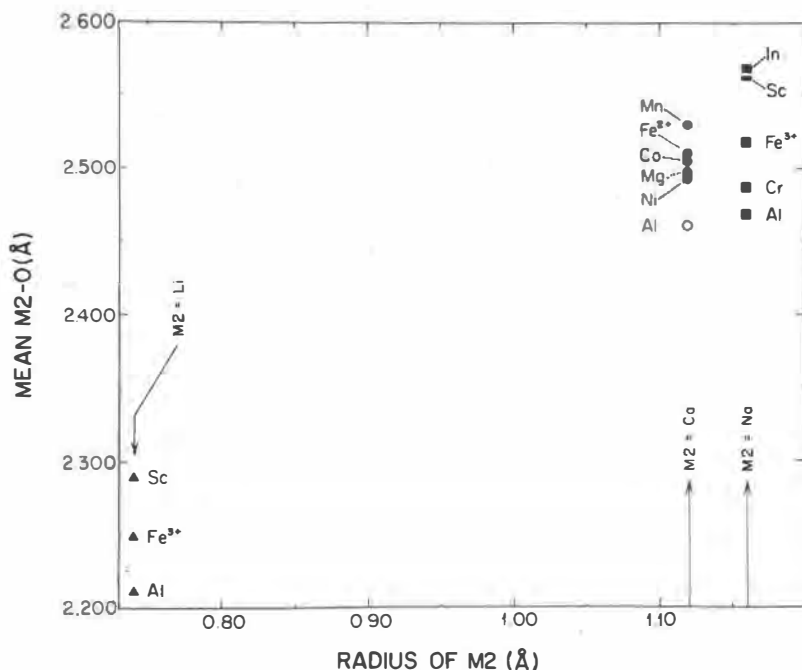


Fig. 17. Variation of mean M2-O interatomic distance with radius of the M2 cation in ordered $C2/c$ pyroxenes (after Ribbe and Prunier, 1977). Triangles represent Li pyroxenes; circles, Ca pyroxenes; squares, Na pyroxenes. Elemental labels associated with each data point indicate M1 occupancy. Samples plotted include 1-13, 15 (Table A4).

cations in M2 of disordered $Pbca$ and $P2_1/c$ pyroxenes. Although there is a positive trend for both space groups, the overall relationships are not as good as those for the M1 site. Some of the scatter may be due to the effects of chemically different microstructures in pyroxenes of these space groups, as Hawthorne and Ito (1977) suggested for the orthopyroxenes.

The relationship between mean M-O distances

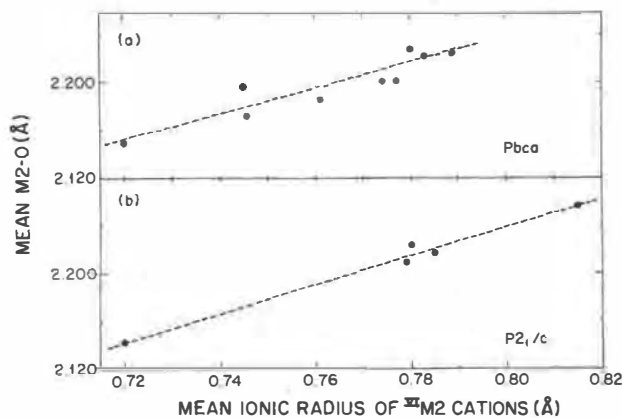


Fig. 18. Variation of mean M2-O with mean ionic radius of $M2$ cations for ordered and disordered pyroxenes of the $Pbca$ and $P2_1/c$ space groups. Dashed lines are regression curves. Samples plotted are the same as those in Fig. 15.

and the Fe-Mg content of orthopyroxene has been discussed repeatedly in recent pyroxene literature. There is general agreement that the size of the M1 and M2 octahedra increases with substitution of Fe for Mg, but the linearity of the relationships is a matter of controversy. Morimoto and Koto (1969) assumed a linear relationship between orthoenstatite and orthoferrosilite and produced two equations that they felt could be used to determine Fe-Mg ratios in the M1 and M2 sites. The hypersthene data of Ghose (1965) did not lie on the curves, but they re-interpreted his site occupancies using their equations. In a footnote at the end of their paper, Morimoto and Koto stated that Mössbauer work supported the original site occupancies in Ghose's orthopyroxene and that the relationships involving (Mg,Fe)-O distances are probably non-linear. Using a few additional data points, Burnham *et al.* (1971) concluded that the relationship for the M1-O distances was non-linear and that the mean M1-O value was an unreliable indicator of site occupancy. They also noted that the presence of calcium and the extreme distortion of the M2 polyhedron precluded use of mean M2-O distances as anything other than a crude indicator of site occupancy. Subsequently, Smyth (1973) stated that the average M1-O distance appeared to vary linearly. Kosoi *et al.* (1974) concluded that the average

interatomic distances in both the M1 and M2 octahedra were non-linear whereas Morimoto (1974) described the relationship between Fe–Mg content and mean M1–O and M2–O bond lengths as almost linear. Most recently, Hawthorne and Ito (1977) showed that plots of mean M1–O and M2–O bond lengths vs. constituent-cation radius for five Mg, Fe, Zn, Cu synthetic orthopyroxenes were extremely non-linear. Their detailed analysis of natural orthopyroxenes indicated that some of the octahedral trivalent cations do not occur in the host orthopyroxenes but reside in incoherently-diffracting microstructures. If these minor trivalent constituents are excluded from the calculation of cation radius, the variation of M1 appears to be linear. Their analysis of bond length variations in the M2 polyhedron was inconclusive because of the difficulty in evaluating precisely the effects of distortion on the bond lengths, and also because of the ambiguity in assigning calcium to the host crystal vs. the incoherently diffracting microstructures.

Ohashi *et al.* (1975) and Ohashi and Finger (1976) studied at room temperature the structural effects of varying M2 occupancy in a series of synthetic pyroxenes along the $\text{Mg}_2\text{Si}_2\text{O}_6$ – $\text{CaMgSi}_2\text{O}_6$ and $\text{Fe}_2\text{Si}_2\text{O}_6$ – $\text{CaFeSi}_2\text{O}_6$ joins. In both series, M1 occupancy is constant (either all Fe or all Mg), and M2 contains varying proportions of Ca and Fe or Ca and Mg. The Ca end-members of each series have $C2/c$ symmetry whereas the Ca-free end-members have $P2_1/c$ symmetry. In the CaFe–FeFe series, the change in space group at room temperature occurs between $\text{Wo}_{15}\text{Fs}_{85}$ and $\text{Wo}_{20}\text{Fs}_{80}$ or where M2 contains approximately 30–40% Ca (Fig. 19a). With decreasing Ca content, the four non-bridging bonds (involving two O1 and two O2 atoms) decrease whereas the four bridging (all O3) bond lengths increase. After the transition to $P2_1/c$ symmetry, the bonds to non-bridging oxygen atoms continue to decrease whereas the bridging oxygens split into two pairs, one of which continues to increase and one of which decreases. Ohashi *et al.* (1975) also concluded that the geometry of the M2 site does not represent an average structure because variations in the M2 quadrupole splitting indicate that the local configuration around the ferrous ion changes as the bulk chemical composition changes. The variation in mean bond lengths in the CaMg–MgMg series is shown in Figure 19b. Although the data are very limited, Ohashi and Finger (1976) suggested that the $P2_1/c$ to $C2/c$ transition should take place at a composition more Ca-rich than that in the CaFe–FeFe series, assuming that the chain angles vary in a similar manner in both series.

By any measure of distortion, the M1 octahedron in all pyroxene structures is much more regular than the M2 polyhedron. Distortion about M1 usually involves short interatomic distances to the underbonded O2 oxygen atoms. Among the $C2/c$ pyroxenes, the Ca pyroxenes have the least distorted M1 octahedra but there appears to be no well-defined relationship between size of the cation occupying M1 and distortion as measured by the quadratic elongation parameter (Table 2). The Fe- and Mg-bearing M1 octahedra in the $C2/c$, $Pbca$, and $P2_1/c$ space groups have similar quadratic elongation values, and the octahedra containing Fe^{2+} may be slightly more regular than those containing Mg. In the M2 polyhedra, interatomic distances to the bridging O3 oxygen atoms are usually longer than those to the non-bridging O1 and O2 anions. In the $Pbca$, $P2_1/c$, and $Pbcn$ pyroxene structures, the shortest M2 bonds are those involving O2 anions whereas in the $C2/c$ pyroxenes the shortest distances involve bonds to either O2 or O1 oxygen atoms. Hawthorne and Grundy (1977) discussed in detail the variation in Na and Li clinopyroxenes in terms of size of the cation occupying M1. Quadratic elongation parameters of 6-coordinated M2 octahedra in the $Pbca$ and $P2_1/c$ pyroxene structures are similar for both the Fe and Mg end-members, and the Fe-bearing M2 octahedra are more distorted than the Mg-bearing M2 octahedra. In both structure types, the irregular oxygen configuration around the M2 site relative to M1 is inherent to the pyroxene structure itself, and it is augmented only slightly by the presence of Fe.

Linkage between the octahedral and tetrahedral layers

The majority of cation substitutions in pyroxenes occur in the octahedral layer. Such substitutions affect the size of the layer and hence its linkage with the tetrahedral chains. The most obvious means of compensating the misfit simply involves extension or kinking of the O3–O3–O3 chain angle. Additional adjustments include distortion of the tetrahedra or a change in “out-of-plane” tilting (Cameron *et al.*, 1973). The latter mechanism involves tilting of the tetrahedra by movement of the O2 atoms farther from or closer to the plane containing the O3 atoms. At present there are no published data discussing the relative importance of chain straightening, tetrahedral distortion, and out-of-plane tilting in maintaining the linkage between the octahedral and tetrahedral layers. Variations involving the first two mechanisms are discussed in detail below, and Ohashi and Finger (1974c) reported that increased

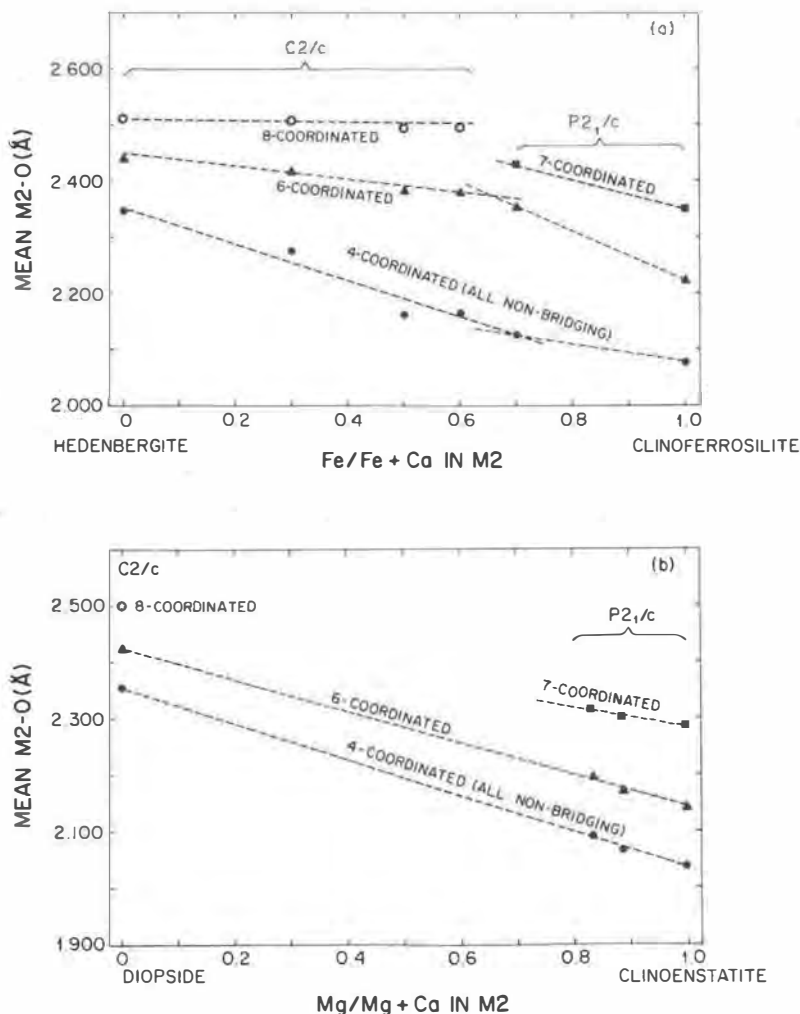


Fig. 19. Variation of mean M2-O with M2 occupancy for pyroxenes along the hedbergite-clinoferrrosilite and diopside-clinoenstatite joins. In both figures, note that the Ca-rich varieties have space group $C2/c$ whereas Ca-poor varieties have space group $P2_1/c$. Dashed lines are regression curves. The term non-bridging refers to bonds involving O1 and O2 anions. (a) Variation of mean M2-O with Fe/(Fe+Ca) in M2. Samples plotted include 4, 16-18, 55, 56 (Table A4). (b) Variation of mean M2-O with Mg/(Mg+Ca) in M2. Samples plotted include 2, 57-59.

out-of-plane tilting is highly correlated with increased kinking of the tetrahedral chain.

In the $Pbca$ and $P2_1/c$ structures, the chain angle increases significantly as the size of the octahedral layer, indicated by mean ionic radius of M1 and M2 cations, increases (Figs. 20, 21). In the $Pbca$ orthopyroxenes, the A chain straightens about 10° and the B chain about 5° as the mean radius of M1 + M2 increases from 0.72 to 0.78 Å. The greater rate of change in the A chain may be related to the increasing mismatch of the octahedral and tetrahedral layers caused by the parity violation in the A layers. The B chain appears to have a maximum O3-O3-O3 angle of $\sim 145^\circ$. In the $P2_1/c$ clinopyroxene struc-

tures both the A and B chains straighten by $\sim 17^\circ$ over the same range in ionic radii. The trend for $P2_1/c$ pyroxenes (Fig. 21) is less well defined, as most of the data points represent samples with Fe-rich compositions. The trends appear to be real, however, because a similar increase in chain angles occurs with the substitution of Ca for Mg in $P2_1/c$ structures along the $Mg_2Si_2O_6$ -CaMgSi₂O₆ join (Ohashi and Finger, 1976). In both the $Pbca$ and $P2_1/c$ structures, straightening of the tetrahedral chains is accompanied by a reduction in both mean Si-O and bridging Si-O distances, as discussed previously. The significant reduction in Si-O(br) distances (~ 0.12 - 0.14 Å for $Pbca$; ~ 0.12 - 0.19 Å for $P2_1/c$) is accom-

panied by small increases in O3–Si–O3 angles and decreases in O3–O3 distances in both the A and B chains.

Papike *et al.* (1973) noted a correlation between the mean ionic radius of the M1 and M2 cations and the O3–O3–O3 tetrahedral chain angle. Using data for eight $C2/c$ pyroxenes, they concluded that as the mean ionic radius of the M cations decreases, the chain straightens. In Figure 22, we plotted data for 18 $C2/c$ pyroxenes: in three series, M2 occupancy is constant (Ca = solid circles, Na = squares, Li = triangles), and in one series, M1 occupancy is constant (CaFe–FeFe pyroxenes = open circles). As the size of the M1 cation increases in each of the Ca, Na, and Li series (with the exception of $\text{LiAlSi}_2\text{O}_6$), the tetrahedral chain kinks. The increased kinking is an obvious result of the increase in size of the M1 octahedron and the O2–O2 octahedral edge (Fig. 3). In a detailed study of the Na and Li pyroxenes, Hawthorne and Grundy (1977) showed that linkage between the tetrahedral and octahedral layers in the Li pyroxenes is accomplished by expansion of the O3–O3 tetrahedral edge and by an increase in the O3–Si–O3 angle—thus producing an increase in chain length without greatly increasing the Si–O(br) distances. With the exception of $\text{NaInSi}_2\text{O}_6$ (and $?\text{NaCrSi}_2\text{O}_6$), the tet-

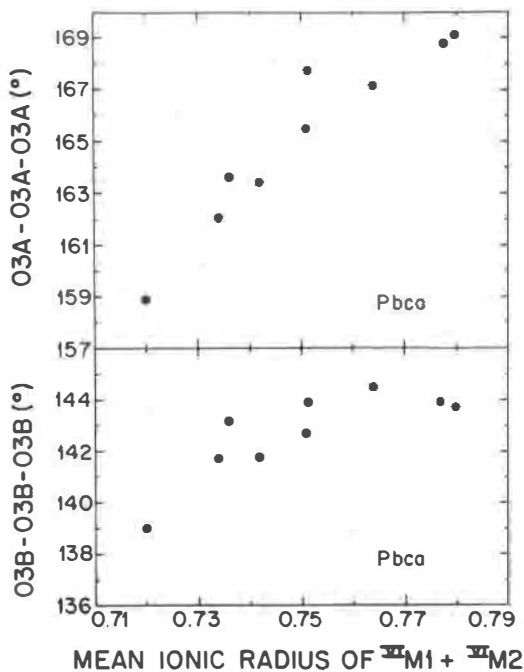


Fig. 20. Variation of A and B chain angles with mean ionic radius of ($^{VI}\text{M1} + ^{VI}\text{M2}$) in $Pbcu$ pyroxenes. Samples plotted are the same as those in Fig. 15a.

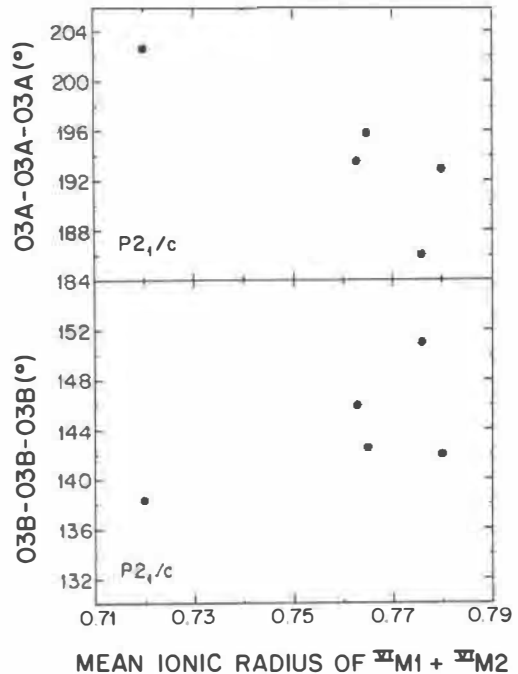


Fig. 21. Variation of A and B chain angles with mean ionic radius of ($^{VI}\text{M1} + ^{VI}\text{M2}$) in $P2_1/c$ pyroxenes. Samples plotted are the same as those in Fig. 15b.

rahedral chains in the Na pyroxenes straighten by increasing the Si–O(br) distances. In the Ca pyroxenes from M1 = Ni to M1 = Fe^{2+} there is essentially no change in the O3–Si–O3 angles or in Si–O(br) or O3–O3 distances. Between M1 = Fe^{2+} and M1 = Mn, there is a significant increase in both Si–O(br) and O3–O3 distances. An increase in the size of the M2 cation affects the tetrahedral chains in the various $C2/c$ pyroxenes differently. In structures containing divalent M2 cations, such as the CaFe–FeFe series studied by Ohashi *et al.* (1975), the O3–O3–O3 angle increases as the size of the M2 cation increases. Concomitant with this increase in the chain angle is an increase in the Si–O(br) bonds and a decrease in both the O3–O3 tetrahedral edge and the O3–Si–O3 angle. Among the pyroxenes with monovalent M2 cations such as the pairs LiFe–NaFe and LiSc–NaSc, the O3–O3–O3 angle decreases as the size of M2 increases. Concomitant with this decrease in both pairs is an increase in the Si–O(br) bonds and a decrease in O3–Si–O3. The O3–O3 tetrahedral edge remains approximately constant. As observed for the $Pbcu$ and $P2_1/c$ space groups, there is a generally antithetic relationship between O3–O3–O3 tetrahedral chain angle and mean T–O distances. That is, as the size of the octahedral layer (= mean radius of cations in M1

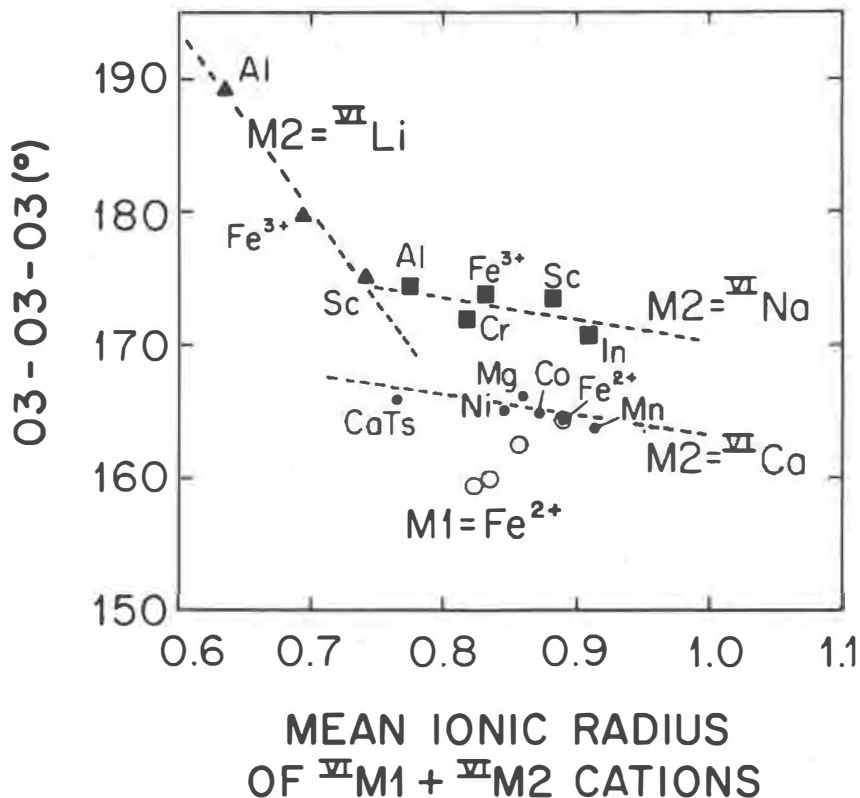


Fig. 22. Variation of O3-O3-O3 chain angle with mean ionic radius of ($^{VI}M1 + ^{VI}M2$) in $C2/c$ pyroxenes. Dashed lines are regression curves for pyroxenes with $M2 = Li$ (triangles), $M2 = Na$ (squares), and $M2 = Ca$ (solid circles). Elemental symbols associated with each data point indicate $M1$ occupancy. The four open circles refer to a $C2/c$ CaFe-FeFe series in which $M1 = Fe^{2+}$ and $M2$ contains varying amounts of Fe and Ca. Samples plotted include 1-5, 15 (solid circles), 6-10 (squares), 11-13 (triangles), and 4, 16-18 (open circles). See Table A4.

+ $M2$) in the $C2/c$ pyroxenes increases, the tetrahedral chain angle decreases and the size of the tetrahedra increases.

Expansion of the octahedral layer in the b direction also requires structural adjustment by the tetrahedral chains. The linkage is accomplished by distortion of the tetrahedra or by a mechanism referred to as c -axis rotation by Hawthorne and Grundy (1977). In a study of the relative importance of these mechanisms for the Li and Na series of $C2/c$ pyroxenes, Hawthorne and Grundy concluded that tetrahedral edge distortion is more important in the Na pyroxenes whereas c -axis rotation is the mechanism by which octahedral b axis expansion is accommodated in the Li pyroxenes.

Pyroxene structures at elevated temperatures and pressures

Studies of pyroxene structures at elevated temperatures and pressures are necessary to our understand-

ing of such phenomena as exsolution, solid solution, and phase transitions, which typically do not occur at room temperature or pressure. To date, six $C2/c$, two $Pbca$, and two $P2_1/c$ pyroxenes have been studied at temperatures up to $\sim 1000^\circ C$, and two $C2/c$ pyroxenes have been studied at pressures up to 45 and 53 kbar (Table A6).

The most important concept to evolve from the high temperature studies is that of differential polyhedral expansion: with increasing temperature, polyhedra containing different cations expand at different rates. In general, smaller mean thermal expansion coefficients are associated with cations having lower coordination number, higher valence, and higher electronegativity (Cameron *et al.*, 1973). The six $C2/c$ pyroxenes were examined at a series of temperatures up to $1000^\circ C$ (Cameron *et al.*, 1973; Finger and Ohashi, 1976). Over the temperature intervals studied, none of the pyroxenes underwent phase transitions and all exhibited regular, essentially linear increases in mean $M1-O$ and $M2-O$ interatomic

distances. The mean Si-O bond lengths in all structures remained approximately constant with increasing temperature. Mean thermal expansion coefficients for various bonds in the six pyroxenes increase in the following order: $\text{Si}^{4+}\text{-O} < \text{Cr}^{3+}\text{-O} < \text{Fe}^{3+}\text{-O} < \text{Al}^{3+}\text{-O} < \text{Fe}^{2+}\text{-O} < \text{Na}^+\text{-O} < \text{Mg}^{2+}\text{-O} < \text{Ca}^{2+}\text{-O} < \text{Li}^+\text{-O}$. The different expansion rates of the M and T polyhedra effect additional structural adjustments in order to maintain linkage between the octahedral and tetrahedral layers with increasing temperature. Mechanisms for this adjustment include straightening of the tetrahedral chains ($\sim 2\text{-}3^\circ$ over a maximum of 1000°C), small increases in the out-of-plane tilting ($\sim 0.5^\circ$ for diopside and ureyite), and very small distortions involving an increase in the O3-O3 interatomic distance.

Two orthopyroxenes, hypersthene (Smyth, 1973) and orthoferrosilite (Sueno *et al.*, 1976), were studied at a series of temperatures up to $\sim 1000^\circ\text{C}$. With increasing temperature the structural changes in both pyroxenes were regular and no phase transitions were observed. The mean Si-O distances showed either essentially no change or perhaps a slight decrease with increasing temperature. As temperature increased both the A and B tetrahedral chains straightened at a significantly higher rate than those in the $C2/c$ structures. In orthoferrosilite, the change in O3A-O3A-O3A was $\sim 10^\circ$ whereas O3B-O3B-O3B changed by $\sim 15^\circ$. Hypersthene exhibited a change of 5° in the A chain and 15° in the B chain. Maintenance of the linkage between tetrahedral and octahedral layers in these orthopyroxenes principally involves straightening of the tetrahedral chains. The rate of straightening becomes greater at higher temperatures, but at all times the B chain is more kinked than the A chain. The pronounced straightening of the tetrahedral chains changes the M2 coordination from six to seven and back to six at the highest temperatures studied.

Two $P2_1/c$ pyroxenes, pigeonite and clinohypersthene, were also examined up to $\sim 1000^\circ\text{C}$. Both structures exhibited a low (P) to high (C-centered) transition. The pigeonite (En = 39) transformed to $C2/c$ symmetry at $\sim 960^\circ\text{C}$ (Brown *et al.*, 1972) whereas the low clinohypersthene exhibited a first-order transition at $\sim 725^\circ\text{C}$ (Smyth, 1974b). The temperature of the transition decreases with increasing Fs component, as noted by Prewitt *et al.* (1971). The clinohypersthene, which was studied at four temperatures below the transition, exhibited a significant decrease in the mean Si-O distances of both the A and B tetrahedra with increasing temperature. As ex-

pected, the M1 and M2 polyhedra show much higher rates of expansion relative to the tetrahedra. Over a 700°C temperature interval, the A chain straightened by 7° and the B chain by 8° . In the pigeonite described by Brown *et al.* (1972) the changes in chain angle over 970°C were larger: A $\sim 12^\circ$ and B $\sim 23^\circ$.

These high-temperature studies provide additional insight into the miscibility between the high calcium and low calcium pyroxenes. Refinements of room-temperature structures documented significant differences in coordination of the M2 site in augite and pigeonite, and it is generally believed that these different configurations are responsible for the limited miscibility. With increasing temperature, the M2 polyhedra of pigeonite and the calcic pyroxenes (as indicated by the average of the diopside and hedenbergite structural data) become much more similar. In the $C2/c$ calcic pyroxenes the change involves the four M2-O3 distances and produces a M2 site that is more six-coordinated. The pigeonites, on the other hand, undergo a $P2_1/c$ to $C2/c$ transition with increasing temperature, and specific O3 anions in the first coordination sphere of M2 are different in the high and low temperature structures. The structural modifications in both pyroxenes are in a direction such that solid solution can be accomplished more readily (Cameron *et al.*, 1973).

Hazen and Finger (1977b) examined the structure of a fassaite at pressures up to 45 kbar, and Levien and Prewitt (1981) examined diopside at pressures up to 53 kbar. With increasing pressure, the mean interatomic distances decrease regularly (Fig. 23), and the various polyhedra compress differentially. This study on end-member diopside is more precise because of improved experimental methods and because the structure is ordered. Results indicate that the mean compressibility coefficients for interatomic distances increase in the following order: T-O $<$ M1-O $<$ M2-O.

Increasing pressure and increasing temperature have generally opposite effects on the crystal structure of pyroxenes. In addition, topologic changes produced by increasing temperature are expected to be similar to those produced by substitution of larger cations into a structure. Although these ideas are convenient generalizations, exceptions are numerous when structural variations are examined in detail. For example, in the $C2/c$ pyroxenes the mean Si-O distance remains approximately constant with increasing temperature whereas it changes significantly with variations in composition of the octahedral layer. The tetrahedral chain angle in $C2/c$ pyroxenes

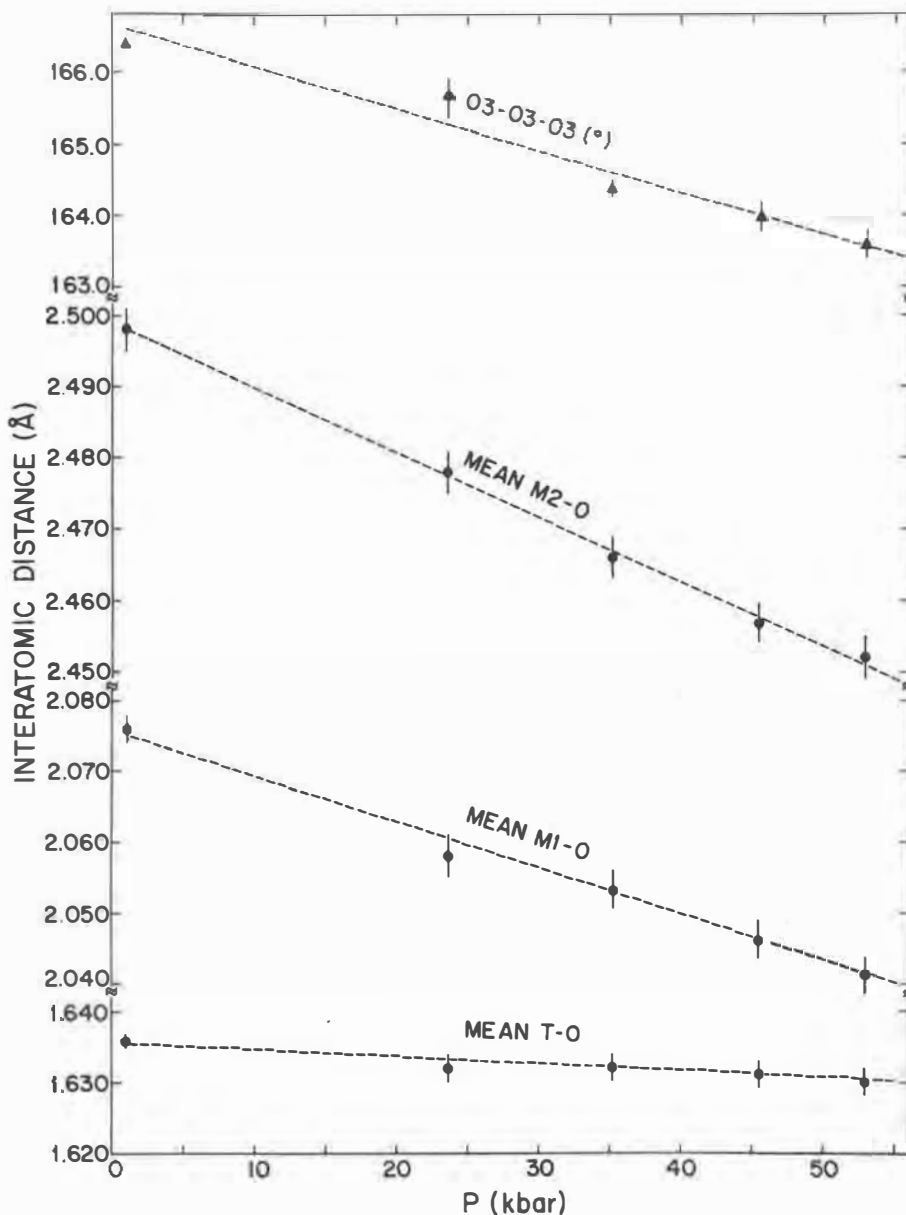


Fig. 23. Variation with increasing pressure of mean interatomic distances and O3-O3-O3 chain angle of diopside (data from Levien and Prewitt, 1981). Dashed lines are regression curves. Error bars represent ± 1 e.s.d.

decreases as the size of cations in the octahedral layer increases, whereas it increases with increasing temperature. Ohashi and Burnham (1973) pointed out differences in orientation of the strain ellipsoid caused by increasing temperature and increasing size of constituent cations. They noted that the direction of largest expansion associated with addition of Ca to a hedenbergite-ferrosilite series of structures is about

midway between the $+a$ and $+c$. This coincides with the smallest thermal expansion direction. Levien and Prewitt (1981) showed for diopside that only some of the structural parameters exhibit an inverse relationship with respect to temperature and pressure. Notably, mean M1-O, M2-O, O3-Si-O3, and O3-O3-O3 do whereas the β cell parameter and mean Si-O do not. The effects of temperature, pressure, and compo-

sition on the structures of both silicate and oxide minerals are discussed by Hazen and Prewitt (1977) and Hazen (1977).

Cation ordering in the octahedral layer

The distribution of cations between M1 and M2 is influenced by the configuration of anions around each site and by the ionic radius and electronegativity of the cations involved. In all pyroxene structures, the M2 polyhedron is larger and more distorted than M1 (Table 2); thus, we expect it to be enriched, relative to M1, in the larger cations and in those transition-metal cations that are stabilized in more distorted environments (Burns, 1970). The preference of Fe^{2+} for M2 over M1 in orthopyroxene was attributed by Ghose (1965) and Burnham *et al.* (1971) to the slightly enhanced covalent character of the Fe^{2+} -O bonds in the M2 site. In the $C2/c$ pyroxenes, larger cations such as Ca, Na, and Mn are usually assigned to M2 and the trivalent and tetravalent cations to M1 on the basis of size considerations. The same assignment is usually followed for the low-Ca pyroxenes ($P2_1/c$, $Pbca$, $Pbcn$ space groups), even though these cations are usually minor in abundance. In addition, in these three space groups the general preference of intermediate-sized cations for M2 is $\text{Mn} > \text{Zn} > \text{Fe}^{2+} > \text{Co} > \text{Mg}$ (Table A7). As a consequence, in the high-Ca clinopyroxenes there are few M2 sites available for Fe^{2+} because it is displaced by Ca. The distribution of cations described above explains why Fe/Mg ratios are typically greater in orthopyroxenes than coexisting clinopyroxenes. Although Fe^{2+} occurs in both the M1 and M2 sites, it preferentially occupies M2 in all pyroxene structures studied. The orthopyroxenes, in contrast, contain a relatively larger proportion of M2 sites available for Fe^{2+} occupancy simply because these structures do not contain large amounts of Ca. The M1 site in such coexisting clino- and orthopyroxenes contain generally similar amounts of Fe^{2+} and Mg (Ghose, 1965; also compare occupancies of coexisting pyroxenes #20 and #33).

The distribution of Fe and Mg between the two M sites in orthopyroxenes has been studied intensively because of its potential as a geothermometer. For a simple binary solution of Fe and Mg, the cation exchange between adjacent M1 and M2 sites can be written as follows:



Assuming ideal mixing on the individual sites (Muel-

ler, 1962), the distribution coefficient or equilibrium constant can be written for a specific temperature as

$$K_D = X_{\text{Fe}}^{\text{M1}}(1 - X_{\text{Fe}}^{\text{M2}})/X_{\text{Fe}}^{\text{M2}}(1 - X_{\text{Fe}}^{\text{M1}})$$

where

$$X_{\text{Fe}} = \text{Fe}^{2+}/(\text{Fe} + \text{Mg})$$

For orthopyroxenes, the distribution appears to be independent of pressure, and examples of K_D 's for samples equilibrated in a laboratory at 500°C and 1000°C are 0.051 and 0.235, respectively. The ion exchange process is relatively rapid as shown by Virgo and Hafner (1969), who reported "a steady value for Fe^{2+} in the M sites after 11 hours at 1000°C and after 50 hours at 500°C."

Virgo and Hafner (1969) assumed an ideal solution model and determined distribution isotherms for one orthopyroxene that equilibrated at 500°, 600°, 700°, 800°, 900°, and 1000°C. They then used the resultant isotherms to determine equilibration temperatures for a series of natural orthopyroxenes from both metamorphic and igneous rocks (Virgo and Hafner, 1970). Orthopyroxenes from granulites and plutonic rocks exhibit a relatively high degree of order (Fig. 24) and have K_D 's (~ 0.028) that correspond to an equilibration temperature of $\sim 480^\circ\text{C}$ whereas the few volcanic orthopyroxenes that they studied appear to have equilibrated between 500° and 600°C. Between $\text{Fe}/(\text{Fe}+\text{Mg}) = 0$ and 0.6, the points for the metamorphic and plutonic rocks scatter about the hyperbolic curves drawn for the ideal distribution, but in the Fe-rich samples with ratios greater than 0.6 the data deviate significantly from the ideal. The increased disorder of the Fe-rich samples may be, in part, a result of the presence of minor elements such as Ca or Mn that could displace Fe^{2+} on the M2 site. Snellenberg (1975) studied the effect of minor cations on the ordering of Fe and Mg in orthopyroxene. He showed that small concentrations of elements such as Ca or Mn do not seriously impair ordering in Fe-poor samples, but at higher concentrations their presence could contribute to the increased disorder in Fe-rich samples by displacing Fe on the M2 site. In addition, his calculations involving nearest-neighbor exchange reproduced the incomplete order usually observed in orthopyroxenes, and are consistent with the suggestion by Mueller (1969) that the energy barrier below 500°C which prevents complete ordering is the activation energy necessary for long-range cation migration. To account for the deviation of the Fe-rich samples from the ideal curves, Saxena and

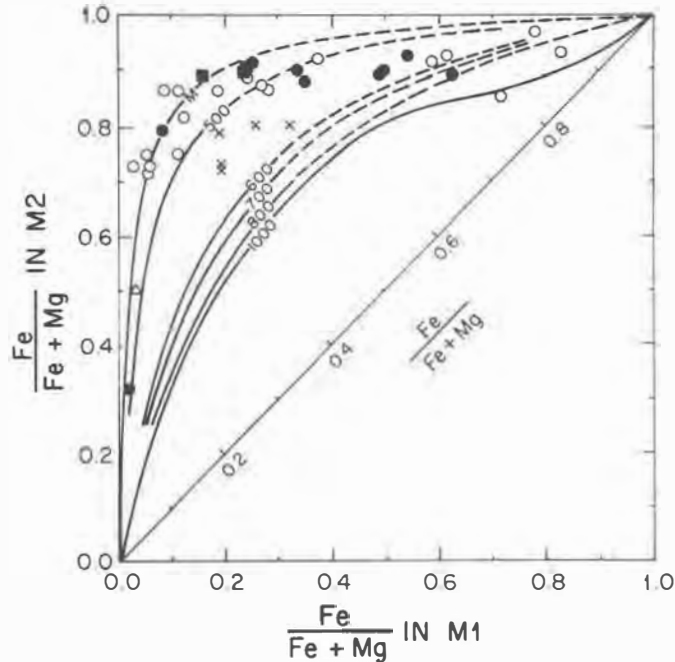


Fig. 24. Distribution of Fe^{2+} and Mg between the M1 and M2 sites of natural orthopyroxenes from granulites (open circles and squares), metamorphic iron formations (solid circles), and volcanic rocks (crosses). Data are taken from Virgo and Hafner (1969, 1970). Solid lines are equilibrium isotherms determined experimentally by Virgo and Hafner (1969).

Ghose (1970) used the regular solution model to reinterpret the data of Virgo and Hafner (1970) (Fig. 25). In addition, they also determined the complete Mg^{2+} - Fe^{2+} distribution isotherms at various temperatures in orthopyroxenes (Saxena and Ghose, 1971). In their model the equilibrium constant is redefined as:

$$K_a = X_{\text{Fe}}^{\text{M1}}(1 - X_{\text{Mg}}^{\text{M2}})/X_{\text{Mg}}^{\text{M1}}(1 - X_{\text{Fe}}^{\text{M2}}) \cdot f_{\text{Fe}}^{\text{M1}}f_{\text{Mg}}^{\text{M2}}/f_{\text{Mg}}^{\text{M1}}f_{\text{Fe}}^{\text{M2}}$$

where the f 's, referred to as "partial" activity coefficients, are determined empirically.

Saxena *et al.* (1974) studied by Mössbauer spectroscopy the Fe^{2+} -Mg distribution in four synthetic pigeonites over a range in temperatures. They showed that the Fe^{2+} -Mg distribution between the two M sites depends upon both temperature and concentration of Ca at the M2 site: the preference of Fe^{2+} for M2 increases with Ca content, but decreases with temperature. The pigeonites they studied contain equal amounts of Fe and Mg, and thus the resulting curves should be applied only to samples with $\text{Fe}/(\text{Fe}+\text{Mg}) \approx 0.5$. Their curves indicated equilibration temperatures of 700–860°C for pigeonites from eight lunar rocks.

McCallister *et al.* (1976) studied by X-ray methods the Fe^{2+} -Mg distribution in three Ca-rich pyroxenes at several temperatures. They conducted heating ex-

periments on the samples, and then used the resultant $\ln K_a$ vs. $1/T$ (°K) calibration curves to determine the equilibration temperature of the untreated material.

General chemical variations

In this section we consider some general aspects of pyroxene chemistry based on the 175 "superior analyses" (out of 406) presented by DHZ. Table A3 keys these analyses to DHZ by giving the page and column number on which each analysis is published. The table also gives the Quad-Others proportions (as discussed above), the General Name based on chemistry only (Table A2), and the best name for the Others component (Table A1).

In the total set of 175 superior analyses, only 59 had Others contents $<10\%$ and Mn <0.08 atoms per formula unit (a.f.u.). When these data are plotted on the standard quadrilateral (Fig. 26), several aspects of pyroxene chemistry are evident, even though we are considering only a small number of analyses. Complete solid solution is present between diopside and hedenbergite (the augites) and fairly complete solid solution occurs from enstatite to ferrosilite. Ferrosilite is not stable at low pressures (see DHZ for a review), and the most Fe^{2+} -rich sample in Figure 26 (DHZ, page 471, column 34) occurs in a metamor-

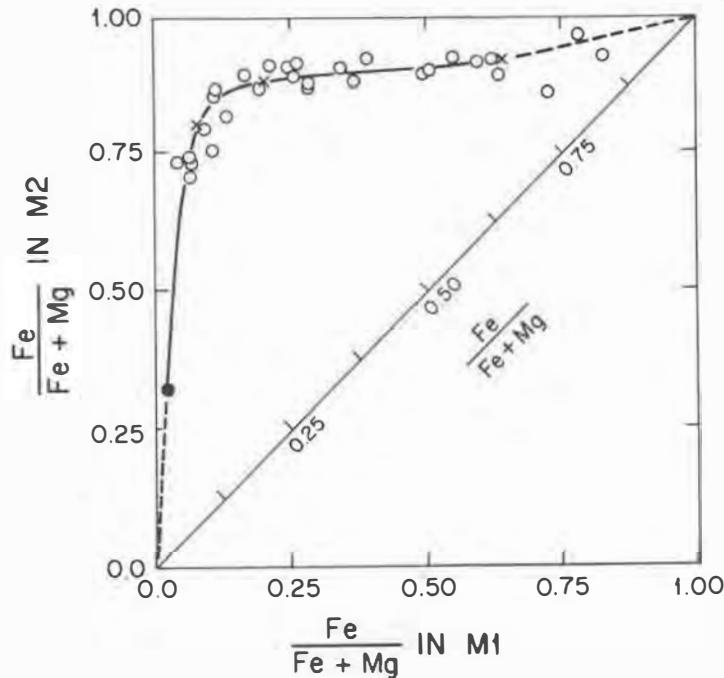


Fig. 25. Distribution of Fe^{2+} and Mg between the M1 and M2 sites in metamorphic orthopyroxenes. Data are from Virgo and Hafner (1970). The solid curve drawn through the crosses is based on a regular solution model (after Saxena and Ghose, 1970).

phosed iron-rich rock from Manchuria that probably formed at relatively high pressure. The Mg- Fe^{2+} pyroxenes (orthopyroxenes plus pigeonites) have Wo values of 0–10% whereas the augites have Wo values of ~35–50%. This is consistent with the miscibility gap between augites and Mg- Fe^{2+} pyroxenes being asymmetric, with the steeper solvus near the enstatite-ferrosilite join.

We can consider the 59 Quad pyroxenes in a slightly different way by reference to Figure 27, where we plot Ca (a.f.u.) vs. $X_{\text{Fe}} = \text{Fe}^{2+}/(\text{Fe}^{2+} + \text{Mg})$. This diagram shows the range in Ca content of the M2 site in augites and Mg- Fe^{2+} pyroxenes. In the Mg- Fe^{2+} pyroxenes, Ca is generally less than 0.19 a.f.u. whereas in the augites Ca ranges from 1.0 to 0.67 a.f.u. It is significant that, within analytical error, Ca does not exceed 1.0 a.f.u. This is consistent with the idea that Ca occupies only the M2 site and is too large for M1.

Figure 28 is a graphical representation of the charge balance equation for 105 pyroxenes in which the Others component is greater than 10%. The absence of points at <0.1 a.f.u. is an artifact of the selection of the data we plotted; low concentrations of Others have larger associated errors and thus are not plotted. However, it is interesting to examine the “gap” between 0.62 and 0.84 a.f.u. Because we know it is possible to have 100% solid solution between

Quad and Others (e.g., diopside-jadeite; Kushiro, 1969), this gap is probably a result of the analyses selected for presentation by DHZ and perhaps also the low abundance of such compositions in natural occurrences.

For the DHZ pyroxenes with Others >10%, Figure 29 is a simple summary of the Others components and of the ranges in solid solutions. The figure illustrates a complete range of Others between $\text{NaR}^{3+}\text{Si}_2\text{O}_6$ pyroxenes (acmite, jadeite, ureyite) and $\text{R}^{2+}\text{R}^{3+}(\text{SiAl})\text{O}_6$ (CATS) and between CATS and $\text{R}^{2+}\text{Tl}_{0.5}^{4+}\text{R}_{0.5}^{2+}(\text{SiAl})\text{O}_6$ (TAL). Very few points fall in the

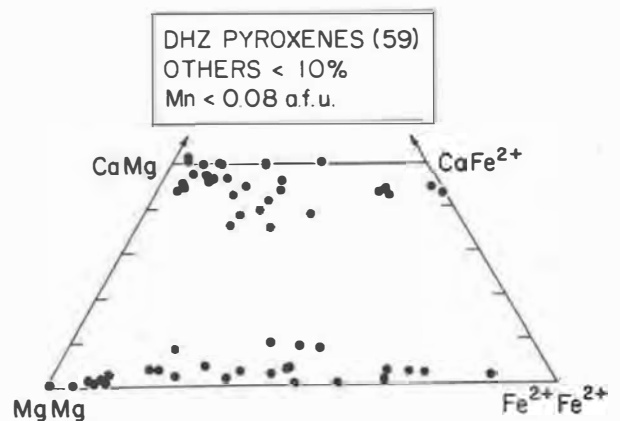


Fig. 26. Quadrilateral pyroxenes from Deer *et al.* (1978).

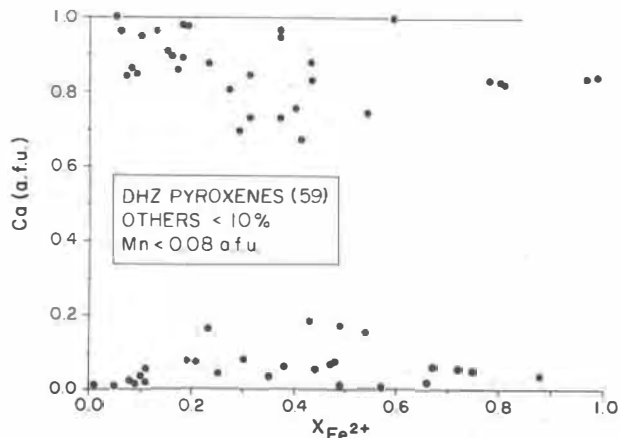


Fig. 27. Plot of Ca (atoms per formula unit, a.f.u.) vs. $X_{Fe^{2+}} = Fe^{2+}/(Fe^{2+}+Mg)$ (atomic) for quadrilateral pyroxenes from Deer *et al.* (1978).

NAT or NATAL fields, thus indicating that the $M^2Na^{M1}Ti$ or $M^2Na^{M1}Ti^{IV}Al$ substitutional couples are relatively uncommon. See Table A1 for a review of the terminology for Others.

Figure 30 shows that total Al varies between 0 and 1.0 a.f.u. for these pyroxenes. This limited range of Al content is interesting since the limit for total Al should be 2.0 a.f.u. (e.g., $CaAlSiAlO_6$). Figure 31 is a plot of ^{IV}Al vs. X_{Fe} . This diagram illustrates two points. First, because ^{IV}Al can vary between 0 and 1.0 (e.g., $CaAlSiAlO_6$) and is one of the two charge deficiency cations, the limit in this data set of ≈ 0.55 ^{IV}Al a.f.u. indicates that the maximum Others substitution component associated with ^{IV}Al is 55%. Second, it is

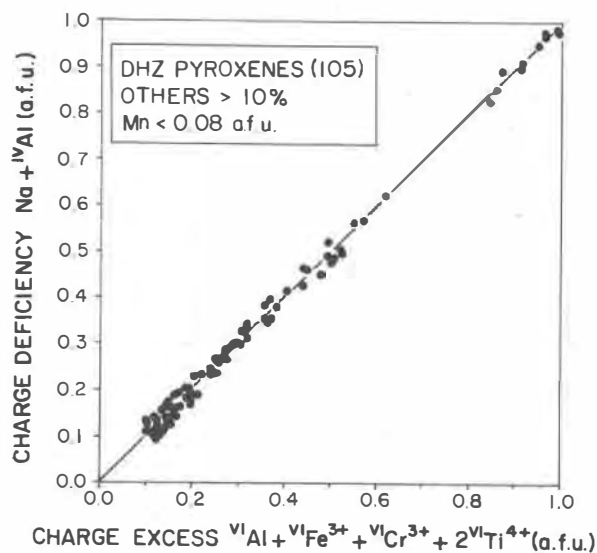


Fig. 28. Plot of charge deficiencies vs. charge excesses relative to quadrilateral pyroxenes. See text of paper for discussion. Analyses from Deer *et al.* (1978).

apparent that, in general, higher ^{IV}Al is associated with more Mg-rich pyroxenes.

The other charge deficiency cation, Na, is plotted against X_{Fe} in Figure 32. There are essentially two groups of pyroxenes based on the amount of Na in M2. Acmite and jadeite have Na between 1.0 and 0.8 a.f.u., whereas omphacite, aegirine-augite, and augite have Na < 0.55 a.f.u. This gap in Na content in the pyroxenes examined is the cause of the gap in the Others content in Figure 28. Because there are pyroxenes with sodium contents in this range, the gap is an artifact of the data selection.

We now consider the charge excess cations, ^{VI}Al , $^{VI}Fe^{3+}$, and $^{VI}Ti^{4+}$, that are most important in naturally-occurring pyroxenes. Figure 33 illustrates the variation of ^{VI}Al with X_{Fe} . ^{VI}Al ranges from 0 to 1.0 a.f.u., and thus can account for up to 100% Others substitutions (e.g., jadeite $NaAlSi_2O_6$). Note that the highest ^{VI}Al contents are at low X_{Fe} . Figure 34 shows the variation of Fe^{3+} with X_{Fe} . Again, Fe^{3+} varies from 0 to 1.0 a.f.u. and can account for 100% Others (e.g., acmite $NaFe^{3+}Si_2O_6$). Here we see, as is expected, high Fe^{3+} at high X_{Fe} . The last charge excess cation we consider is Ti, which is plotted against X_{Fe} in Figure 35. Ti contents in this data set are lower than for either ^{VI}Al or $^{VI}Fe^{3+}$ and range from 0 to 0.18 a.f.u. Because each substitution of a Ti^{4+} for a R^{2+} cation in Quad produces a charge excess of 2+, the maximum Ti content reported here can account for $\sim 36\%$ Others.

In summary, for the pyroxenes considered in this limited data set and ignoring lithium or manganese pyroxenes, Na is responsible for the highest Others contents as jadeite and acmite components.

Consider further the nature of the Others substitutions in the Mg- Fe^{2+} pyroxenes and augites. Based on our calculations of the best name for Others for the 175 superior analyses (Table A3), we find that the most important substitutional couples for the Mg- Fe^{2+} pyroxenes are as follows: ^{VI}Al - ^{IV}Al (43%), $^{VI}Fe^{3+}$ - ^{IV}Al (33%), ^{VI}Ti - $2^{IV}Al$ (19%), and $M^2Na^{VI}Ti^{IV}Al$ (5%). Thus, the $^{VI}R^{3+}$ - ^{IV}Al couples (CATS) are dominant in 76% of the pyroxenes considered. These estimates are based on 42 analyses, labelled as Mg or Fe pyroxene in Table A3, that correspond to orthopyroxene and pigeonite in DHZ.

In Table A3 we classify ~ 95 pyroxenes as augites. The substitutional couples for the Others components are as follows: $^{VI}Fe^{3+}$ - ^{IV}Al (35%), ^{VI}Al - ^{IV}Al (34%), $M^2Na^{VI}Ti^{4+IV}Al$ (13%), ^{VI}Ti - $2^{IV}Al$ (8%), $M^2Na^{VI}Fe^{3+}$ (5%), $M^2Na^{VI}Al$ (4%), and $M^2Na^{VI}Cr^{3+}$ (1%). These results show, as for the Mg- Fe^{2+} pyrox-

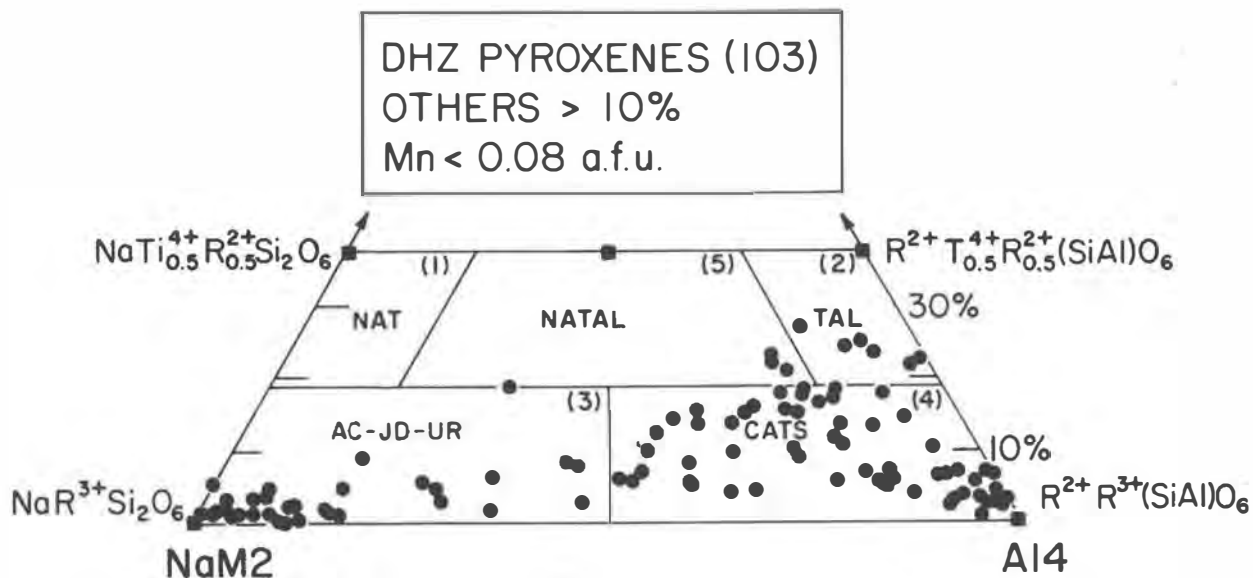


Fig. 29. Pyroxenes from Deer *et al.* (1978) plotted on the Others quadrilateral. See text of paper for discussion.

enes, that ${}^{\text{VI}}\text{Fe}^{3+}$ - ${}^{\text{IV}}\text{Al}$ and ${}^{\text{IV}}\text{Al}$ - ${}^{\text{VI}}\text{Al}$ are the dominant couples in the DHZ pyroxene data base. An important point is that Fe^{3+} is an extremely important cation in terrestrial pyroxenes and cannot be ignored. This poses a particular problem because at the present time most pyroxenes are analyzed with the microprobe, which cannot distinguish between Fe^{2+} and Fe^{3+} . Because of this problem, some workers have recalculated pyroxene analyses assuming that all Fe is present as Fe^{2+} . This is clearly a dangerous assumption and should be avoided in most cases. Indirect methods of estimating Fe^{3+} for microprobe data are available, one of which is referred to below.

Pyroxene chemistry in basaltic systems

As part of a NASA-sponsored program entitled "Basaltic Volcanism on the Terrestrial Planets," Papike and White (1979) conducted a synthesis of the pyroxene mineralogy of a planetary basalt suite. In that study, they examined approximately 1,200 high quality pyroxene microprobe analyses from the following basaltic suites: Archean, Columbia Plateau, deep sea, basaltic meteorite, Hawaiian, island arc, Keweenawan, lunar highland melt rock, lunar mare, and Rio Grande. Of special interest were those characteristics of pyroxene chemistry that reflect plan-

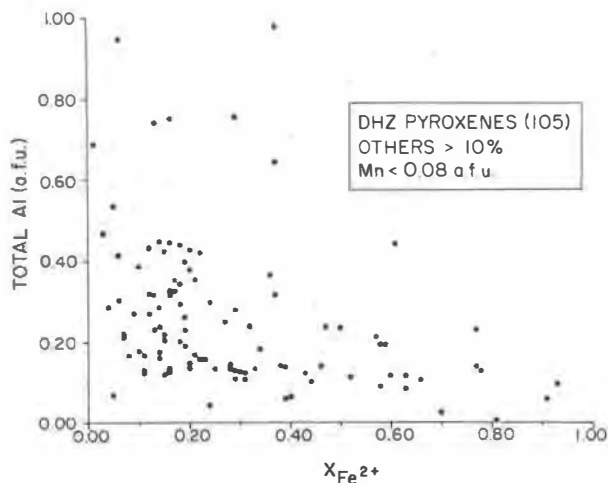


Fig. 30. Total Al (a.f.u.) vs. $X_{\text{Fe}^{2+}}$ for Deer *et al.* (1978) pyroxenes. See text of paper for discussion.

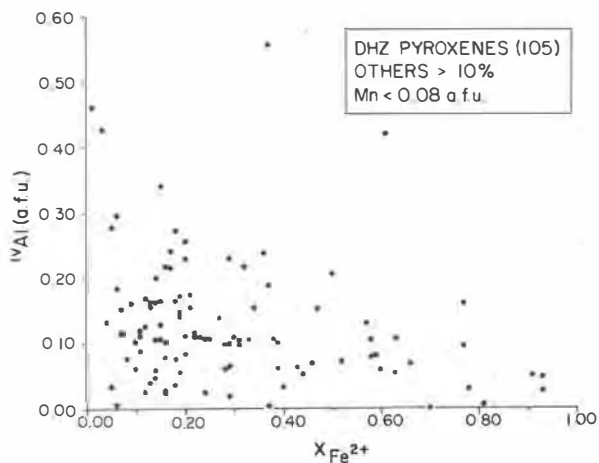


Fig. 31. Tetrahedral Al (a.f.u.) vs. $X_{\text{Fe}^{2+}}$ for Deer *et al.* (1978) pyroxenes. See text of paper for discussion.

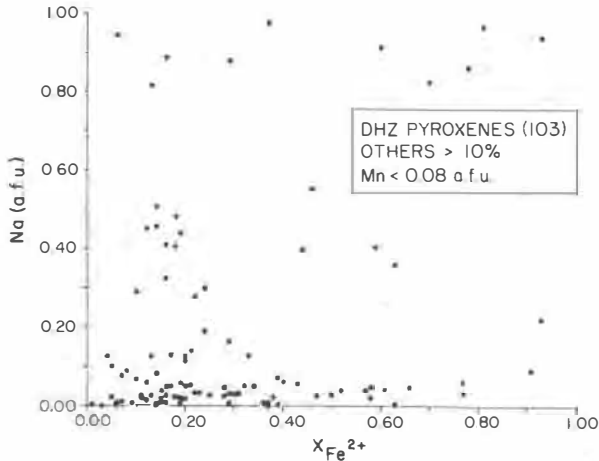


Fig. 32. Na (a.f.u.) vs. $X_{Fe^{2+}}$ for Deer *et al.* (1978) pyroxenes. See text of paper for discussion.

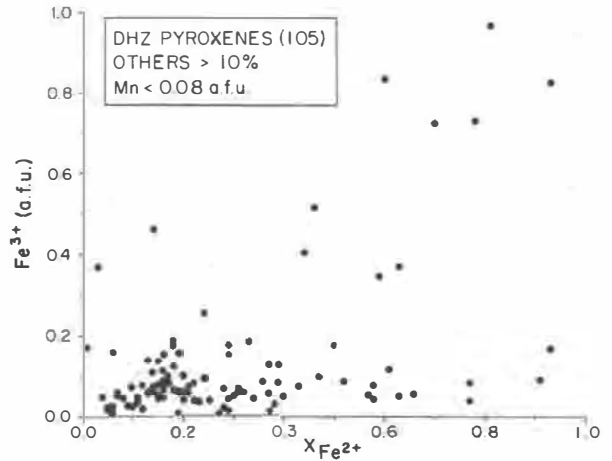


Fig. 34. Fe^{3+} (a.f.u.) vs. $X_{Fe^{2+}}$ for Deer *et al.* (1978) pyroxenes. See text of paper for discussion.

etary constraints on the host basalts from which the pyroxenes crystallized. The average composition for each of the pyroxene groups mentioned above is presented in Table 3.

The range of Fe_2O_3 values observed for these pyroxenes is considerable (Fe_2O_3 content was estimated by the method of Papike *et al.*, 1974). The reader is referred to Schweitzer *et al.* (1979) for documentation of ferric iron in terrestrial pyroxenes. Relatively high values of Fe_2O_3 are estimated for pyroxenes from deep sea (Schweitzer *et al.*, 1978, 1979), Hawaiian, island arc, and Rio Grande basalts. Pyroxenes from basaltic meteorites, lunar highland melt rocks, and mare basalts show essentially no Fe_2O_3 , and reflect the low oxygen fugacities that obtained during the extrusion of the parental basalts.

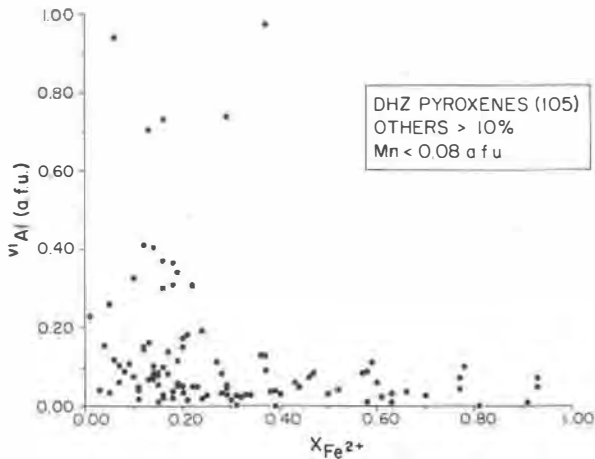


Fig. 33. Octahedral Al (a.f.u.) vs. $X_{Fe^{2+}}$ for Deer *et al.* (1978) pyroxenes. See text of paper for discussion.

The cation contents for twelve subgroups of the pyroxenes were treated statistically by a factor analysis program BMDP4M (Dixon, 1975). Results of the calculations are presented in Tables 4, A8, and A9. Table A8 illustrates the relative importance of the Others substitutional couples. The Archean pyroxenes have $^{VI}Al-^{IV}Al$ and $^{VI}Ti^{4+}-^{IV}Al$ as the two most important Others couples. These couples are consistent with the high Al concentrations reported for these pyroxenes. In pyroxenes from the Columbia Plateau suite, $^{VI}Fe^{3+}-^{IV}Al$ and $^{VI}Ti^{4+}-^{IV}Al$ are the two most important couples. Fe^{3+} is clearly important in these pyroxenes. In pyroxenes from the deep sea basalts, the same two couples are important, thus indicating similar oxygen fugacities obtained for the two rock suites. In the equilibrated eucrites, the significance of the correlation coefficients is equivocal because their values are low and the concentration of the Others components is also low. Nevertheless, $^{VI}Ti^{4+}-^{IV}Al$ and $^{VI}Al-^{IV}Al$ appear to be present. In

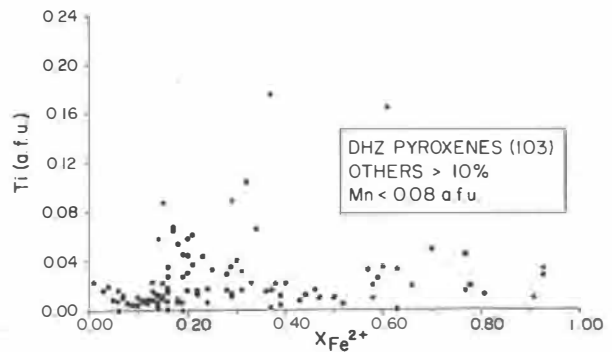


Fig. 35. Ti (a.f.u.) vs. $X_{Fe^{2+}}$ for Deer *et al.* (1978) pyroxenes. See text of paper for discussion.

Table 3. Mean values of pyroxene compositions

	Archean	Columbia Plateau	Deep Sea	Basaltic Meteorites	Hawaiian	Island Arc	Keweenawan	Lunar Highland	Lunar Mare	Rio Grande	(Grand Average)
SiO ₂	51.68	50.30	50.42	50.17	52.25	51.31	51.31	52.12	49.00	50.93	50.95
Al ₂ O ₃	3.92	2.00	3.01	0.75	2.82	2.83	1.79	1.98	2.55	2.68	2.43
FeO	9.60	12.51	10.60	27.107	8.45	9.54	13.21	15.62	22.15	10.30	13.91
Fe ₂ O ₃	0.70	0.62	1.61	0.00	1.02	1.79	1.02	0.00	=	1.43	1.17
MgO	16.75	13.05	14.89	13.36	21.05	16.02	15.37	21.18	13.06	15.73	16.05
MnO	0.24	0.27	0.28	0.763	0.14	0.19	0.34	0.24	0.36	0.29	0.31
TiO ₂	0.46	1.27	0.90	0.24	0.85	0.47	0.88	0.92	1.44	0.95	0.65
Cr ₂ O ₃	0.20	0.05	0.20	0.52	0.38	0.18	0.15	0.56	0.54	0.12	0.29
CaO	16.82	19.23	17.86	6.81	12.84	17.30	16.02	7.36	10.51	17.02	14.18
Na ₂ O	0.17	0.16	0.19	0.04	0.13	0.29	0.24	0.02	0.02	0.31	0.16
	100.54	99.46	99.96	99.85	99.93	99.92	100.33	100.00	99.63	99.76	100.10

Pasamonte, an unequilibrated eucrite that is virtually identical in bulk composition to the equilibrated eucrites, the most important substitutional couple is ${}^{\text{VI}}\text{Ti}^{4+}\text{-}{}^{\text{IV}}\text{Al}$. In the Shergotty meteorite, which has a different bulk chemistry (e.g., higher Na), the two most important Others couples are ${}^{\text{VI}}\text{Ti}^{4+}\text{-}{}^{\text{IV}}\text{Al}$ and $\text{Na-}{}^{\text{VI}}\text{Al}$ (jadeite). The latter couple reflects higher Na concentrations in the host basalt. Pyroxenes from the Hawaiian suite have an extremely high correlation coefficient (0.932) for the ${}^{\text{VI}}\text{Ti-}{}^{\text{IV}}\text{Al}$ couple, showing the dominance of this couple in these pyroxenes. The Na-containing couples $\text{Na-}{}^{\text{VI}}\text{Fe}^{3+}$ and $\text{Na-}{}^{\text{VI}}\text{Ti}^{4+}$ are also important. In the island arc suite, the dominant Others components are ${}^{\text{VI}}\text{Al-}{}^{\text{IV}}\text{Al}$ and ${}^{\text{VI}}\text{Fe}^{3+}\text{-}{}^{\text{IV}}\text{Al}$. In pyroxenes from the Keweenawan suite, the three most important couples are ${}^{\text{VI}}\text{Fe}^{3+}\text{-}{}^{\text{IV}}\text{Al}$, ${}^{\text{VI}}\text{Ti}^{4+}\text{-}{}^{\text{IV}}\text{Al}$, and $\text{Na-}{}^{\text{VI}}\text{Ti}^{4+}$. In the two lunar highlands and mare suites, ${}^{\text{VI}}\text{Ti-}{}^{\text{IV}}\text{Al}$ is the dominant Others couple. Lastly, pyroxenes from the Rio Grande basalts show ${}^{\text{VI}}\text{Fe}^{3+}\text{-}{}^{\text{IV}}\text{Al}$ as the dominant couple followed by ${}^{\text{VI}}\text{Ti}^{4+}\text{-}{}^{\text{IV}}\text{Al}$. Table 4 lists the two most important Others couples for each of these groups. With the data summarized in this manner, several things are apparent. First, the ${}^{\text{VI}}\text{Ti-}{}^{\text{IV}}\text{Al}$ couple is by far the most important Others couple: it ranks in the top two for all except the island arc suite. Second, Fe^{3+} is important in all of the terrestrial suites, with the possible exception of the Archean; it is usually present as the ${}^{\text{VI}}\text{Fe}^{3+}\text{-}{}^{\text{IV}}\text{Al}$ couple. This emphasizes the importance of f_{O_2} in pyroxene-liquid elemental partitioning. At the relatively high oxygen fugacities of terrestrial basalt petrogenesis, iron enters the pyroxene as both Fe^{3+} and Fe^{2+} whereas in lunar and most basaltic meteorite pyroxenes, iron is only present as Fe^{2+} .

Table A8 lists the Others-Quad cation correlations. These correlation coefficients enable us to ascertain if there is any preferential linking of the Others couples with a specific quadrilateral component. We will simplify the discussion by considering only

the two most important Others couples, ${}^{\text{VI}}\text{Ti}^{4+}\text{-}{}^{\text{IV}}\text{Al}$ and ${}^{\text{VI}}\text{Fe}^{3+}\text{-}{}^{\text{IV}}\text{Al}$. By examining the correlation coefficients in Table A8, we can decide which of the following pyroxene components are most important:



We can thus see whether these couples are correlated with augitic pyroxenes (high correlation with Ca), or whether they occur early in the crystallization sequence (high correlation with Mg) or late in the crystallization sequence (high correlation with Fe^{2+}). Such an analysis indicates that the Ti-Al couple is correlated with the Ca content of the pyroxene and with the degree of fractionation in Archean, Columbia Plateau, deep sea, Pasamonte, and Shergotty basalts, whereas it is essentially correlated only with Ca in Hawaiian, island arc, Keweenawan, lunar, and Rio Grande basalts. The Table A9 correlation coefficients show clearly that the ${}^{\text{VI}}\text{Fe}^{3+}\text{-}{}^{\text{IV}}\text{Al}$ couple enters the pyroxene structure as $\text{CaFe}^{3+}\text{SiAlO}_6$, and is largely concentrated in the augitic pyroxenes.

Table 4. Summary of the relative importance of the Others cation couples in pyroxenes

Group	First in Importance	Second in Importance
Archean	Ti-Al	Al-Al
Columbia Plateau	$\text{Fe}^{3+}\text{-Al}$	Ti-Al
Deep Sea	$\text{Fe}^{3+}\text{-Al}$	Ti-Al
Equilibrated Eucrites	($\text{Cr}^{3+}\text{-Al}$)?	Ti-Al
Pasamonte	Ti-Al	Cr-Al
Shergotty	Ti-Al	Na-Al
Hawaiian	Ti-Al	Na- Fe^{3+}
Island Arc	Al-Al	$\text{Fe}^{3+}\text{-Al}$
Keweenawan	$\text{Fe}^{3+}\text{-Al}$	Ti-Al
Lunar Highlands	Ti-Al	Na-Ti
Lunar Mare	Ti-Al	Al-Al
Rio Grande	$\text{Fe}^{3+}\text{-Al}$	Ti-Al

Microstructures

We include in our discussion of microstructures the anti-phase domains of pigeonite and omphacite and the various exsolution features that occur in both ortho- and clinopyroxenes. All the features can be observed and studied by transmission electron microscopy (TEM), but some are also visible under the polarizing microscope. Much of the discussion that follows is cursory in nature, and the interested reader is referred to *Electron Microscopy in Mineralogy* (Wenk, 1976) for additional details on TEM studies.

Anti-phase domains

The domain structure in pigeonite forms during the transition from the high-temperature $C2/c$ structure to the low-temperature $P2_1/c$ structure. The domains were predicted by Morimoto and Tokonami (1969a), who observed diffuse "b"-type reflections ($h + k = \text{odd integer}$) on precession photographs. These "b" reflections had disc-like shapes within the a^*b^* plane, which is perpendicular to the c direction; thus, they reasoned that the domains must be elongated parallel to c . Subsequent electron microscopy studies (e.g., Champness and Lorimer, 1971) confirmed the presence of such domains.

Adjacent domains in pigeonite are in antiphase relationship with a $(a + b)/2$ translation. They are commonly elongated parallel to c and range in diameter from about 200–500Å in pigeonites from volcanic rocks to more than 1000Å in pigeonites from intrusive rocks (Morimoto, 1974). Their formation is largely a consequence of the differences in the tetrahedral chains of the high and low structures. In the high structure there is only one type of tetrahedral chain, whereas in the low structure there are two types. During cooling through the transition point, half of the $C2/c$ chains become A chains and half become B chains in the lower-temperature $P2_1/c$ structure. Presumably, near the transition point, nuclei of the low structure form throughout the high structure. As these nuclei grow and coalesce, those with different orientations of A and B chains form different domains that are out of phase by $(a+b)/2$ (Fig. 36). The translational mistake at the antiphase boundaries (APB's) does not significantly perturb the basic pyroxene structure, but it does produce bands with a C-centered lattice along the domain boundaries. Largely for this reason, several workers (Morimoto and Tokonami, 1969a; Clark *et al.*, 1971) postulated that these APB's are enriched in Ca. Lally *et al.* (1975) found no evidence for Ca-enrichment in a TEM study of lunar pyroxenes; however, Carpenter

(1978a) concluded that certain APB's in pigeonites of dolerites are Ca-enriched.

There have been numerous attempts (e.g., Nord *et al.*, 1973) to correlate the size of antiphase domains (APD's) in pigeonite with relative cooling rates of the rocks in which they occur. If we assume homogeneous nucleation during cooling, the theoretical effect of decreasing the cooling rate through the transition produces larger APD's because fewer nuclei form and there is a longer time in which to coarsen. However, there are numerous complications and at present the technique is of limited use. Heterogeneous nucleation, either on a dislocation or on pre-existing exsolution lamellae, produces large APD's even with more rapid rates of cooling (e.g., Lally *et al.*, 1975). Carpenter (1979) noted that APD size may also be composition-dependent because the $C2/c \rightleftharpoons P2_1/c$ transformation varies with composition. In addition, he reported that the domain size in pigeonite quenched from above the transition temperature can be as large as 2600Å, and apparently is independent of annealing time and temperature.

Antiphase domains 100–3000Å wide and related by the vector $(a+b)/2$ are also present in omphacite (Phakey and Ghose, 1973; Champness, 1973). The origin of the domains is attributed to cation ordering, which produces a transformation from a C-centered to a P lattice. However, Heuer and Nord (1976) noted that the low temperature environment in which the omphacites formed may preclude such a diffusion-controlled transition. A detailed discussion of the ordering and exsolution in omphacites is given in Carpenter (1978b, 1980).

Exsolution features

Exsolution lamellae form in pyroxenes of many igneous and metamorphic rocks by unmixing during cooling. Commonly-reported host-lamellae relationships (after Hess, 1941 and Poldervaart and Hess, 1951) include the following:

Exsolution involving a $C2/c$ monoclinic host:

- augite with (100) hypersthene lamellae
- augite with (001) pigeonite lamellae
- augite with both (100) hypersthene and (001) pigeonite lamellae

Exsolution involving a $Pbca$ orthorhombic host:

- hypersthene with (100) augite lamellae (orthopyroxene of the Bushveld type)

Exsolution involving a $P2_1/c$ monoclinic host:

- pigeonite with (001) and occasionally (100) augite lamellae



Fig. 36. Schematic diagrams of the pigeonite structure projected down [001] (after Morimoto, 1974). (a) C-centered lattice of high $C2/c$ pigeonite. A and V represent symmetrically identical chains. (b) Primitive lattice of low $P2_1/c$ pigeonite. The A chains are represented by A and V and the B chains by U and N. (c) Domain structure of low pigeonite. Note shift of $(a + b)/2$ along domain boundaries.

Host-lamellae associations other than the above are less common. Yamaguchi and Tomita (1970) reported monoclinic enstatite exsolved parallel to (100) in terrestrial diopsides. Morimoto and Tokonami (1969b) described a pigeonite from the Moore County meteorite that contained hypersthene lamellae and two sets of augite lamellae exsolved parallel to (100) and (001). They calculated a strain energy of 0.02 kcal/mole for the (001) exsolution lamellae compared to 0.04 kcal/mole for (100) lamellae. These values indicate that the former orientation should be more common, as is observed. They also reported that the strain energies for augite exsolved on (010) or (110) of pigeonite is approximately an order of magnitude greater, and thus precipitation in such orientations appears less likely but not impossible. Brown (1957) reported the presence of (010) blebs in inverted pigeonites.

The term "inverted pigeonite" (orthopyroxene of the Stillwater type) refers to a hypersthene grain that contains (100) and ($h0l$) augite lamellae. Presumably the grain crystallized as a $C/2c$ pigeonite above the clino-ortho boundary and with cooling exsolved augite parallel to (001). As the crystal cooled through the clino-ortho boundary, the host pigeonite inverted to hypersthene, concomitantly changing the indices of the (001) lamellae to ($h0l$). Exsolution of augite continued, but now parallel to the (100) plane. The textures of rocks that contain inverted pigeonites are frequently more complex than described above. In the Biwabik and Gunflint Iron Formations, individual inverted pigeonite grains (\equiv hypersthene) contain multiple sets of randomly oriented augite exsolution lamellae (Bonnichsen, 1969; Simmons *et al.*, 1974). Each hypersthene grain is interpreted to have formed from numerous precursor grains of pigeonite, each with (001) augite lamellae. At the clino-ortho transition, one nucleus of ortho formed and a single crystallization front swept through adjacent pigeonite crystals, ignoring grain boundaries. Subsequent ex-

solution of augite parallel to (100) in this composite grain overprints the randomly-oriented ($h0l$) lamellae.

The general orientation of exsolution lamellae is influenced by the crystal systems of the host and the lamellae. Exsolution of a monoclinic phase from a monoclinic host usually, but not always, occurs near (001) of the host, whereas exsolution involving monoclinic and orthorhombic phases usually occurs near (100) planes. In detail, these lamellae may not be oriented exactly parallel to specific rational lattice planes of the host. P. Robinson *et al.* (1971) and Jaffe *et al.* (1975) showed that the exact orientation of augite or pigeonite exsolution lamellae in a pigeonite or augite host was such that the dimensional fit of the lattices at the start of exsolution was optimized. This best fit, which minimizes strain energy, was achieved by slight relative rotations of the two pyroxene lattices. Thus, in some clinopyroxenes the "001" and "100" lamellae are actually oriented on irrational planes near (001) and (100). The angles between the boundaries of these lamellae and c axis of the host pyroxene varies according to the Fe-Mg ratio, with the deviation being largest in magnesian samples (Jaffe *et al.*, 1975). Robinson *et al.* (1977) attributed variations of 18° in the angle of "001" lamellae and 32° in the angle of the "100" lamellae to differences in unit cell parameters at the various temperatures at which the lamellae formed. They concluded that temperatures of exsolution in monoclinic pyroxenes could be estimated either from the orientation of the exsolution boundaries or from the differential changes in unit cell parameters for the host and lamellar phases during cooling. Application of these geothermometers to four different sets of pigeonite lamellae (one "100" and three "001") in augite from the Bushveld Complex produced a reasonable sequence of exsolution temperatures.

The most effective means of studying the mechanisms of exsolution and the various types of sub-mi-

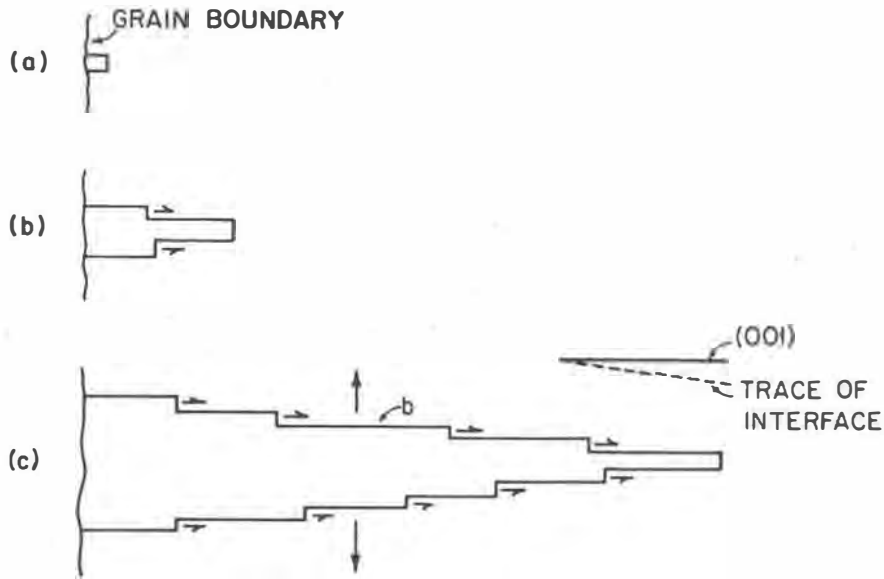


Fig. 37. Model proposed to explain the growth of heterogeneously nucleated (001) pigeonite lamellae in augite (after Copley *et al.*, 1974). The three figures schematically show the growth sequence with time.

croscopic structures in pyroxenes is transmission electron microscopy. Copley *et al.* (1974) and Champness and Lorimer (1973) described in detail the development and growth of exsolution lamellae, and the sequence of growth of a wedge-shaped (001) pigeonite lamellae in augite is shown schematically in Figure 37. Lengthening of the lamellae occurs by migration of the ledges parallel to (001) whereas thickening occurs by propagation of ledges across the (001) faces. Champness and Lorimer (1973, 1974) described the following three types of (100) precipitates in primary orthopyroxenes from the Bushveld and Stillwater Complex: (1) coarse, optically visible, semi-coherent augite lamellae that nucleated hetero-

geneously and have stepped interfaces with the host crystal, (2) fine, homogeneously distributed coherent disc-shaped Guinier–Preston (G.P.) zones about 18 Å thick, and (3) a heterogeneously nucleated coherent precipitate with cell parameters close to those of clinoenstatite or pigeonite. All the precipitates are richer in Ca than are the host orthopyroxenes. The two latter precipitates are thought to be metastable and to have formed at low temperatures after the precipitation of the equilibrium (100) augite (Champness and Lorimer, 1974). The G.P. zones are considered to be the result of pre-precipitate reactions occurring in supersaturated solid solutions. In metal alloys the term is applied to metastable precipitates having a structure similar to but a composition different from the host phase. Adjacent to each augite lamellae, they also noted precipitate-free zones (P.F.Z.) that apparently formed in areas which lacked sufficient Ca even for nucleation of G.P. zones. Carpenter (1978a) studied by TEM the development of microstructures in slowly cooled pigeonite from a coarse-grained dolerite. He deduced that the following sequence of events occurred during cooling: (1) heterogeneous nucleation of large (001) lamellae of augite, (2) formation of APD's, and (3) heterogeneous nucleation of fine (001) augite lamellae at Ca-enriched APB's. In some crystals events (1) and (2) were reversed, indicating that both occurred in a similar temperature range.

The two mechanisms by which exsolution in pyroxenes proceeds are: (1) spinodal decomposition

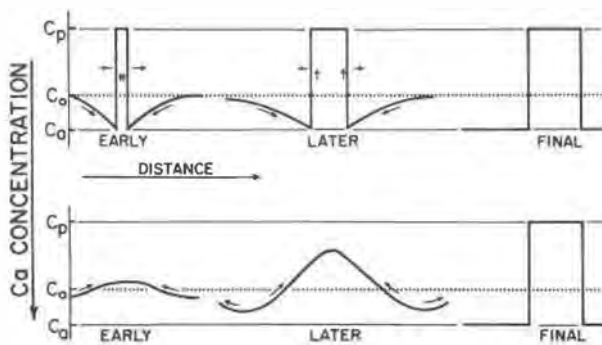


Fig. 38. Schematic evolution of Ca concentration profiles for nucleation and growth mechanism vs. the spinodal mechanism (after Cahn, 1968). C_0 refers to Ca concentration in the original crystal, C_a to the relative concentrations in augite, and C_p to the relative concentration in pigeonite.

and (2) nucleation and growth. Nucleation can be homogeneous or heterogeneous. The latter involves formation of nuclei on pre-existing defects such as stacking faults, dislocations, and low or high-energy boundaries. Spinodal decomposition² does not require a nucleation event; it is simply a diffusional clustering mechanism. Yund and McCallister (1970) described spinodal decomposition as proceeding "from a compositional perturbation small in degree but large in extent. The perturbation grows and a new phase gradually emerges which is structurally coherent with its surroundings across a diffuse interface. Thus, unlike classical nucleation, there is no clear stage at which the second phase appears." The end result at equilibrium of both mechanisms is similar (Fig. 38), but the concentration profiles in the initial stages are different. Lamellae that formed by homogeneous nucleation and growth are commonly indistinguishable from those formed by spinodal decomposition followed by coarsening. McCallister and Yund (1975), in a TEM study of pyroxene exsolution along the Di-En join, attributed irregular, almost spindly lamellae to rapid exsolution that occurred by spinodal decomposition and straight and continuous lamellae to the mechanism of nucleation and growth. Nord *et al.* (1976) emphasized that before spinodal decomposition is rigorously suggested as a unmixing mechanism for any pyroxene that (1) diffuse matrix-precipitate interfaces should be present and (2) that $\Delta\beta$ ($= \beta$ of pigeonite - β of augite sharing a common 001 plane) should have a value somewhere near the equilibrium value of 2.6° (Papike *et al.*, 1971).

The importance of the mechanism involved in exsolution or phase separation has implications with respect to the composition of the coexisting phases and hence for the shape and position of a solvus. Exsolution lamellae formed by precipitation and growth usually have the equilibrium composition whereas lamellae formed by spinodal decomposition may exhibit a range of compositions. The latter would only achieve the equilibrium compositional state after coarsening.

Acknowledgments

We are grateful to L. W. Finger, F. C. Hawthorne, R. M. Hazen, and P. Robinson for detailed and constructive reviews of this paper. We thank Louise Levien and C. T. Prewitt for allowing

us to use some of their high-pressure data prior to publication. We are also indebted to the following individuals who helped substantially in the technical aspects of preparing this paper: Lois Koh for drafting the figures, Neal White for performing numerous computer calculations, Robin Spencer for typing the entire manuscript and helping to compile and check the tables of data and references, and Pauline Papike for proof-reading and compiling the manuscript. This work was partially supported by NASA grant NSG9044.

References

- Appleman, D. E., Boyd, Jr., F. R., Brown, G. M., Ernst, W. G., Gibbs, G. V., and Smith, J. V. (1966) AGI Short Course on Chain Silicates. American Geological Institute, Washington, D.C.
- Baur, W. H. (1971) The prediction of bond length variations in silicon-oxygen bonds. *American Mineralogist*, 56, 1573-1599.
- Bence, A. E. and Papike, J. J. (1972) Pyroxenes as recorders of lunar basalt petrogenesis: chemical trends due to crystal-liquid interaction. *Proceedings of the 3rd Lunar Science Conference*, 1, 431-469.
- Bonnichsen, B. (1969) Metamorphic pyroxenes and amphiboles in the Biwabik Iron Formation, Dunka River area, Minnesota. *Mineralogical Society of America Special Paper*, 2, 217-239.
- Brovkin, A. A., Novoselov, Yu. M., and Kitsul, V. I. (1975) Distribution of aluminum in the crystal structure of high-alumina hypersthene. *Doklady Akademiia Nauk USSR*, 223, 148-150.
- Brown, G. E. and Gibbs, G. V. (1969) Oxygen coordination and the Si-O bond. *American Mineralogist*, 54, 1528-1539.
- Brown, G. E. and Gibbs, G. V. (1970) Stereochemistry and ordering in the tetrahedral portion of silicates. *American Mineralogist*, 55, 1587-1607.
- Brown, G. E., Gibbs, G. V., and Ribbe, P. H. (1969) The nature and variation in length of the Si-O and Al-O bonds in framework silicates. *American Mineralogist*, 54, 1044-1061.
- Brown, G. E., Prewitt, C. T., Papike, J. J., and Sueno, S. (1972) A comparison of the structures of low and high pigeonite. *Journal of Geophysical Research*, 77, 5778-5789.
- Brown, G. M. (1957) Pyroxenes from the early and middle stages of fractionation of the Skaergaard intrusion, East Greenland. *Mineralogical Magazine*, 31, 511-543.
- Brown, G. M. (1967) Mineralogy of basaltic rocks. In H. H. Hess and A. Poldervaart, Eds., *Basalts*, 1, p. 103-162. Wiley, New York.
- Brown, G. M. (1972) Pigeonitic pyroxenes: a review. *Geological Society of America Memoir*, 132, 523-534.
- Brown, I. D. and Shannon, R. D. (1973) Empirical bond-strength-bond-length curves for oxides. *Acta Crystallographica*, A29, 266-282.
- Brown, W. L. (1972) La symétrie et les solutions solides des clinopyroxènes. *Bulletin de Société française de Minéralogie et de Cristallographie*, 95, 574-582.
- Burnham, C. W. (1965) Ferrosilite. *Carnegie Institution of Washington Year Book*, 64, 202-204.
- Burnham, C. W. (1966) Ferrosilite. *Carnegie Institution of Washington Year Book*, 65, 285-290.
- Burnham, C. W., Clark, J. R., Papike, J. J., and Prewitt, C. T. (1967) A proposed crystallographic nomenclature for clinopyroxene structures. *Zeitschrift für Kristallographie*, 125, 1-6.
- Burnham, C. W., Ohashi, Y., Hafner, S. S., and Virgo, D. (1971). Cation distribution and atomic thermal vibrations in an iron-rich orthopyroxene. *American Mineralogist*, 56, 850-876.

² The term spinodal means the limit beyond which a homogeneous phase is no longer stable. It was first introduced in 1877 by Gibbs, who referred to it as the limit of metastability (Gibbs, 1961). It is, in simple terms, the boundary between metastable and unstable.

- Burns, R. G. (1970) Mineralogical Applications of Crystal Field Theory. Cambridge University Press, Cambridge, England.
- Buseck, P. R. and Iijima, S. (1975) High resolution electron microscopy of enstatite. II: geological application. *American Mineralogist*, 60, 771-784.
- Cahn, J. W. (1968) Spinodal decomposition. *Transactions of the Metallurgical Society of AIME*, 242, 166-180.
- Cameron, M., Sueno, S., Prewitt, C. T., and Papike, J. J. (1973) High-temperature crystal chemistry of acmite, diopside, hedenbergite, jadeite, spodumene and ureyite. *American Mineralogist*, 58, 594-618.
- Carpenter, M. A. (1978a) Nucleation of augite at antiphase boundaries in pigeonite. *Physics and Chemistry of Minerals*, 2, 237-251.
- Carpenter, M. A. (1978b) Kinetic control of ordering and exsolution in omphacite. *Contributions to Mineralogy and Petrology*, 67, 17-24.
- Carpenter, M. A. (1979) Experimental coarsening of antiphase domains in a silicate mineral. *Science*, 206, 681-683.
- Carpenter, M. A. (1980) Mechanisms of exsolution in sodic pyroxenes. *Contributions to Mineralogy and Petrology*, 71, 289-300.
- Champness, P. E. (1973) Speculation on an order-disorder transformation in omphacite. *American Mineralogist*, 58, 540-542.
- Champness, P. E. and Lorimer, G. W. (1971) An electron microscopic study of a lunar pyroxene. *Contributions to Mineralogy and Petrology*, 33, 171-183.
- Champness, P. E. and Lorimer, G. W. (1973) Precipitation (exsolution) in an orthopyroxene. *Journal of Materials Science*, 8, 467-474.
- Champness, P. E. and Lorimer, G. W. (1974) A direct lattice-resolution study of precipitation (exsolution) in orthopyroxene. *Philosophical Magazine*, 30, 357-365.
- Clark, J. R. and Papike, J. J. (1968) Crystal-chemical characterization of omphacites. *American Mineralogist*, 53, 840-868.
- Clark, J. R., Appleman, D. E., and Papike, J. J. (1968) Bonding in eight ordered clinopyroxenes isostructural with diopside. *Contributions to Mineralogy and Petrology*, 20, 81-85.
- Clark, J. R., Appleman, D. E., and Papike, J. J. (1969) Crystal-chemical characterization of clinopyroxenes based on eight new structure refinements. *Mineralogical Society of America Special Paper*, 2, 31-50.
- Clark, J. R., Ross, M., and Appleman, D. E. (1971) Crystal chemistry of a lunar pigeonite. *American Mineralogist*, 56, 888-908.
- Copley, P. A., Champness, P. E., and Lorimer, G. W. (1974) Electron petrography of exsolution textures in an iron-rich clinopyroxene. *Journal of Petrology*, 15, 41-57.
- Curtis, L., Gittins, J., Kocman, V., Rucklidge, J. C., Hawthorne, F. C., and Ferguson, R. B. (1975) Two crystal structure refinements of a $P2/n$ titanian ferro-omphacite. *Canadian Mineralogist*, 13, 62-67.
- Deer, W. A., Howie, R. A., and Zussman, J. (1978) *Rock-Forming Minerals*, Vol. 2A, second edition, Single-Chain Silicates. Wiley, New York.
- Dixon, W. J. (Ed.) (1975) *BMDP Biomedical Computer Programs*. University of California Press, Berkeley, California.
- Dodd, R. T., Grover, J. E., and Brown, G. E. (1975) Pyroxenes in the Shaw (L-7) chondrite. *Geochimica et Cosmochimica Acta*, 39, 1585-1594.
- Dowty, E. and Clark, J. R. (1973) Crystal structure refinement and optical properties of a Ti^{3+} fassaite from the Allende meteorite. *American Mineralogist*, 58, 230-242.
- Ferguson, R. B. (1974) A cation-anion distance-dependent method for evaluating valence-bond distributions in ionic structures and results for some olivines and pyroxenes. *Acta Crystallographica*, B30, 2527-2539.
- Finger, L. W. and Ohashi, Y. (1976) The thermal expansion of diopside to 800°C and a refinement of the crystal structure at 700°C. *American Mineralogist*, 61, 303-310.
- Freed, R. L. and Peacor, D. R. (1967) Refinement of the crystal structure of johannsenite. *American Mineralogist*, 52, 709-720.
- Ganguly, J. and Ghose, S. (1979) Aluminous orthopyroxene: order-disorder, thermodynamic properties, and petrologic implications. *Contributions to Mineralogy and Petrology*, 69, 375-385.
- Gasparik, T. and Lindsley, D. H. (1980) Experimental study of pyroxenes in the system $CaMgSi_2O_6$ - $CaAl_2SiO_6$ - $Ca_{0.5}AlSi_2O_6$. *EOS*, 61, 402-403.
- Ghose, S. (1965) Mg^{2+} - Fe^{2+} order in an orthopyroxene, $Mg_{0.93}Fe_{1.07}Si_2O_6$. *Zeitschrift für Kristallographie*, 122, 81-99.
- Ghose, S. and Wan, C. (1973) Luna 20 pyroxenes: evidence for a complex thermal history. *Proceedings of the 4th Lunar Science Conference*, 1, 901-907.
- Ghose, S., Wan, C., and Okamura, F. P. (1975) Site preference and crystal chemistry of transition metal ions in pyroxenes and olivines. (abstr.) *Acta Crystallographica*, A31, S76.
- Gibbs, G. V., Hamil, M. M., Louisnathan, S. J., Bartell, L. S., and Yow, H. (1972) Correlations between Si-O bond length, Si-O-Si angle and bond overlap populations calculated using extended Hückel molecular orbital theory. *American Mineralogist*, 57, 1578-1613.
- Gibbs, J. W. (1961) *The Scientific Papers of J. Willard Gibbs*, 1. Dover Publications, New York.
- Grove, T. L. and Burnham, C. W. (1974) Al-Si disorder in calcium Tschermak's pyroxene, $CaAl_2SiO_6$. *EOS*, 55, 1202.
- Güven, N. (1969) Nature of the coordination polyhedra around M2 cations in pigeonite. *Contributions to Mineralogy and Petrology*, 24, 268-274.
- Hawthorne, F. C. and Grundy, H. D. (1973) Refinement of the crystal structure of $NaScSi_2O_6$. *Acta Crystallographica*, B29, 2615-2616.
- Hawthorne, F. C. and Grundy, H. D. (1974) Refinement of the crystal structure of $NaInSi_2O_6$. *Acta Crystallographica*, B30, 1882-1884.
- Hawthorne, F. C. and Grundy, H. D. (1977) Refinement of the crystal structure of $LiScSi_2O_6$ and structural variations in alkali pyroxenes. *Canadian Mineralogist*, 15, 50-58.
- Hawthorne, F. C. and Ito, J. (1977) Synthesis and crystal-structure refinement of transition-metal orthopyroxenes I: orthoenstatite and (Mg, Mn, Co) orthopyroxene. *Canadian Mineralogist*, 15, 321-338.
- Hawthorne, F. C. and Ito, J. (1978) Refinement of the crystal structures of $(Mg_{0.77}Co_{0.22})SiO_3$ and $(Mg_{0.925}Mn_{0.075})SiO_3$. *Acta Crystallographica*, B34, 891-893.
- Hazen, R. M. (1977) Temperature, pressure and composition: structurally analogous variables. *Physics and Chemistry of Minerals*, 1, 83-94.
- Hazen, R. M. and Finger, L. W. (1977a) Crystal structure and compositional variation of Angra dos Reis fassaite. *Earth and Planetary Science Letters*, 35, 357-362.
- Hazen, R. M. and Finger, L. W. (1977b) Compressibility and crystal structure of Angra dos Reis fassaite to 52 kbar. *Carnegie Institution of Washington Year Book*, 76, 512-515.
- Hazen, R. M. and Prewitt, C. T. (1977) Effects of temperature and

- pressure on interatomic distances in oxygen-based minerals. *American Mineralogist*, 62, 309–315.
- Hess, H. H. (1941) Pyroxenes of common mafic magmas. *American Mineralogist*, 26, 515–535, 573–594.
- Heuer, A. H. and Nord, Jr., G. L. (1976) Polymorphic phase transitions in minerals. In H.-R. Wenk *et al.*, Eds., *Electron Microscopy in Mineralogy*, p. 274–303. Springer-Verlag, Berlin.
- Hill, R. J. and Gibbs, G. V. (1979) Variation in $d(T-O)$, $d(T \cdots T)$ and ΔTOT in silica and silicate minerals, phosphates and aluminates. *Acta Crystallographica*, B35, 25–30.
- Huckenholz, H. G., Schairer, J. F., and Yoder, Jr., H. S. (1969) Synthesis and stability of ferri-diopside. *Mineralogical Society of America Special Paper*, 2, 163–177.
- Iijima, S. and Buseck, P. R. (1975) High resolution electron microscopy of enstatite. I: Twinning, polymorphism, and polytypism. *American Mineralogist*, 60, 758–770.
- Jaffe, H. W., Robinson, P., Tracy, R. J., and Ross, M. (1975) Orientation of pigeonite exsolution lamellae in metamorphic augite: correlation with composition and calculated optimal phase boundaries. *American Mineralogist*, 60, 9–28.
- Kosoi, A. L., Malkova, L. A., and Frank-Kamenetskii, V. A. (1974) Crystal-chemical characteristics of rhombic pyroxenes. *Kristallografiya*, 19, 282–288 (transl. *Soviet Physics and Crystallography*, 19, 171–174, 1974).
- Kushiro, I. (1969) Clinopyroxene solid solutions formed by reactions between diopside and plagioclase at high pressures. *Mineralogical Society of America Special Paper*, 2, 179–191.
- Lally, J. S., Heuer, A. H., Nord, Jr., G. L., and Christie, J. M. (1975) Subsolidus reactions in lunar pyroxenes: an electron petrographic study. *Contributions to Mineralogy and Petrology*, 51, 263–281.
- Law, A. D. and Whittaker, E. J. W. (1980) Rotated and extended model structures in amphiboles and pyroxenes. *Mineralogical Magazine*, 43, 565–574.
- Levien, L. and Prewitt, C. T. (1981) High-pressure structural study of diopside. *American Mineralogist*, in press.
- Louisnathan, S. J. and Gibbs, G. V. (1972a) The effect of tetrahedral angles on Si–O bond overlap populations for isolated tetrahedra. *American Mineralogist*, 57, 1614–1642.
- Louisnathan, S. J. and Gibbs, G. V. (1972b) Variation of Si–O distances in olivines, soda melilite and sodium metasilicate as predicted by semi-empirical molecular orbital calculations. *American Mineralogist*, 57, 1643–1663.
- Matsumoto, T. (1974) Possible structure types derived from *Pbca*-orthopyroxene. *Mineralogical Magazine*, 7, 374–383.
- Matsumoto, T., Tokonami, M., and Morimoto, N. (1975) The crystal structure of omphacite. *American Mineralogist*, 60, 634–641.
- McCallister, R. H. and Yund, R. A. (1975) Kinetics and microstructure of pyroxene exsolution. *Carnegie Institution of Washington Year Book*, 74, 433–436.
- McCallister, R. H., Finger, L. W., and Ohashi, Y. (1974) Refinement of the crystal structure of a subcalcic diopside. *Carnegie Institution of Washington Year Book*, 73, 518–522.
- McCallister, R. H., Finger, L. W., and Ohashi, Y. (1976) Intracrystalline Fe^{2+} –Mg equilibria in three natural Ca-rich clinopyroxenes. *American Mineralogist*, 61, 671–676.
- McDonald, W. S. and Cruickshank, D. W. J. (1967) A reinvestigation of the structure of sodium metasilicate, Na_2SiO_3 . *Acta Crystallographica*, 22, 37–43.
- Miyamoto, M., Takeda, H., and Takano, Y. (1975) Crystallographic studies of a bronzite in the Johnstown achondrite. *Fortschritte der Mineralogie*, 52, 389–397.
- Morgan, B. A. (1967) Geology of the Valencia Area, Carabobo, Venezuela. Ph.D. Thesis, Princeton University, Princeton, New Jersey.
- Morimoto, N. (1974) Crystal structure and fine texture of pyroxenes. *Fortschritte der Mineralogie*, 52, 52–80.
- Morimoto, N. and Güven, N. (1970) Refinement of the crystal structure of pigeonite. *American Mineralogist*, 55, 1195–1209.
- Morimoto, N. and Koto, K. (1969) The crystal structure of orthoenstatite. *Zeitschrift für Kristallographie*, 129, 65–83.
- Morimoto, N. and Tokonami, M. (1969a) Domain structure of pigeonite and clinoenstatite. *American Mineralogist*, 54, 725–740.
- Morimoto, N. and Tokonami, M. (1969b) Oriented exsolution of augite in pigeonite. *American Mineralogist*, 54, 1101–1117.
- Morimoto, N., Appleman, D. E., and Evans, Jr., H. T. (1960) The crystal structures of clinoenstatite and pigeonite. *Zeitschrift für Kristallographie*, 114, 120–147.
- Morimoto, N., Nakajima, Y., Syono, Y., Akimoto, S., and Matsui, Y. (1975) Crystal structures of pyroxene-type $ZnSiO_3$ and $ZnMgSi_2O_6$. *Acta Crystallographica*, B31, 1041–1049.
- Mueller, R. F. (1962) Energetics of certain silicate solid solutions. *Geochimica et Cosmochimica Acta*, 26, 581–598.
- Mueller, R. F. (1969) Kinetics and thermodynamics of intracrystalline distributions. *Mineralogical Society of America Special Paper*, 2, 83–93.
- Nord, Jr., G. L., Heuer, A. H., and Lally, J. S. (1976) Pigeonite exsolution from augite. In H.-R. Wenk *et al.*, Eds., *Electron Microscopy in Mineralogy*, p. 220–227. Springer-Verlag, Berlin.
- Nord, Jr., G. L., Lally, J. S., Heuer, A. H., Christie, J. M., Radcliffe, S. V., Griggs, D. T., and Fisher, R. M. (1973) Petrologic study of igneous and metaigneous rocks from Apollo 15 and 16 using high voltage transmission electron microscopy. *Proceedings of the Fourth Lunar Science Conference*, 1, 953–970.
- Ohashi, Y. and Burnham, C. W. (1973) Clinopyroxene lattice deformations: the roles of chemical substitution and temperature. *American Mineralogist*, 58, 843–849.
- Ohashi, Y. and Finger, L. W. (1974a) Symmetry reduction and twinning relationships in clinopyroxene and orthopyroxenes. *Carnegie Institution of Washington Year Book*, 73, 531–535.
- Ohashi, Y. and Finger, L. W. (1974b) A lunar pigeonite: crystal structure of primitive-cell domains. *Carnegie Institution of Washington Year Book*, 73, 525–531.
- Ohashi, Y. and Finger, L. W. (1974c) The effects of cation substitution on the symmetry and the tetrahedral chain configuration in pyroxenes. *Carnegie Institution of Washington Year Book*, 73, 522–525.
- Ohashi, Y. and Finger, L. W. (1976) The effect of Ca substitution on the structure of clinoenstatite. *Carnegie Institution of Washington Year Book*, 75, 743–746.
- Ohashi, Y., Burnham, C. W., and Finger, L. W. (1975) The effect of Ca–Fe substitution on the clinopyroxene crystal structure. *American Mineralogist*, 60, 423–434.
- Okamura, F. P., Ghose, S., and Ohashi, H. (1974) Structure and crystal chemistry of calcium Tschermak's pyroxene, $CaAl_2Si_2O_6$. *American Mineralogist*, 59, 549–557.
- Pannhorst, W. (1979) Structural relationships between pyroxenes. *Neues Jahrbuch für Mineralogie Abhandlungen*, 135, 1–17.
- Papike, J. J. and Cameron, M. (1976) Crystal chemistry of silicate minerals of geophysical interest. *Reviews of Geophysics and Space Physics*, 14, 37–80.
- Papike, J. J. and Ross, M. (1970) Gedrites: crystal structures and

- intracrystalline cation distributions. *American Mineralogist*, 55, 1945-1972.
- Papike, J. J. and White, C. (1979) Pyroxenes from the planetary basalts: characterization of "other" than quadrilateral components. *Geophysical Research Letters*, 6, 913-916.
- Papike, J. J., Cameron, K. L., and Baldwin, K. (1974) Amphiboles and pyroxenes: Characterization of *Other* than quadrilateral components and estimates of ferric iron from microprobe data. *Geological Society of America Abstracts with Programs*, 6, 1053-1054.
- Papike, J. J., Prewitt, C. T., Sueno, S., and Cameron, M. (1973) Pyroxenes: comparisons of real and ideal structural topologies. *Zeitschrift für Kristallographie*, 138, 254-273.
- Papike, J. J., Bence, A. E., Brown, G. E., Prewitt, C. T., and Wu, C. H. (1971) Apollo 12 clinopyroxenes: exsolution and epitaxy. *Earth and Planetary Science Letters*, 10, 307-315.
- Peacor, D. R. (1967) Refinement of the crystal structure of a pyroxene of formula $M_1M_{II}(Si_{1.5}Al_{0.5})O_6$. *American Mineralogist*, 52, 31-41.
- Phakey, P. P. and Ghose, S. (1973) Direct observation of anti-phase domain structure in omphacite. *Contributions to Mineralogy and Petrology*, 39, 239-245.
- Poldervaart, A. and Hess, H. H. (1951) Pyroxenes in the crystallization of basaltic magma. *Journal of Geology*, 59, 472-489.
- Prewitt, C. T. (Ed.) (1980) *Pyroxenes*. Mineralogical Society of America Reviews in Mineralogy, Vol. 7. Mineralogical Society of America, Washington, D. C.
- Prewitt, C. T. and Burnham, C. W. (1966) The crystal structure of jadeite, $NaAlSi_2O_6$. *American Mineralogist*, 51, 956-975.
- Prewitt, C. T., Brown, G. E., and Papike, J. J. (1971) Apollo 12 clinopyroxenes: high temperature X-ray diffraction studies. *Proceedings of the 2nd Lunar Science Conference*, 1, 59-68.
- Ribbe, P. H. and Prunier, Jr., A. R. (1977) Stereochemical systematics of ordered *C2/c* silicate pyroxenes. *American Mineralogist*, 62, 710-720.
- Robinson, K., Gibbs, G. V., and Ribbe, P. H. (1971) Quadratic elongation: a quantitative measure of distortion in coordination polyhedra. *Science*, 172, 567-570.
- Robinson, P. (1980) The composition space of terrestrial pyroxenes: internal and external limits. In C. T. Prewitt, Ed., *Pyroxenes*. Mineralogical Society of America Reviews in Mineralogy, Vol. 7. Mineralogical Society of America, Washington, D. C.
- Robinson, P., Jaffe, H. W., Ross, M., and Klein, Jr., C. (1971) Orientation of exsolution lamellae in clinopyroxenes and clin amphiboles: consideration of optimal phase boundaries. *American Mineralogist*, 56, 909-939.
- Robinson, P., Ross, M., Nord, Jr., G. L., Smyth, J. R., and Jaffe, H. W. (1977) Exsolution lamellae in augite and pigeonite: fossil indicators of lattice parameters at high temperature and pressure. *American Mineralogist*, 62, 857-873.
- Saxena, S. K. and Ghose, S. (1970) Order-disorder and the activity-composition relation in a binary crystalline solution. I. Metamorphic orthopyroxene. *American Mineralogist*, 55, 1219-1225.
- Saxena, S. K. and Ghose, S. (1971) Mg^{2+} - Fe^{2+} order-disorder and the thermodynamics of the orthopyroxene crystalline solution. *American Mineralogist*, 56, 532-559.
- Saxena, S. K., Ghose, S., and Turnock, A. C. (1974) Cation distribution in low-calcium pyroxenes: dependence on temperature and calcium content and the thermal history of lunar and terrestrial pigeonites. *Earth and Planetary Science Letters*, 21, 194-200.
- Schweitzer, E. L., Papike, J. J., and Bence, A. E. (1978) Clinopyroxenes from deep sea basalts: a statistical analysis. *Geophysical Research Letters*, 5, 573-576.
- Schweitzer, E. L., Papike, J. J., and Bence, A. E. (1979) Statistical analysis of clinopyroxenes from deep-sea basalts. *American Mineralogist*, 64, 501-513.
- Shannon, R. D. and Prewitt, C. T. (1969) Effective ionic radii in oxides and fluorides. *Acta Crystallographica*, B25, 925-946.
- Shannon, R. D. and Prewitt, C. T. (1970) Revised values of effective ionic radii. *Acta Crystallographica*, B26, 1046-1048.
- Simmons, E. C., Lindsley, D. H., and Papike, J. J. (1974) Phase relations and crystallization sequence in a contact-metamorphosed rock from the Gunflint Iron Formation, Minnesota. *Journal of Petrology*, 15, 539-565.
- Smith, J. V. (1969) Crystal structure and stability of the $MgSiO_3$ polymorphs; physical properties and phase relations of Mg,Fe pyroxenes. *Mineralogical Society of America Special Paper*, 2, 3-29.
- Smyth, J. R. (1971) Protoenstatite: a crystal-structure refinement at 1100°C. *Zeitschrift für Kristallographie*, 134, 262-274.
- Smyth, J. R. (1973) An orthopyroxene structure up to 850°C. *American Mineralogist*, 58, 636-648.
- Smyth, J. R. (1974a) Low orthopyroxene from a lunar deep crustal rock: a new pyroxene polymorph of space group $P2_1ca$. *Geophysical Research Letters*, 1, 27-29.
- Smyth, J. R. (1974b) The high temperature crystal chemistry of clinohypersthene. *American Mineralogist*, 59, 1069-1082.
- Smyth, J. R. and Ito, J. (1977) The synthesis and crystal structure of a magnesium-lithium-scandium protopyroxene. *American Mineralogist*, 62, 1252-1257.
- Snellenburg, J. W. (1975) Computer simulation of the distribution of octahedral cations in orthopyroxene. *American Mineralogist*, 60, 441-447.
- Steele, I. M. (1975) Mineralogy of lunar norite 78235; second lunar occurrence of $P2_1ca$ pyroxene from Apollo 17 soils. *American Mineralogist*, 60, 1086-1091.
- Sueno, S., Cameron, M., and Prewitt, C. T. (1976) Orthoferrosilite: high-temperature crystal chemistry. *American Mineralogist*, 61, 38-53.
- Takeda, H. (1972a) Structural studies of rim augite and core pigeonite from lunar rock 12052. *Earth and Planetary Science Letters*, 15, 65-71.
- Takeda, H. (1972b) Crystallographic studies of coexisting aluminan orthopyroxene and augite of high-pressure origin. *Journal of Geophysical Research*, 77, 5798-5811.
- Takeda, H. and Ridley, W. I. (1972) Crystallography and chemical trends of orthopyroxene-pigeonite from rock 14310 and coarse fine 12033. *Proceedings of the 3rd Lunar Science Conference*, 1, 423-430.
- Takeda, H., Miyamoto, M., and Reid, A. M. (1974) Crystal chemical control of element partitioning for coexisting chromite-ulvöspinel and pigeonite-augite in lunar rocks. *Proceedings of the 5th Lunar Science Conference*, 1, 727-741.
- Thompson, Jr., J. B. (1970) Geometrical possibilities for amphibole structures: model biopyriboles. *American Mineralogist*, 55, 292-293.
- Tokonami, M., Horiuchi, H., Nakano, A., Akimoto, S.-I., and Morimoto, N. (1979) The crystal structure of the pyroxene-type $MnSiO_3$. *Mineralogical Journal*, 9, 424-426.
- Tossell, J. A. and Gibbs, G. V. (1977) Molecular orbital studies of geometries and spectra of minerals and inorganic compounds. *Physics and Chemistry of Minerals*, 2, 21-57.

- Veblen, D. R. and Burnham, C. W. (1978) New biopyriboles from Chester, Vermont: II. The crystal chemistry of jimthompsonite, clinojimthompsonite, and chesterite, and the amphibole-mica reaction. *American Mineralogist*, 63, 1053-1073.
- Virgo, D. and Hafner, S. S. (1969) Fe²⁺,Mg order-disorder in heated clinopyroxenes. *Mineralogical Society of America Special Paper*, 2, 67-81.
- Virgo, D. and Hafner, S. S. (1970) Fe²⁺,Mg order-disorder in natural orthopyroxenes. *American Mineralogist*, 55, 201-223.
- Wenk, H.-R. (Ed.) (1976) *Electron Microscopy in Mineralogy*. Springer-Verlag, Heidelberg.
- Wood, B. J. and Henderson, C. M. B. (1978) Composition and unit-cell parameters of synthetic non-stoichiometric tschermakitic clinopyroxenes. *American Mineralogist*, 63, 66-72.
- Yamaguchi, Y. and Tomita, K. (1970) Clinoenstatite as an exsolution phase in diopside. *Memoirs of the Faculty of Science, Kyoto University, Series of Geology and Mineralogy*, 37, 173-180.
- Yund, R. A. and McCallister, R. H. (1970) Kinetics and mechanisms of exsolution. *Chemical Geology*, 6, 5-30.
- Zussman, J. (1968) The crystal chemistry of pyroxenes and amphiboles. I. Pyroxenes. *Earth-Science Reviews*, 4, 39-67.

*Manuscript received, June 16, 1980;
accepted for publication, July 17, 1980.*

Appendix tables

Table A1. Pyroxene end-members for Others

			Fe ²⁺ /Fe ²⁺ +Mg	Fe ³⁺ >Al>Cr	Al>Fe ³⁺ >Cr	Cr>Al>Fe ³⁺	Ca/Ca+P ²⁺ in M2 site
1.	NAT	NaTi _{0.5} R _{0.5} ⁴⁺ Si ₂ O ₆					
	(1)	Fe²⁺-NAT NaTi _{0.5} Fe _{0.5} ²⁺ Si ₂ O ₆	>0.5	---	---	---	---
	(2)	Mg-NAT NaTi _{0.5} Mg _{0.5} Si ₂ O ₆	<0.5	---	---	---	---
2.	TAL	R ²⁺ Ti _{0.5} R _{0.5} ²⁺ (SiAl)O ₆					
	(3)	CaFe²⁺-TAL CaTi _{0.5} Fe _{0.5} ²⁺ (SiAl)O ₆	>0.5	---	---	---	>0.5
	(4)	CaMg-TAL CaTi _{0.5} Mg _{0.5} (SiAl)O ₆	<0.5	---	---	---	>0.5
	(5)	Fe²⁺-TAL Fe ²⁺ Ti _{0.5} Fe _{0.5} ²⁺ (SiAl)O ₆	>0.5	---	---	---	<0.5
	(6)	Mg-TAL MgTi _{0.5} Mg _{0.5} (SiAl)O ₆	>0.5	---	---	---	<0.5
3.	AC-JD-UR	NaR ³⁺ Si ₂ O ₆					
	(7)	Jadeite NaAlSi ₂ O ₆	---	---	YES	---	---
	(8)	Acmite NaFe ³⁺ Si ₂ O ₆	---	YES	---	---	---
	(9)	Ureyite NaCr ³⁺ Si ₂ O ₆	---	---	---	YES	---
4.	CATS	R ²⁺ R ³⁺ (SiAl)O ₆					
	(10)	CaAl-CATS CaAl(SiAl)O ₆	---	---	YES	---	>0.5
	(11)	CaFe³⁺-CATS CaFe ³⁺ (SiAl)O ₆	---	YES	---	---	>0.5
	(12)	CaCr³⁺-CATS CaCr ³⁺ (SiAl)O ₆	---	---	---	YES	>0.5
	(13)	Fe²⁺-Al-CATS Fe ²⁺ Al(SiAl)O ₆	>0.5	---	YES	---	<0.5
	(14)	Fe²⁺Fe³⁺-CATS Fe ²⁺ Fe ³⁺ (SiAl)O ₆	>0.5	YES	---	---	<0.5
	(15)	Fe²⁺Cr³⁺-CATS Fe ²⁺ Cr ³⁺ (SiAl)O ₆	>0.5	---	---	YES	<0.5
	(16)	MgAl-CATS MgAl(SiAl)O ₆	<0.5	---	YES	---	<0.5
	(17)	MgFe³⁺-CATS MgFe ³⁺ (SiAl)O ₆	<0.5	YES	---	---	<0.5
	(18)	MgCr³⁺-CATS MgCr ³⁺ (SiAl)O ₆	<0.5	---	---	YES	<0.5
5.	NATAL	NaTiSiAlO ₆					

Table A2. Procedure for assigning a pyroxene "general" name based on chemistry only

- 1) Calculate cations per six oxygen atoms and assign cations to sites in order of increasing ionic radius--start with T, then M1, then M2 site.
- 2) If (Ca + Na) > 0.8 and 0.2 < Na/(Na + Ca) < 0.8, the pyroxene name is either aegirine-augite or omphacite.
If Fe³⁺/VIAl > 1.0, the name is aegirine augite
If Fe³⁺/VIAl < 1.0, the name is omphacite
- 3) If Ca > 0.5 and Mn (M1) > 0.5, the pyroxene name is johannsenite.
- 4) If the pyroxene is not named by this point, check if Others is greater than or less than 50%. If >50%, use the Others name from Table A1. If <50%, use one of the "general" names given in the following four steps.
- 5) If Ca < 0.15 and Fe²⁺/Mg < 1, the name is Mg pyroxene
- 6) If Ca < 0.15 and Fe²⁺/Mg > 1, the name is Fe pyroxene
- 7) If Ca > 0.15 and Fe²⁺/Mg < 1, the name is Mg augite
- 8) If Ca > 0.15 and Fe²⁺/Mg > 1, the name is Fe augite

Table A3. Superior analyses from Deer *et al.* (1978)

Analysis No. Page-Column	%Quad	%Others	"General" Name	Best Name for Others	Analysis No. Page-Column	%Quad	%Others	"General" Name	Best Name for Others
35-2	96	4	Mg Pyroxene	MgAl Cats	216-6	98	2	Fe Augite	--
35-3	97	3	Mg Pyroxene	MgFe ³⁺ Cats	216-7	79	21	Fe Augite	CaFe ³⁺ Cats
35-5	84	16	Mg Pyroxene	MgAl Cats	216-10	96	4	Fe Augite	CaAl Cats
36-6	94	6	Mg Pyroxene	MgFe ³⁺ Cats	218-3	89	11	Fe Augite	Acmite
36-7	94	6	Mg Pyroxene	MgFe ³⁺ Cats	219-7	91	9	Fe Augite	CaFe ³⁺ Cats
36-8	91	9	Mg Pyroxene	MgFe ³⁺ Cats					
36-10	90	10	Mg Pyroxene	MgFe ³⁺ Cats	219-10	76	24	Aegirine Augite	--
37-11	85	15	Mg Pyroxene	MgAl Cats					
37-12	94	6	Mg Pyroxene	MgAl Cats	220-13	95	5	Fe Augite	NATAL
38-13	95	5	Mg Pyroxene	MgAl Cats	301-3	88	12	Mg Augite	CaFe ³⁺ Cats
38-17	92	8	Mg Pyroxene	MgAl Cats	301-4	90	10	Mg Augite	CaFe ³⁺ Cats
38-18	95	5	Mg Pyroxene	Mg TAL	302-7	90	10	Mg Augite	CaAl Cats
39-22	97	3	Mg Pyroxene	Mg TAL	302-8	89	11	Mg Augite	CaFe ³⁺ Cats
39-23	95	5	Mg Pyroxene	NATAL	302-9	88	12	Mg Augite	NATAL
39-24	91	9	Mg Pyroxene	MgAl Cats					
40-27	98	2	Fe Pyroxene	Fe ²⁺ TAL	303-11	86	14	Mg Augite	CaFe ³⁺ Cats
40-29	98	2	Fe Pyroxene	Fe ²⁺ TAL	303-12	89	11	Mg Augite	CaMg TAL
40-30	84	16	Fe Pyroxene	Fe ²⁺ TAL					
41-1	96	4	Mg Pyroxene	MgFe ³⁺ Cats	304-16	91	9	Mg Augite	CaFe ³⁺ Cats
41-2	87	13	Mg Pyroxene	MgAl Cats	304-17	90	10	Mg Augite	CaMg TAL
41-4	92	8	Mg Pyroxene	MgFe ³⁺ Cats	304-19	91	9	Mg Augite	CaFe ³⁺ Cats
41-5	92	8	Mg Pyroxene	Mg TAL	305-2	86	14	Mg Augite	CaFe ³⁺ Cats
42-6	86	14	Mg Pyroxene	MgAl Cats	305-3	83	17	Mg Augite	CaFe ³⁺ Cats
42-8	97	3	Mg Pyroxene	MgAl Cats	305-5	77	23	Mg Augite	CaMg TAL
42-9	76	24	Mg Pyroxene	MgAl Cats					
42-10	80	20	Mg Pyroxene	MgAl Cats	306-6	91	9	Mg Augite	CaFe ³⁺ Cats
43-11	87	13	Mg Pyroxene	MgFe ³⁺ Cats	306-7	89	11	Mg Augite	NATAL
43-13	92	8	Mg Pyroxene	MgFe ³⁺ Cats	306-8	90	10	Mg Augite	CaMg TAL
44-17	92	8	Fe Pyroxene	Fe ²⁺ Fe ³⁺ Cats	306-9	87	13	Mg Augite	NATAL
44-18	86	14	Fe Pyroxene	Fe ²⁺ Al Cats	307-11	91	9	Mg Augite	NATAL
44-19	89	11	Fe Pyroxene	Fe ²⁺ TAL	307-12	90	10	Mg Augite	NATAL
45-22	93	7	Fe Pyroxene	Fe ²⁺ Fe ³⁺ Cats	307-13	89	11	Mg Augite	CaAl Cats
45-24	94	6	Fe Pyroxene	Fe ²⁺ Al Cats					
45-25	96	4	Fe Pyroxene	NATAL	308-1	81	19	Mg Augite	CaAl Cats
47-33	99	1	Fe Pyroxene	Fe ²⁺ Fe ³⁺ Cats	308-2	78	22	Mg Augite	CaAl Cats
47-34	97	3	Fe Pyroxene	Fe ²⁺ Al Cats	308-3	78	22	Mg Augite	CaAl Cats
48-4	91	9	Mg Pyroxene	MgAl Cats	308-4	70	30	Mg Augite	CaAl Cats
49-6	82	18	Mg Pyroxene	MgAl Cats	309-5	74	26	Mg Augite	CaAl Cats
49-7	87	13	Mg Pyroxene	MgAl Cats	309-6	71	29	Mg Augite	CaAl Cats
50-1	100	0	Mg Pyroxene	---					
170-7	94	6	Mg Pyroxene	Mg TAL	309-7	68	32	Mg Augite	CaAl Cats
170-10	95	5	Mg Pyroxene	MgFe ³⁺ Cats	310-2	88	12	Mg Augite	CaAl Cats
171-13	92	8	Fe Pyroxene	Fe ²⁺ Fe ³⁺ Cats	310-4	90	10	Mg Augite	NATAL
203-6	94	6	Mg Augite	CaAl Cats	310-5	91	9	Mg Augite	CaFe ³⁺ Cats
203-8	92	8	Mg Augite	CaAl Cats	311-6	91	9	Mg Augite	CaAl Cats
203-9	98	2	Mg Augite	---	311-7	86	14	Mg Augite	CaFe ³⁺ Cats
204-12	85	15	Mg Augite	CaAl Cats					
204-13	94	6	Mg Augite	Jadeite	311-8	87	13	Fe Augite	CaFe ³⁺ Cats
205-16	94	6	Mg Augite	Jadeite	312-2	90	10	Fe Augite	CaFe ³⁺ Cats
205-18	92	8	Mg Augite	CaAl Cats	312-3	93	7	Fe Augite	NATAL
205-19	84	16	Mg Augite	CaAl Cats	314-11	86	14	Fe Augite	CaFe ³⁺ Cats
206-5	91	9	Mg Augite	CaAl Cats	314-13	94	6	Fe Augite	NATAL
207-6	76	24	Mg Augite	CaAl Cats	315-16	91	9	Fe Augite	CaFe ³⁺ Cats
207-7	94	6	Mg Augite	CaFe ³⁺ Cats	315-17	93	7	Fe Augite	NATAL
207-10	85	15	Mg Augite	Jadeite	316-2	89	11	Fe Augite	CaFe ³⁺ Cats
207-11	88	12	Mg Augite	Ureyite	316-3	84	16	Fe Augite	Fe ²⁺ Al Cats
208-2	93	7	Mg Augite	CaAl Cats					
208-5	81	19	Mg Augite	CaAl Cats	317-1	81	19	Mg Augite	MgAl Cats
209-7	91	9	Mg Augite	CaAl Cats	317-2	89	11	Mg Augite	MgFe ³⁺ Cats
209-8	89	11	Mg Augite	CaAl Cats	319-1	66	34	Mg Augite	CaMg TAL
209-9	88	12	Mg Augite	CaFe ³⁺ Cats	320-7	78	22	Mg Augite	CaMg TAL
209-10	89	11	Mg Augite	CaFe ³⁺ Cats					
210-3	84	16	Mg Augite	CaFe ³⁺ Cats	320-8a	44	56	CaMgTAL	--
210-4	84	16	Mg Augite	CaAl Cats					
210-5	96	4	Mg Augite	Acmite	320-12	58	42	Fe Augite	CaFe ²⁺ TAL
211-6	96	4	Mg Augite	CaAl Cats					
211-9	89	11	Mg Augite	CaFe ³⁺ Cats	321-3	73	27	Mg Augite	CaFe ³⁺ Cats
211-10	91	9	Mg Augite	CaFe ³⁺ Cats	321-5	57	43	Mg Augite	CaFe ³⁺ Cats
212-12	84	16	Mg Augite	CaMg TAL					
212-13	76	24	Mg Augite	CaFe ³⁺ Cats	322-1	71	29	Omphacite	--
213-17	85	15	Mg Augite	NATAL					
213-18	90	10	Mg Augite	CaFe ³⁺ Cats	323-5	77	23	Mg Augite	Acmite
214-22	85	15	Mg Augite	NATAL					
214-23	91	9	Mg Augite	CaFe ³⁺ Cats	323-7	70	30	Aegirine Augite	--
214-24	91	9	Mg Augite	CaFe ³⁺ Cats					
214-25	86	14	Mg Augite	Acmite	403-1	54	46	Mg Augite	CaAl Cats
214-26	97	3	Mg Augite	Jadeite	404-6	72	28	Mg Augite	CaAl Cats
215-2	81	19	Mg Augite	CaFe ³⁺ Cats	404-7	70	30	Mg Augite	CaFe ³⁺ Cats
					405-10	75	25	Mg Augite	CaAl Cats
					405-11	81	19	Mg Augite	CaAl Cats
					406-16a	44	56	CaMgTAL	--
					417-2	97	3	Johannsenite	--
					417-3	97	3	Johannsenite	--
					417-4	95	5	Johannsenite	--
					418-6	92	8	Johannsenite	--

*Same analysis is reported twice in Deer *et al.* (1978).

Table A3. (continued)

Analysis No. Page-Column	%Quad	%Others	"General" Name	Best Name for Others
419-2	98	2	Fe Augite	CaAl Cats
428-4	64	36	Omphacite	--
430-4	64	36	Omphacite	--
431-6	65	35	Omphacite	--
432-12	51	49	Omphacite	--
433-2	50	50	Omphacite	--
433-3	51	49	Omphacite	--
433-5	48	52	Omphacite	--
434-6	51	49	Omphacite	--
434-7	48	52	Omphacite	--
464-1	1	99	Jadeite	--
464-2	5	95	Jadeite	--
466-11	10	90	Jadeite	--
466-12	10	90	Jadeite	--
466-14	15	85	Jadeite	--
487-1	2	98	Acmite	--
488-7	6	94	Acmite	--
488-8	7	93	Acmite	--
489-1	77	23	Mg Augite	Acmite
489-2	65	35	Aegirine Augite	--
489-3	52	48	Aegirine Augite	--
489-5	60	40	Aegirine Augite	--
490-6	53	47	Aegirine Augite	--
490-8	43	57	Aegirine Augite	--
490-9	39	61	Aegirine Augite	--
491-13	17	83	Acmite	--
491-15	13	87	Acmite	--
494-3	25	75	Acmite	--

Table A4. Crystal data for pyroxenes included in tables and plotted in figures

No.	Name (Composition) ^a	Space Group	Unit Cell Parameters					O3-O3-O3(0) ^b	Source and Locality	Reference (Crystal Data)
			a(Å)	b(Å)	c(Å)	d(Å)	v(Å ³)			
1.	CaNiSi ₂ O ₆	C2/c	9.737	8.899	5.231	105.9	435.9	165.1	synthetic	Schlenker et al. (1977) (in Ribbe and Prunier, 1977)
2.	diopside CaMgSi ₂ O ₆	C2/c	9.746(4)	8.899(5)	5.251(6)	105.63(6)	438.6(3)	166.38(11)	Gouverneur talc district, Gouverneur, New York	Clark et al. (1969)
3.	CaCoSi ₂ O ₆	C2/c	9.797	8.954	5.243	105.4	443.4	164.8	synthetic	Schlenker et al. (1977) (in Ribbe and Prunier, 1977)
4.	hedenbergite CaFe ²⁺ Si ₂ O ₆	C2/c	9.845(1)	9.024(1)	5.245(1)	104.74(1)	450.6(1)	164.5(1)	synthetic	Cameron et al. (1973)
5.	johannsenite CaMnSi ₂ O ₆	C2/c	9.978(9)	9.156(9)	5.293(5)	105.48(3)	466.0	163.78(47)	U.S.N.M. #R3118 Schio-Vincenti mine, Venetia, northern Italy	Freed and Peacor (1967)
6.	jadeite NaAlSi ₂ O ₆	C2/c	9.418(1)	8.562(2)	5.219(1)	107.58(1)	401.20(15)	174.7(2)	#184 (H.S. Yoder); veinlets in schist; Santa Rita Peak, New Idria District, California	Prewitt and Burnham (1966)
7.	ureyite NaCrSi ₂ O ₆	C2/c	9.550(16)	8.712(7)	5.273(8)	107.44(16)	418.6(1.4)	172.1(2)	synthetic	Clark et al. (1969)
8.	acmite NaFe ³⁺ Si ₂ O ₆	C2/c	9.658(2)	8.795(2)	5.294(1)	107.42(2)	429.1(1)	174.0(2)	Green River Formation, Wyoming	Clark et al. (1969)
9.	NaSc ³⁺ Si ₂ O ₆	C2/c	9.8438(4)	9.0439(4)	5.3540(2)	107.215(2)	455.29	173.6(1)	synthetic	Hawthorne and Grundy (1973)
10.	NaIn ³⁺ Si ₂ O ₆	C2/c	9.9023(4)	9.1307(4)	5.3589(2)	107.200(1)	462.86	170.8(2)	synthetic	Hawthorne and Grundy (1974)
11.	spodumene LiAlSi ₂ O ₆	C2/c	9.449(3)	8.386(1)	5.215(2)	110.10(2)	388.1(1)	189.5	Newry, Maine	Clark et al. (1969)
12.	LiFe ³⁺ Si ₂ O ₆	C2/c	9.666(2)	8.669(1)	5.294(2)	110.15(2)	416.4(1)	180(2)	synthetic	Clark et al. (1969)
13.	LiSc ³⁺ Si ₂ O ₆	C2/c	9.8033(7)	8.9581(7)	5.3515(4)	110.281(4)	440.83	175.6(1)	synthetic	Hawthorne and Grundy (1977)
14.	Zn ₂ Si ₂ O ₆	C2/c	9.787(3)	9.161(2)	5.296(1)	111.42(3)	442.0(2)	161.3(1)	synthetic	Morimoto et al. (1975)
15.	Ca-Ts CaAlSiAlO ₆	C2/c	9.609(3)	8.652(2)	5.274(2)	106.06(2)	421.35(21)	165.93(6)	synthetic	Okamura et al. (1974)
16.	clinopyroxene	C2/c	9.812(1)	9.049(1)	5.233(1)	105.34(1)	448.1(1)	162.5(2)	synthetic	Ohashi et al. (1973)
17.	clinopyroxene	C2/c	9.781(2)	9.072(2)	5.246(2)	106.55(2)	446.2(3)	159.8(5)	synthetic	Ohashi et al. (1973)
18.	clinopyroxene	C2/c	9.760(6)	9.057(8)	5.234(3)	106.28(5)	444.1(6)	159.5(3)	synthetic	Ohashi et al. (1973)
19.	augite	C2/c	9.699(1)	8.844(1)	5.272(1)	106.97(2)	432.5(1)	165.8(2)	Kakanui, New Zealand	Clark et al. (1969)
20.	augite	C2/c	9.707(2)	8.858(2)	5.274(1)	106.52(3)	434.76	165.47(13)	HK56051801 of Kuno; alkaline olivine basalt; Takasima, North Kyushu, Japan; coexists with #33	Takeda (1972b)
21.	augite	C2/c	9.713(2)	8.964(3)	5.266(2)	105.93(2)	440.89	164.26	lamellae in pyroxene grain from lunar (KREEP) basalt 14310,90; cf. pigeonite host #64	Takeda et al. (1974)
22.	augite	C2/c	9.704(4)	8.968(5)	5.248(3)	105.65(3)	439.78	—	lamellae in pyroxene grain from Juvinas eucrite, France; cf. pigeonite host #65	Takeda et al. (1974)
23.	augite	C2/c	9.726(2)	8.909(3)	5.268(1)	106.82(2)	436.94	164.13	rim from pyroxene grain in lunar basalt 12052; cf. core pigeonite #63	Takeda (1972a)
24.	subcalcic diopside	C2/c	9.699(5)	8.871(2)	5.251(3)	107.03(3)	431.9(3)	166.2(3)	#1600E4; pyroxene nodules, Thaba Putsoa pipe, Lesotho	McCallister et al. (1974)
24b.	clinopyroxene	C2/c	9.684(2)	8.840(3)	5.266(1)	106.89(3)	431.3(2)	165.57	megacryst; nephelinite breccia; KaKanu, New Zealand	McCallister et al. (1976)

Table A4. (continued)

24c.	clinopyroxene	<u>C2/c</u>	9.683(3)	8.846(3)	5.264(1)	106.83(2)	431.6(2)	167.15		eclogite; KaKanui, New Zealand	McCallister <i>et al.</i> (1976)
25.	fassaite (titanaugite)	<u>C2/c</u>	9.794(5)	8.906(5)	5.319(3)	105.90(3)	446.20	166.0		phenocrysts in nepheline jacupirangite; Hesseau Hill, Oka, Quebec	Peacor (1967)
26.	fassaite	<u>C2/c</u>	9.80(1)	8.85(1)	5.360(5)	105.62(17)	447.70	165.10		Allende meteorite; Chihuahua, Mexico	Dowty and Clark (1973)
27.	fassaite	<u>C2/c</u>	9.738(1)	8.874(2)	5.2827(5)	105.89(1)	439.1(1)	165.4(2)		Angra dos Reis achondrite; Rio de Janeiro, Brazil	Hazen and Finger (1977a)
28.	Ca-Ts	<u>C2/c</u>	9.780(2)	8.782(2)	5.369(1)	105.78(1)	443.754	--		synthetic	Ghose <i>et al.</i> (1975)
29.	omphacite	<u>C2/c</u>	9.646(6)	8.824(5)	5.270(6)	106.59(8)	429.9(5)	168.7(2)		Schmitt #1725; Hareidland, Sunmore, Norway	Clark <i>et al.</i> (1979)
30.	orthoenstatite Mg ₂ Si ₂ O ₆	<u>Pbca</u>	18.216(2)	8.813(1)	5.179(1)	--	831.42	A=158.9(1) B=139.0(1)		synthetic	Hawthorne and Ito (1977)
31.	-- Zn ₂ Si ₂ O ₆	<u>Pbca</u>	18.204(5)	9.087(3)	5.278(2)	--	873.1(3)	A=178.3(4) B=149.2(3)		synthetic	Morimoto <i>et al.</i>
32.	orthoferrosilite Fe ₂ ²⁺ Si ₂ O ₆	<u>Pbca</u>	18.418(2)	9.078(1)	5.2366(4)	--	875.6(1)	A=169.11 B=143.76(24)		synthetic	Sueno <i>et al.</i> (1976)
33.	bronzite	<u>Pbca</u>	18.276(3)	8.819(2)	5.196(1)	--	837.47	A=162.43(12) B=140.89(11)		HK56051802 of Kuno; alkaline olivine basalt; Takasima, North Kyushu, Japan; coexists with #20	Takeda (1972b)
34.	bronzite	<u>Pbca</u>	18.304(3)	8.887(2)	5.215(1)	--	848.31	--		lunar rock (KREEP fragment) 12033, 99	Takeda and Ridley (1972)
35.	bronzite	<u>Pbca</u>	18.301(3)	8.869(2)	5.215(1)	--	846.45	A=164.73 B=142.50		lunar basalt 14310, 90	Takeda and Ridley (1972)
36.	bronzite	<u>Pbca</u>	18.233(4)	8.836(3)	5.194(2)	--	836.79	A=162.1 B=141.7		Shaw chondrite; Lincoln County, Colorado	Dodd <i>et al.</i> (1975)
37.	bronzite	<u>Pbca</u>	18.276(7)	8.861(4)	5.201(3)	--	842.27	A=163.41(24) B=141.75(21)		U.S.N.M. #46; Johnstown achondrite; Weld County, Colorado	Miyamoto <i>et al.</i> (1975)
38.	bronzite	<u>Pbca</u>	18.3291(31)	8.8853(11)	5.2212(8)	--	850.32	A=163.70 B=143.15		#K7; Luna 20	Ghose and Wan (1973)
39.	aluminous bronzite	<u>Pbca</u>	18.221(2)	8.770(1)	5.192(1)	--	829.67	A=161.88 B=136.80		#2; granulite from Aldan Shield, ?U.S.S.R.	Kosoi <i>et al.</i> (1974)
40.	aluminous bronzite	<u>Pbca</u>	18.224(5)	8.775(5)	5.179(5)	--	828.20	A=161.83 B=137.22		#3; granulite from Aldan Shield, ?U.S.S.R.	Kosoi <i>et al.</i> (1974)
41.	hypersthene	<u>Pbca</u>	18.310(10)	8.927(5)	5.226(5)	--	854.21	A=167.83 B=143.90		#37218 of Ramberg; granulite; Greenland	Ghose (1965)
42.	hypersthene	<u>Pbca</u>	18.295(2)	8.901(1)	5.218(1)	--	849.72	A=165.53 B=142.67		#1; granulite from Aldan Shield, ?U.S.S.R.	Kosoi <i>et al.</i> (1974)
43.	hypersthene	<u>Pbca</u>	18.313(3)	8.912(2)	5.210(1)	--	850.30	--		synthetic	Ghose <i>et al.</i> (1975)
44.	ferrohypersthene	<u>Pbca</u>	18.363(5)	8.990(3)	5.232(4)	--	863.7(5)	A=167.2 B=144.5		B1-9 of Virgo and Hafner (1969); metamorphosed iron formation; Quebec	Smyth (1973)
45.	aluminous hypersthene	<u>Pbca</u>	18.220(5)	8.765(3)	5.188(1)	--	828.51	A=161.65 B=136.39		393/8; Gneiss, Sutam River, Aldan Shield, ?U.S.S.R.	Brovkin <i>et al.</i> (1973)
46.	eulite	<u>Pbca</u>	18.405(1)	9.0338(7)	5.2390(4)	--	871.08(14)	A=168.8(1) B=143.9(1)		XYZ of Ramberg; granulite from Greenland	Burnham <i>et al.</i> (1971)
47.	(Mg, Co) orthopyroxene	<u>Pbca</u>	18.233(7)	8.836(6)	5.188(3)	--	835.82	A=160.1(1) B=139.6(1)		synthetic	Hawthorne and Ito (1978)
48.	(Mg, Mn) orthopyroxene	<u>Pbca</u>	18.270(6)	8.833(6)	5.195(3)	--	838.36	A=160.6(2) B=140.7(2)		synthetic	Hawthorn and Ito (1978)
49.	(Mg, Mn, Co) orthopyroxene	<u>Pbca</u>	18.246(3)	8.839(2)	5.196(1)	--	837.99	A=161.6(2) B=141.4(2)		synthetic	Hawthorne and Ito (1977)
50.	(Zn, Mg) orthopyroxene	<u>Pbca</u>	18.201(5)	8.916(2)	5.209(2)	--	845.32	A=166.9(6) B=143.6(5)		synthetic	Morimoto <i>et al.</i> (1975)
51.	(Zn, Mg) orthopyroxene	<u>Pbca</u>	18.231(4)	8.893(2)	5.209(1)	--	844.53	--		synthetic	Ghose <i>et al.</i> (1975)
52.	(Ni, Mg)	<u>Pbca</u>	18.203(4)	8.788(2)	5.171(1)	--	827.19	--		synthetic	Ghose <i>et al.</i>

Table A4. (continued)

	orthopyroxene									(1975)
53.	(Co, Mg) orthopyroxene	Pbca	18.229(4)	8.847(2)	5.182(1)	—	835.71	—	synthetic	Ghose et al. (1975)
53b.	aluminous orthopyroxene	Pbca	18.2248(39)	8.7822(24)	5.1927(12)	—	831.11	A=160.35 B=138.10	#SQ2-70; spinel lherzolite; Baja, California	Ganguly and Ghose (1979)
53c.	aluminous orthopyroxene	Pbca	18.1991(48)	8.7800(14)	5.1666(12)	—	825.56	A=158.81 B=137.13	synthetic	Ganguly and Ghose (1979)
54.	clinostatite Mg ₂ Si ₂ O ₆	P2 ₁ /c	9.620(5)	8.825(5)	5.188(5)	108.333(167)	418.09	A=199.0 ^c B=134.0	Bishopville enstatite achondrite; Lee County, S. Carolina	Morimoto et al. (1960)
55.	clinoferrisilite Fe ₂ ⁺ Si ₂ O ₆	P2 ₁ /c	9.7085(8)	9.0872(11)	5.2284(6)	108.432(4)	437.6(1)	A=193.0 B=142.0	synthetic	Burnham (1965, 1966)
56.	clinopyroxene	P2 ₁ /c	9.779(1)	9.088(1)	5.258(1)	107.39(1)	445.9(2)	A=164.2(8) B=156.0(7)	synthetic	Ohashi et al. (1975)
57.	enstatite Mg ₂ Si ₂ O ₆	P2 ₁ /c	9.605(1)	8.813(1)	5.166(1)	108.46(1)	415.1(1)	A=202.76 B=138.31	synthetic	Ohashi and Finger (1976)
58.	clinopyroxene	P2 ₁ /c	9.639(1)	8.835(1)	5.192(1)	108.39(1)	419.6(1)	A=200.37 B=141.99	synthetic	Ohashi and Finger (1976)
59.	clinopyroxene	P2 ₁ /c	9.657(1)	8.846(2)	5.208(1)	108.34(1)	422.3(1)	A=197.99 B=145.01	synthetic	Ohashi and Finger (1976)
60.	pigeonite	P2 ₁ /c	9.706(2)	8.950(1)	5.246(1)	108.59(1)	431.94	A=190.4 B=148.5(5)	andesite; Isle of Mull, Scotland	Morimoto and Güven (1970)
61.	pigeonite	P2 ₁ /c	9.706(2)	8.950(1)	5.246(1)	108.59(1)	432.0(2)	A=186.1 B=151.0(3)	andesite; Isle of Mull, Scotland	Brown et al. (1972)
62.	pigeonite	P2 ₁ /c	9.678(10)	8.905(10)	5.227(5)	108.71(8)	430.6	A=194.3 B=145.5(5)	lunar basalt 10003,38	Clark et al. (1971)
63.	pigeonite	P2 ₁ /c	9.688(3)	8.890(3)	5.238(2)	108.40(4)	428.07	A=188.85 B=150.05	core from pyroxene grain in lunar basalt 12052; cf. augite rim #23	Takeda (1972a)
64.	pigeonite	P2 ₁ /c	9.715(1)	8.963(1)	5.239(1)	108.64(2)	432.26	A=190.48 B=147.78	host in pyroxene grain from lunar (KREEP) basalt 14310,90; cf. augite lamellae #21	Takeda et al. (1974)
65.	pigeonite	P2 ₁ /c	9.698(2)	8.967(2)	5.223(1)	108.75(2)	430.10	—	host in pyroxene grain from Juvinas eucrite; France cf. augite lamellae #22	Takeda et al. (1974)
66.	pigeonite	P2 ₁ /c	9.683(8)	8.900(7)	5.228(4)	108.50(2)	427.26	A=193.6(2) B=146.0(2)	phenocryst in mare basalt 15476	Ohashi and Finger (1974b)
67.	clinohypersthene	P2 ₁ /c	9.691(3)	8.993(3)	5.231(2)	108.61(2)	432.0(2)	A=195.9 B=142.5	BI-9 of Virgo and Hafner (1969); metamorphosed iron formation, Quebec	Smyth (1974b)
68.	(Mn, Mg) clinopyroxene	P2 ₁ /c	9.719(2)	8.917(2)	5.248(1)	108.51(2)	431.29	—	synthetic	Ghose et al. (1975)
68b.	MnSiO ₃	P2 ₁ /c	9.864(2)	9.179(2)	5.298(1)	108.22	455.64	A=190.53 B=149.46	synthetic	Tokonami et al. (1979)
69.	protoenstatite Mg ₂ Si ₂ O ₆	P2 ₁ cn	9.304(4)	8.902(4)	5.351(3)	—	443.19	150.12	A.M.N.H. #3846; meteorite; Norton County, Kansas	Smyth (1971)
70.	(Mg, Li, Sc) protopyroxene	Pbcn	9.251(2)	8.773(2)	5.377(1)	—	436.39	167.32	synthetic	Smyth and Ito (1977)
71.	omphacite	P2/n	9.585(3)	8.776(3)	5.260(3)	106.85(3)	423.5(3)	169.45	eclogite; Iratsu mass; Bessi area, Japan	Matsumoto et al. (1975)
72.	titanian ferro-omphacite	P2/n	9.622(2)	8.826(2)	5.279(1)	106.92(2)	428.85	170.24	metamorphosed peralkaline rocks; Red Wine province, Central Labrador	Curtis et al. (1975)
73.	omphacite	P2	9.596(5)	8.771(4)	5.265(6)	106.93(7)	423.9(0.4)	A=165.0 C=165.0	#100-RGC-58 Tiburon Peninsula, California	Clark and Papike (1968)
74.	omphacite	P2	9.551(8)	8.751(5)	5.254(4)	106.87(8)	420.2(4)	A=170.3 C=169.1	Morgan (1967) #Ca-1059; Puerto Cabello, Venezuela	Clark et al. (1969)

^aCompositions are given only for end member pyroxenes.

^b03-03 angles greater than 180° indicate S-rotations.

^cRefinement is based on two-dimensional data.

Table A5. Symmetry information on pyroxene space groups

Space Group	Site	Point Symmetry	Multiplicity	Examples	Space Group	Site	Point Symmetry	Multiplicity	Examples
$\underline{C2/c}$	M1	2	4	Diopside, Augite, Jadeite	\underline{Pbca}	M1	1	8	Hypersthene, Orthoenstatite
	M2	2	4			M2	1	8	
	T	1	8			TA	1	8	
	01	1	8			TB	1	8	
	02	1	8			01A	1	8	
	03	1	8			01B	1	8	
$\underline{P2_1/c}$	M1	1	4	Pigeonite, Clinoenstatite		02A	1	8	
	M2	1	4			02B	1	8	
	TA	1	4			03A	1	8	
	TB	1	4			03B	1	8	
	01A	1	4		$\underline{P2/n}$	M1	2	2	Omphacite
	01B	1	4			M1(1)	2	2	
	02A	1	4			M2	2	2	
	02B	1	4			M2(1)	2	2	
	03A	1	4			T1	1	4	
	03B	1	4			T2	1	4	
\underline{Pbcn}	M1	2	4	Protoenstatite		01(1)	1	4	
	M2	2	4			01(2)	1	4	
	T	1	8			02(1)	1	4	
	01	1	8			02(2)	1	4	
	02	1	8		03(1)	1	4		
	03	1	8		03(2)	1	4		

Table A6. Pyroxene structures studied at high temperature

No.	Pyroxene	Space Group	Temperatures (°C) Studied at One Atmosphere Pressure	Mean Thermal Expansion Coefficient (°C ⁻¹ x 10 ⁻⁵) ^a								Reference
				α_a	α_{d100}	α_b	α_c	α_V	$\alpha_{\text{Mean T-O}}$	$\alpha_{\text{Mean M1-O}}$	$\alpha_{\text{Mean M2-O}}$	
2.	diopside ^b	$\underline{C2/c}$	24,400,700,850,1000	0.779 ^c	0.606	2.05	0.646	3.33	0.099	1.44	1.64	Cameron <i>et al.</i> (1973)
4.	hedenbergite	$\underline{C2/c}$	24,400,600,800,900,1000	0.724	0.483	1.76	0.597	2.98	0.026	1.05	1.61	Cameron <i>et al.</i> (1973)
6.	jadeite ^b	$\underline{C2/c}$	24,400,600,800	0.850	0.817	1.00	0.631	2.47	0.156	0.947	1.28	Cameron <i>et al.</i> (1973)
7.	ureyite ^b	$\underline{C2/c}$	24,400,600	0.585	0.691	0.946	0.390	2.04	0.529	0.633	1.26	Cameron <i>et al.</i> (1973)
8.	acmite ^b	$\underline{C2/c}$	24,400,600,800	0.727	0.804	1.20	0.450	2.47	0.182	0.781	1.28	Cameron <i>et al.</i> (1973)
11.	spodumene ^b	$\underline{C2/c}$	24,300,460,760	0.380	0.600	1.11	0.475	2.22	0.160	1.06	1.97	Cameron <i>et al.</i> (1973)
32.	orthoferrosilite	\underline{Pbca}	24,400,600,800,900,980	0.112	--	0.109	0.168	0.393	-0.350(TA)	1.59	4.59	Sueno <i>et al.</i> (1976)
44.	ferrohypersthene	\underline{Pbca}	20,175,280,500,700,850	0.135	--	0.145	0.154	0.438	-0.736(TB)	2.26	4.23	Smyth (1973)
									-0.285(TA)			
									-0.192(TB)			
61.	pigeonite	$\underline{P2_1/c}^d$	24,960	--	--	--	--	--	--	--	--	Brown <i>et al.</i> (1972)
67.	clinohypersthene	$\underline{P2_1/c}^e$	20,200,400,600,700	0.162	0.083	0.104	0.138	0.327	-0.212(TA)	1.476	4.70	Smyth (1974b)
									-2.88(TB)			

^a Mean thermal expansion coefficients are computed from the equation $\alpha_x = (1/X_{24})(X_T - X_{24})/(T - 24)$, where the slope of the regression equation is used for the term $(X_T - X_{24})/(T - 24)$.

^b Crystals used in this study were obtained from samples previously used by Prewitt and Burnham (1966; jadeite) and Clark *et al.* (1969; spodumene, acmite, diopside, and ureyite).

^c For 0.779, read 0.779 x 10⁻²°C⁻¹.

^d Transformed to $\underline{C2/c}$ above = 960°C.

^e Transformed to $\underline{C2/c}$ above = 725°C.

Table A7. Site occupancies of disordered silicate pyroxenes. Crystal data given in Table A4

No.	Pyroxene	Space Group	Site	Occupancy	Relevant Footnotes	Reference
19.	Augite	$C2/c$	M1 M2 T	0.715Mg + 0.182Al + 0.103Fe 0.616Ca + 0.187Mg + 0.107Fe + 0.090Na 0.91Si + 0.08Al + 0.01Ti	a	Clark <i>et al.</i> (1969)
20.	Augite	$C2/c$	M1 M2 T	0.68Mg + 0.11Al + 0.03Ti + 0.09Fe ²⁺ + 0.09Fe ³⁺ 0.74Ca + 0.06Na + 0.11Mg + 0.09Fe ²⁺ 0.865Si + 0.135Al	a,c,g	Takeda (1972b)
21.	Augite	$C2/c$	M1 M2 T	0.61Mg + 0.39Fe 0.83Ca + 0.13Fe + 0.04Mg 0.973Si + 0.027Al	a,c,g	Takeda <i>et al.</i> (1974)
22.	Augite	$C2/c$	M1 M2 T	0.63Mg + 0.37Fe 0.91Ca + 0.06Fe + 0.03Mg 0.963Si + 0.018Al + 0.003Ti + 0.016Fe	a,c,g	Takeda <i>et al.</i> (1974)
23.	Augite	$C2/c$	M1 M2 T	0.64Mg + 0.22Fe + 0.08Ti ⁴⁺ + 0.06Al 0.61Ca + 0.27Fe + 0.12Mg 0.893Si + 0.107Al	a,c	Takeda (1972a)
24.	Subcalcic diopside	$C2/c$	M1 M2 T	0.854Mg + 0.029Fe ²⁺ + 0.025Fe ³⁺ + 0.092Al 0.553Ca + 0.233Mg + 0.118Na + 0.096Fe ²⁺ 0.987Si + 0.013Al	a,c	McCallister <i>et al.</i> (1974)
24b.	Clinopyroxene	$C2/c$	M1 M2 T	0.634Mg + 0.172Al + 0.121Fe + 0.023Ti 0.634Ca + 0.201Mg + 0.093Na + 0.072Fe 0.911Si + 0.089Al	a,c	McCallister <i>et al.</i> (1976)
24c.	Clinopyroxene	$C2/c$	M1 M2 T	0.604Mg + 0.202Fe + 0.170Al + 0.024Ti 0.594Ca + 0.198Na + 0.136Fe + 0.072Mg 0.927Si + 0.073Al	a,c	McCallister <i>et al.</i> (1976)
25.	Fassaite (titanaugite)	$C2/c$	M1 M2 T	0.555Mg + 0.166Al + 0.155Fe ³⁺ + 0.063Ti ⁴⁺ + 0.061Fe ²⁺ 0.986Ca + 0.007Na + 0.007Mn 0.753Si + 0.247Al	a,m	Peacor (1967)
26.	Fassaite	$C2/c$	M1 M2 T	0.48Ti + 0.39Mg + 0.13Al 1.00Ca 0.645Si + 0.365Al	u	Dowty and Clark (1973)
27.	Fassaite	$C2/c$	M1 M2 T	0.568Mg + 0.210Fe + 0.161Al + 0.059Ti 0.968Ca + 0.020Fe + 0.010Mg 0.864Si + 0.136Al	a,c	Hazen and Finger (1977a)
28.	Ca tschermakite's pyroxene	$C2/c$	M1 M2 T	0.821Fe ³⁺ + 0.179Al 1.00Ca 1.00Si + 0.821Al + 0.179Fe ³⁺	a,h	Ghose <i>et al.</i> (1975)
29.	Omphacite	$C2/c$	M1 M2 T	0.543Mg + 0.240Al + 0.217Fe 0.590Ca + 0.320Na + 0.057Mg + 0.033Fe 0.998Si + 0.002Al	a,e	Clark <i>et al.</i> (1969)
33.	Bronzite	$Pbca$	M1 M2 TA TB	0.86Mg + 0.07Fe ³⁺ + 0.03Al + 0.03Fe ²⁺ + 0.01Ti 0.64Mg + 0.29Fe + 0.06Ca + 0.01Na 0.925Si + 0.075Al 0.925Si + 0.075Al	a,c,i	Takeda (1972b)
34.	Bronzite	$Pbca$	M1 M2 TA TB	0.91Mg + 0.07Fe + 0.02(Ti + Al + Cr + Mn) 0.50Fe + 0.44Mg + 0.06Ca 0.985Si + 0.015Al 0.985Si + 0.015Al	a,i	Takeda and Ridley (1972)
35.	Bronzite	$Pbca$	M1 M2 TA TB	0.89Mg + 0.064Fe + 0.05(Ti + Al + Cr + Mn) 0.52Mg + 0.39Fe + 0.09Ca 0.97Si + 0.03Al 0.97Si + 0.03Al	a,i	Takeda and Ridley (1972)
36.	Bronzite	$Pbca$	M1 M2 TA TB	0.967Mg + 0.033Fe ²⁺ 0.660Mg + 0.317Fe ²⁺ + 0.023Ca 0.987Si + 0.010Cr + 0.002Al + 0.001Ti 0.987Si + 0.010Cr + 0.002Al + 0.001Ti	a,c,i	Dodd <i>et al.</i> (1975)
37.	Bronzite	$Pbca$	M1 M2 TA TB	0.956Mg + 0.044Fe 0.511Mg + 0.435Fe + 0.054Ca 0.979Si + 0.021Al 0.979Si + 0.021Al	a,c,i	Miyamoto <i>et al.</i> (1975)
38.	Bronzite	$Pbca$	M1 M2 TA TB	0.871Mg + 0.129Fe 0.593Mg + 0.407Fe 0.973Si + 0.027Al 0.973Si + 0.027Al	a,d,i	Ghose and Wan (1973)
39.	Aluminous bronzite	$Pbca$	M1 M2 TA TB	0.764Mg + 0.200Al + 0.036Fe 0.631Mg + 0.359Fe + 0.010Ca 0.996Si + 0.004Ti 0.756Si + 0.240Al + 0.004Ti	a,e,j	Kosoi <i>et al.</i> (1974)

Table A7. (continued)

40.	Aluminous bronzite	<u>Pbca</u>	M1 M2 TA TB	0.700Mg + 0.210Al + 0.090Fe 0.685Mg + 0.305Fe + 0.010Ca 0.996Si + 0.004Ti 0.756Si + 0.240Al + 0.004Ti	a,e,j	Kosoi <u>et al.</u> (1974)
41.	Hypersthene	<u>Pbca</u>	M1 M2 TA TB	0.85Mg + 0.15Fe ²⁺ 0.90Fe ²⁺ + 0.10Mg 0.97Si + 0.03Al 0.97Si + 0.03Al	a,d,i	Ghose (1965)
42.	Hypersthene	<u>Pbca</u>	M1 M2 TA TB	0.931Mg + 0.069Fe 0.811Fe + 0.159Mg + 0.030Ca 0.971Si + 0.028Al + 0.001Ti 0.971Si + 0.028Al + 0.001Ti	a,e,i	Kosoi <u>et al.</u> (1974)
43.	Hypersthene	<u>Pbca</u>	M1 M2 TA TB	0.810Mg + 0.190Fe ²⁺ 0.396Mg + 0.604Fe ²⁺ 1.00Si 1.00Si	a,h	Ghose <u>et al.</u> (1975)
44.	Ferrohypersthene	<u>Pbca</u>	M1 M2 TA TB	0.574Mg + 0.425Fe 0.906Fe + 0.062Mg + 0.032Ca 0.999Si + 0.001Al 0.999Si + 0.001Al	a,i	Smyth (1973)
45.	Aluminous hypersthene	<u>Pbca</u>	M1 M2 TA TB	0.88Mg + 0.10Al + 0.02Fe ²⁺ 0.58Mg + 0.25Fe ²⁺ + 0.13Al + 0.04Fe ³⁺ 1.00Si 0.87Si + 0.13Al	k,j,r,s	Brovkin <u>et al.</u> (1975)
46.	Eulite	<u>Pbca</u>	M1 M2 TA TB	0.75Fe ²⁺ + 0.25Mg 0.96Fe ²⁺ + 0.04Ca 0.992Si + 0.008Al 0.992Si + 0.008Al	a,d,f,i	Burnham <u>et al.</u> (1971)
47.	(Mg, Co) orthopyroxene	<u>Pbca</u>	M1 M2 TA TB	0.871Mg + 0.129Co 0.681Mg + 0.319Co 1.00Si 1.00Si	b,h	Hawthorne and Ito (1978)
48.	(Mg, Mn) orthopyroxene	<u>Pbca</u>	M1 M2 TA TB	0.977Mg + 0.023Mn 0.873Mg + 0.127Mn 1.00Si 1.00Si	b,h	Hawthorne and Ito (1978)
49.	(Mg, Mn, Co) orthopyroxene	<u>Pbca</u>	M1 M2 TA TB	0.904Mg + 0.065Co ²⁺ + 0.031Mn ²⁺ 0.658Mg + 0.198Co ²⁺ + 0.144Mn ²⁺ 1.00Si 1.00Si	b,h,k	Hawthorne and Ito (1977)
50.	(Zn, Mg) orthopyroxene	<u>Pbca</u>	M1 M2 TA TB	0.64Mg + 0.36Zn 0.64Zn + 0.36Mg 1.00Si 1.00Si	v,h	Morimoto <u>et al.</u> (1975)
51.	(Zn, Mg) orthopyroxene	<u>Pbca</u>	M1 M2 TA TB	0.933Mg + 0.067Zn 0.617Mg + 0.383Zn 1.00Si 1.00Si	b,h	Ghose <u>et al.</u> (1975)
52.	(Ni, Mg) orthopyroxene	<u>Pbca</u>	M1 M2 TA TB	0.789Mg + 0.211Ni 0.831Mg + 0.169Ni 1.00Si 1.00Si	b,h	Ghose <u>et al.</u> (1975)
53.	(Co, Mg) orthopyroxene	<u>Pbca</u>	M1 M2 TA TB	0.735Mg + 0.265Co 0.525Mg + 0.475Co 1.00Si 1.00Si	b,h	Ghose <u>et al.</u> (1975)
60.	Pigeonite	<u>P2₁/c</u>	M1 M2 TA TB	0.720Mg + 0.280Fe 0.760Fe + 0.18Ca + 0.060Mg 1.00Si 1.00Si	a,h	Morimoto and Güven (1970)
61.	Pigeonite	<u>P2₁/c</u>	M1 M2 TA TB	0.702Mg + 0.298Fe 0.742Fe + 0.180Ca + 0.078Mg 1.00Si 1.00Si	a,h	Brown <u>et al.</u> (1972)
62.	Pigeonite	<u>P2₁/c</u>	M1 M2 TA TB	0.78Mg + 0.15Fe ²⁺ + 0.03Ti + 0.04Al 0.57Fe ²⁺ + 0.27Mg + 0.16Ca 0.991Si + 0.009Al 0.991Si + 0.009Al	a,i	Clark <u>et al.</u> (1971)
63.	Pigeonite	<u>P2₁/c</u>	M1 M2 TA TB	0.86Mg + 0.12Fe + 0.01Al + 0.02Ti ⁴⁺ 0.46Fe + 0.35Mg + 0.18Ca 0.955Si + 0.045Al 0.955Si + 0.045Al	a,c,i	Takeda (1972a)
64.	Pigeonite	<u>P2₁/c</u>	M1 M2 TA TB	0.62Mg + 0.38Fe 0.69Fe + 0.20Mg + 0.106Ca 0.997Si + 0.003Al 0.997Si + 0.003Al	a,i	Takeda <u>et al.</u> (1974)

Table A7. (continued)

65.	Pigeonite	$P2_1/c$	M1 M2 TA TB	0.66Mg + 0.34Fe 0.90Fe + 0.06Mg + 0.04Ca 0.996Si + 0.003Al + 0.001Ti 0.996Si + 0.003Al + 0.001Ti	a,c,i	Takeda <i>et al.</i> (1974)
66.	Pigeonite	$P2_1/c$	M1 M2 TA TB	0.930Mg + 0.070Fe 0.450Fe + 0.430Mg + 0.120Ca 1.00Si 1.00Si	a,h	Ohashi and Finger (1974b)
67.	Clinohypersthene	$P2_1/c$	M1 M2 TA TB	0.503Fe + 0.497Mg 0.834Fe + 0.134Mg + 0.032Ca 0.999Si + 0.001Al 0.999Si + 0.001Al	a,i	Smyth (1974b)
68.	(Mn, Mg) clinopyroxene	$P2_1/c$	M1 M2 TA TB	0.882Mg + 0.118Mn 0.218Mg + 0.782Mn 1.00Si 1.00Si	b,h	Chose <i>et al.</i> (1975)
70.	(Mg,Li,Sc) protopyroxene	$Pbcn$	M1 M2 T	0.70 Mg + 0.30Sc 0.70 Mg + 0.30Li 1.00Si	b	Smyth and Ito (1977)
71.	Omphacite	$P2/n$	M1 M1(1) M2 M2(1) T1 T2	0.815Mg + 0.185Fe 0.868Al + 0.132Fe 0.686Na + 0.314Ca 0.716Ca + 0.284Na 0.959Si + 0.041Al 0.959Si + 0.041Al	a,i	Matsumoto <i>et al.</i> (1975)
72.	Titanian ferro-omphacite	$P2/n$	M1 M1(1) M2 M2(1) T1 T2	0.786Fe + 0.214Al 0.749Al + 0.251Fe 0.740Na + 0.260Ca 0.672Ca + 0.328Na 0.976Si + 0.024Al 0.976Si + 0.024Al	a,i	Curtis <i>et al.</i> (1975)
73.	Omphacite	$P2$	M1 M1(1) M1H M1(1)H M2 M2(1) M2H M2(1)H T1A T2A T1C T2C	0.81Mg + 0.19Fe ²⁺ 0.95Al + 0.05Fe ³⁺ 0.82Al + 0.18Fe ³⁺ 0.80Mg + 0.20Fe ²⁺ 0.64Na + 0.36Ca 0.64Ca + 0.36Na 0.97Ca + 0.03Na 0.64Na + 0.36Ca 0.98Si + 0.02Al 0.98Si + 0.02Al 0.98Si + 0.02Al 0.98Si + 0.02Al	a,i,t	Clark and Papike (1968)
74.	Omphacite	$P2$	M1 M1(1) M1H M1(1)H M2 M2(1) M2H M2(1)H T1A T2A T1C T2C	0.82Mg + 0.10Fe + 0.08Al 1.00Al 0.92Al + 0.08Fe 0.90Mg + 0.10Fe 0.76Na + 0.24Ca 0.75Ca + 0.25Na 0.69Ca + 0.31Na 0.68Na + 0.32Ca 0.99Si + 0.01Al 0.99Si + 0.01Al 0.99Si + 0.01Al 0.99Si + 0.01Al	a,i,t	Clark <i>et al.</i> (1969)

- a Assignment of Fe vs Mg in M sites based on site occupancy refinement and/or adjustment of temperature factors, form factors, etc. Remainder of cations assigned to M1 and M2 using crystal chemical principles.
- b Assignment of cations to M sites based on site occupancy refinement.
- c Minor Ti and/or Cr and/or Mn included with Fe in site occupancy refinement.
- d Minor Al and/or Cr and/or Ti and/or Mn ignored in site occupancy refinement.
- e Assignment of minor Mn and/or Cr and/or Na and/or Ti not reported.
- f Minor VIAl included with Mg.
- g Assignment of cations to T sites done by present authors using crystal chemical principles.
- h Tetrahedral site occupancy fixed at 1.0 Si based on general formula in the reference cited.
- i No site refinement of Al and Si in T sites attempted and identical site occupancies were assigned by present authors. See original papers for details because bond distances in some crystals indicate a concentration of Al in TB.
- j Assignment of Si vs Al in T sites based on site occupancy refinement and/or adjustment of temperature factors, etc.
- k T site occupancies adjusted on basis of interatomic distances.
- m Cation fractions normalized by present authors so that total occupancy of each site equals 1.0.
- n Equal amounts of Ti assigned to TA and TB.
- r Al in M1 and M2 not constrained by known composition of sample.
- s Authors stated that most of Al occupies the TB position, but in another sentence they state that 13 per cent of the Al atoms are in this position. The discrepancy may have arisen during the translation from Russian and the 13 per cent may indicate 0.13 Al atoms of the 0.17 Al atoms occupy TB.
- t Site labels are from cited reference.
- u Cations assigned to M and T sites using crystal chemical principles and interatomic distances.
- v Assignment of cations to M sites using Fourier syntheses.

Table A8. Pyroxene Other-Other cation correlations^a

Group	VI _{Al} -IV _{Al}	VI _{Fe3+} -IV _{Al}	VI _{Cr3+} -IV _{Al}	VI _{Ti4+} -IV _{Al}	Na-VI _{Al}	Na-VI _{Fe3+}	Na-VI _{Cr3+}	Na-VI _{Ti4+}
Archean	0.527	0.203	0.360	0.527	0.427	-0.319	-0.353	-0.282
Columbia Plateau	-0.436	0.568	0.072	0.566	-0.027	0.202	-0.121	0.395
Deep Sea	0.232	0.584	0.068	0.590	-0.051	0.453	-0.137	0.349
Equilibrated Euclrites	0.270	-	0.342	0.328	0.021	-	-0.032	-0.078
Pasamonte	0.033	-	0.234	0.488	-0.059	-	-0.054	0.088
Shergotty	-0.100	-	0.129	0.260	0.234	-	0.173	0.160
Hawaiian	0.495	0.436	0.375	0.932	0.178	0.608	0.069	0.537
Island Arc	0.588	0.486	0.213	0.355	0.378	-0.223	-0.156	0.382
Keweenawan	0.091	0.794	0.360	0.635	-0.042	0.562	0.159	0.568
Lunar Highlands	0.285	-	0.562	0.642	-0.136	-	0.050	0.611
Lunar Mare	0.675	-	0.300	0.833	0.158	-	0.068	0.598
Rio Grande	0.304	0.818	0.207	0.642	0.571	0.463	-0.210	0.001

^a Correlation coefficients > 0.6 are underlined.

Table A9. Pyroxene Other-Quad cation correlations

Group	Ti-Ca	Ti-Mg	Ti-Fe ²⁺	VI _{Al} -Ca	VI _{Al} -Mg	VI _{Al} -Fe ²⁺	Fe ³⁺ -Ca	Fe ³⁺ -Mg	Fe ³⁺ -Fe ²⁺	Cr-Ca	Cr-Mg	Cr-Fe ²⁺
Archean	0.519	-0.785	0.645	-0.180	-0.020	-0.198	0.266	-0.086	-0.106	0.035	0.150	-0.363
Columbia Plateau	0.405	-0.541	0.357	-0.441	0.146	0.008	0.468	0.234	-0.546	-0.269	0.210	-0.116
Deep Sea	-0.014	-0.486	0.405	0.152	0.142	-0.306	0.342	-0.166	-0.196	0.284	0.382	-0.586
Equilibrated Euclrites	0.159	-0.110	-0.147	0.083	-0.136	-0.107	-	-	-	0.043	-0.086	-0.009
Pasamonte	0.783	-0.841	0.808	-0.234	0.288	-0.370	-	-	-	-0.224	0.218	-0.225
Shergotty	0.323	-0.768	0.372	0.351	0.064	0.301	-	-	-	0.639	0.292	-0.792
Hawaiian	0.737	-0.783	-0.550	0.494	-0.533	-0.290	0.278	-0.249	-0.522	0.194	-0.184	-0.358
Island Arc	0.101	-0.505	0.243	0.322	-0.687	0.008	0.009	0.064	-0.233	0.469	-0.153	-0.508
Keweenawan	0.450	-0.529	-0.177	0.132	0.198	0.378	0.558	-0.382	-0.451	0.374	0.133	-0.621
Lunar Highlands	0.760	-0.493	-0.090	-0.357	0.392	-0.285	-	-	-	0.201	0.233	-0.603
Lunar Mare	0.713	-0.213	-0.273	0.135	-0.187	-0.025	-	-	-	-0.033	0.645	-0.680
Rio Grande	0.372	-0.522	-0.105	0.123	-0.013	-0.411	0.637	-0.574	-0.669	0.167	-0.052	-0.225

Table A9. (continued)

Group	Na-Ca	Na-Mg	Na-Fe ²⁺	IV _{Al} -Ca	IV _{Al} -Mg	IV _{Al} -Fe ²⁺	Mn-Ca	Mn-Mg	Mn-Fe ²⁺	IV _{Al} -XFe	Cr-XFe	Mn-XFe	Na-XFe	Ti-XFe
Archean	-0.409	0.258	0.208	0.346	-0.498	0.131	0.272	-0.373	0.431	0.304	-0.316	0.434	-0.249	0.773
Columbia Plateau	0.534	-0.555	0.225	0.726	-0.092	-0.331	0.041	-0.509	0.524	-0.209	-0.137	0.514	0.342	0.438
Deep Sea	0.335	-0.469	0.114	0.359	-0.227	-0.203	-0.345	-0.675	0.938	-0.101	-0.572	0.919	0.256	0.446
Equilibrated Euclrites	0.000	-0.015	0.009	0.458	-0.154	-0.501	-0.664	0.175	0.729	-0.447	0.052	0.646	0.013	-0.099
Pasamonte	0.091	-0.135	0.163	0.445	-0.391	0.287	0.521	-0.646	0.699	0.372	-0.239	0.660	0.136	0.844
Shergotty	0.461	-0.149	-0.252	0.148	-0.044	-0.066	0.020	-0.055	0.823	-0.019	-0.721	0.736	-0.145	0.557
Hawaiian	0.720	-0.722	-0.682	0.733	-0.758	-0.691	-0.152	0.098	0.382	0.108	-0.221	0.422	0.013	0.355
Island Arc	-0.231	-0.374	0.483	0.388	-0.611	-0.237	-0.852	0.474	0.726	-0.016	-0.429	0.509	0.612	0.465
Keweenawan	0.722	-0.613	-0.452	0.782	-0.493	-0.663	-0.403	-0.176	0.681	-0.432	-0.686	0.657	-0.178	0.076
Lunar Highlands	0.542	-0.327	-0.098	0.383	0.034	-0.526	0.294	-0.656	0.698	-0.367	-0.506	0.711	0.056	0.132
Lunar Mare	0.434	-0.169	-0.124	0.513	-0.063	-0.357	-0.231	-0.637	0.817	-0.178	-0.707	0.757	0.011	-0.090
Rio Grande	0.618	-0.599	-0.584	0.538	-0.507	-0.593	-0.569	0.337	0.709	-0.444	-0.193	0.542	-0.391	0.177